Meridional Exchanges and Mixing at the Iceland-Faroe Ridge

Nicholas L. Beaird

A dissertation
submitted in partial fulfillment of the
requirements for the degree of

Doctor of Philosophy

University of Washington

2013

Reading Committee:

Peter Rhines, Chair

Charles Eriksen, Chair

LuAnne Thompson

Program Authorized to Offer Degree:
School of Oceanography

University of Washington

Abstract

Meridional Exchanges and Mixing at the Iceland-Faroe Ridge

Nicholas L. Beaird

Co-Chairs of the Supervisory Committee:
Professor Peter Rhines

Professor Charles Eriksen
School of Oceanography

The Greenland-Scotland Ridge influences the exchange of warm and cold water masses between the North Atlantic and the Nordic Sea, a circulation with significant impact on global ocean circulation and climate. This study examines aspects of the exchange east of Iceland. Data from three years of intense Seaglider hydrographic surveys of the region are used.

The dense overflows across the Iceland-Faroe Ridge (IFR) and Faroe Bank Channel (FBC) are investigated in Chapter 2. The flow of dense overflow on the Atlantic side of the IFR is found to be directed along-slope with speeds averaging 21.5 cm s^{-1}. The overflow/ambient interface lays parallel to the IFR topography. Mesoscale eddy deformation of the interface is generally small compared with the topographically induced slope. The mean FBC overflow transport is estimated at 1.8±0.2 Sv, and an indirect calculation produces a lower bound estimate of IFR overflow of 0.8 Sv. The dominant IFR overflow branch (mean 0.48 Sv) is at the northwestern end of the ridge, where a highly variable narrow jet along the Iceland shelf break transports dense water to the southwest.

Chapter 3 outlines a method to infer dissipation of turbulent kinetic energy using Seaglider observations of finescale vertical velocity and density. The resulting

Seaglider-inferred dissipation estimates compare well with observations made by a standard microstructure shear probe. Application of the method to the full set of Seaglider dives from the field campaign reveals regions of elevated dissipation and mixing which are crucial to the development of North Atlantic Deep Water (NADW) and the lower branch of the Atlantic Meridional Overturning Circulation (AMOC).

A seasonal flux of fresh water across the IFR is explored in Chapter 4. Low salinity thermohaline intrusions are subducted in winter time at the Iceland Faroe Front, injecting cold, fresh water into the large volume of Atlantic Subpolar Mode Water south of the ridge. The associated heat and salt flux are comparable to previous estimates of eddy induced and intrusion driven fluxes at the front. The heat and salt flux is inconsequential relative to the total heat and salt budgets of the Nordic Seas, but is important locally.

TABLE OF CONTENTS

Page

List of Figures ii

Chapter 1: **Introduction** 1
- 1.1 Flow of Atlantic Waters to the Ridge 3
- 1.2 The Iceland-Faroe Ridge and Front 4
- 1.3 Circulation and Modification in the Nordic Seas 7
- 1.4 Overflows at the GSR 8
  - 1.4.1 Denmark Strait overflow 9
  - 1.4.2 IFR overflow 9
  - 1.4.3 FBC overflow 10
- 1.5 Circulation of the overflow waters in the North Atlantic 11
- 1.6 Climate Impacts of Cross Iceland-Scotland Ridge exchanges 12
- 1.7 Overview of Chapters 12

Chapter 2: **Overflow Waters at the Iceland-Faroe Ridge Observed in Multi-Year Seaglider Surveys** . . . 18
- 2.1 Introduction 18
- 2.2 Data 21
- 2.3 Methods 23
- 2.4 Faroe Bank Channel 25
  - 2.4.1 FBC Composite Section 26
  - 2.4.2 FBC Exit 28
- 2.5 Iceland-Faroe Ridge 29
  - 2.5.1 IFR Composite Sections 30
  - 2.5.2 Distribution of Overflow on the IFR 33
  - 2.5.3 Near-Bottom Velocities 35
- 2.6 Western Valley 39

2.7 Conclusions 41
2.8 Figures 43

Chapter 3: **Dissipation of Turbulent Kinetic Energy Inferred from Seagliders: An Application to the Eastern Nordic Seas Overflows** 59
3.1 Introduction 59
3.2 Measurements 61
3.3 Methods 64
3.3.1 Vertical Velocities from Seaglider 64
3.3.2 Large-Eddy method 66
3.3.3 Choosing the Scales 68
3.4 Method Validation 70
3.4.1 VMP & Seaglider comparison survey 70
3.5 Results & Discussion 75
3.5.1 Seaglider-inferred dissipation section 75
3.5.2 Mixing 'Hot Spots' 76
3.6 Summary 80
3.7 Figures 82

Chapter 4: **Evidence of Direct Exchange of Low Salinity Intermediate Waters Across the Iceland-Faroe Ridge in Winter** 95
4.1 Introduction 95
4.2 Measurements 98
4.3 Results 98
4.3.1 Water mass structure south of the front 98
4.3.2 Fresh Thermohaline Intrusions 100
4.3.3 Seasonality and Geographic distribution of intrusions 105
4.4 Discussion 107
4.4.1 Possible mechanisms of subduction 108
4.4.2 Basic heat and salt flux estimates 110
4.5 Conclusions 113

Chapter 5: **Conclusions** 130

Bibliography 133

LIST OF FIGURES

Figure Number		Page
1.1	Regional reference map	15
1.2	Hansen & Østerhus 2000 surface circulation	16
1.3	Hansen & Østerhus 2000 deep circulation	17
2.1	IFR bathymetry and section locations	44
2.2	Cross-IFR salinity and velocity section	45
2.3	Regional water mass temperature-salinity diagram	46
2.4	Bottom temperature from each Seaglider dive	47
2.5	Section I properties	47
2.6	FBC outflow thickness and bottom temperature	48
2.7	Mean overflow density at all composite sections	49
2.8	Overflow transport across composite sections	50
2.9	Mean and minimum bottom temperature	51
2.10	Example temperature and salinity profiles	52
2.11	Plume properties downstream of the sill	53
2.12	Overflow velocities on the IFR	54
2.13	Distribution of interface slopes	55
2.14	Bottom temperatures in the Western Valley	56
2.15	Particle trajectories to the Western Valley	57
2.16	Density sections in the Western Valley	58
3.1	Seaglider dive locations	83
3.2	VMP survey and Seaglider dives in the FBC	84
3.3	Example Seaglider vertical velocity profiles	84
3.4	Distribution of Seaglider and moored ADCP vertical velocity	85
3.5	Time series of FBC interface height	86
3.6	Survey averaged FBC property profiles	87
3.7	Ratio of inferred and measured dissipation	88

3.8 Distribution of dissipation in FBC layers 89
3.9 Seaglider section of temperature and dissipation 90
3.10 Vertically integrated dissipation rates over the plume thickness 91
3.11 Integrated dissipation in the FBC 92
3.12 Section of dissipation and temperature in the Western Valley 93
3.13 Integrated dissipation in the Western Valley 94

4.1 Sea surface temperature and bathymetry of the IFR 114
4.2 Regional water mass temperature and salinity relationships 115
4.3 Seaglider tracks for three example sections 116
4.4 Section across the IFR 117
4.5 Schematic section of regional water masses 118
4.6 Example section of fresh intrusions in 2007 119
4.7 Example section of fresh intrusions in 2008 120
4.8 Temperature-Salinity kernel density estimates in intrusive/nonintrusive groups 121
4.9 Geographic and temporal distribution of fresh intrusions 122
4.10 Time series of intrusion frequency 122
4.11 Seasonal histogram of temperature-salinity relations on the IFR . . . 123
4.12 Seasonal histogram of temperature-salinity relations in the FBC . . . 124
4.13 Seasonal upper water column properties on the IFR 125
4.14 Cross IFR salinity and potential vorticity sections 126
4.15 Seaglider section at the IFF 127
4.16 Sea surface temperature at the IFF 128

ACKNOWLEDGMENTS

I am endlessly grateful to my advisors Peter Rhines and Charlie Eriksen for their guidance and support which allowed me to succeed in graduate school. I learned a tremendous amount during my time at the University of Washington and owe much of the credit to them.

I also worked closely with Ilker Fer in writing the third chapter of this thesis. I had a wonderful experience with Ilker in Norway and did what became some of my favorite work there. I would like to acknowledge Ilker's significant impact on my graduate studies.

I would like to thank my committee for their significant help as well: LuAnne Thompson, Eric D'Asaro, Paul Quay and Chris Bretherton.

Our lab group made all the data collection and much of the science interpretation possible, and for this I owe thanks to Kirk O'Donnell, Jim Bennett, and Bill Ferdericks.

I have learned a huge amount from the students (and former students) in the UW School of Oceanography, particularly Noel Pelland, Eleanor Frajka-Williams, Alison Gray, Sally Warner, Tom Connolly, and Sara Bender.

The collection of data used in the thesis was made possible by the significant help of Bogi Hansen, and Hjálmar Hátún and the crew of the *R.V. Magnus Heinason* in the Faroe Islands and the R/V *Håkon Mosby* of Norway. Support for the data collection and analysis came from the National Science Foundation, OCE Division, through grants OCE-1029344 and OCE-0550584. Additional observations were made under Project 204867 funded by the Research Council of Norway.

Chapter 1

INTRODUCTION

The shallow topography which connects Greenland to Scotland via Iceland and the Faroe Plateau is a dynamic impediment to meridional ocean circulation with significant influence on global ocean circulation and climate. On one side of the ridge are the Nordic and Arctic Seas, on the other the North Atlantic (Fig. 1.1). In the upper ocean, water masses of tropical origin flow north across the ridge into the polar marginal seas where they undergo water mass transformation and form the precursors of North Atlantic Deep water (NADW). The ridge imposes constraints on the return of the recently formed dense water, forcing it through several deep gaps in the ridge crest. The dense water subsequently forms highly turbulent gravity currents, or 'overflows'. Entrainment of ambient water into the overflows results in substantial additional water mass modification, setting the properties of NADW. The combined meridional circulation comprises the northern end (downwelling branch) of the Atlantic Meridional Overturning Circulation (AMOC). The AMOC drives much of the circulation in the deep North Atlantic ocean below the wind driven gyres. The ridge is unique in that it forces the upper and lower branches of the AMOC into close vertical proximity. In general the region is one of complex three dimensional circulation, strongly influenced by turbulent mixing, topographic interactions, frontal ageostrophic circulation, and buoyancy forced flows. The important dynamical scales are small owing to shallow topography and strong rotation. This complex and influential region provides significant challenges to observational oceanography. The investigations contained in this thesis pertain to the mean circulation of the dense overflows on the Iceland-Faroe Ridge (Chapter 2), the turbulent mixing and entrain-

ment of Atlantic waters into those overflows (Chapter 3), and the seasonal flux of low salinity intermediate water across the Iceland Faroe Front by mesoscale and submesoscale features (Chapter 4).

The topographic barrier between the North Atlantic and the Nordic Seas is called the Greenland-Scotland Ridge (GSR) and is broken into three main gaps: the Denmark Strait between Greenland and Iceland; the Iceland-Faroe Ridge (IFR) between Iceland and the Faroe Plateau; and the Faroe Shetland and Faroe Bank Channels (FSC, FBC) between the Faroe Plateau and the Shetland Islands. Meridional exchange occurs in each gap, and will be quickly reviewed here. The Denmark Strait contains two branches of equatorward flow of Arctic water: one in the surface East Greenland Current; and another at depth in the Denmark Strait overflow (3 Sv) (Girton and Sanford, 2003). A small amount of northward flow of Atlantic water occurs in the Denmark Strait in the North Icelandic Irminger Current ($\sim$1) Sv (Hansen and Østerhus, 2000). The IFR is the shallowest and widest gap in the GSR and hosts a irregular overflow of about 1 Sv (Hermann, 1967; Beaird et al., 2013) and a northward flow of warm water (4 Sv) which represents approximately half of the Atlantic inflow to the Nordic Seas (Hansen et al., 2003; Rossby and Flagg, 2012). The other half (4 Sv) of the inflow occurs in the final gap, the FSC (Hansen and Østerhus, 2000). The FSC and its extension the FBC also contain about 2 Sv of equatorward dense overflow (Hansen and Østerhus, 2007). Throughout the following discussion of exchanges between the North Atlantic and the Nordic Seas, the poleward flow towards the Nordic Seas will be termed 'inflow' and the equatorward flow of dense Nordic/Arctic waters to the North Atlantic will be 'outflow' or 'overflow'. Schematic representations of the major surface and deep circulations are reproduced in Figures 1.2 and 1.2 from the exhaustive review of North Atlantic-Nordic Seas exchanges by Hansen and Østerhus (2000). These current diagrams should prove useful as references for the discussions of the somewhat Byzantine circulation of water masses in the GSR region. In particular, the discussion of water masses in Chapter 4 should be aided by these introductory

figures.

The focus of this thesis is the mixing and circulation of waters in the FBC and on the IFR. In this introduction background material will be presented by following the AMOC, starting with the transport of warm waters north to the GSR, their modification in the Nordic Seas, and overflow back across the GSR as dense water. Some global circulation and climate impacts will be presented.

1.1 Flow of Atlantic Waters to the Ridge

The inflow of Atlantic water to the Nordic Seas is important on both regional and global scales. The heat lost from the warm Atlantic waters to the atmosphere keeps Scandinavia more mild than it would otherwise be Hansen and Østerhus (2000). The salt transported by the inflow is integral to the subsequent production of dense water by convective cooling. The salt adds the necessary density to allow the surface waters to cool and sink to great depth, completing the downwelling loop of the AMOC. The pathways which the warm salty waters follow, and the modification along the way, are of great importance to our understanding of ocean circulation. The main branches of inflow to the Nordic Seas are through the FSC (FSC branch), across the IFR (IFR branch), and clockwise around Iceland (the North Icelandic Irminger Current).

Hansen and Østerhus (2000) define two source regions (oceanic and continental) for the flow of Atlantic waters to the GSR, both of which are fairly similar in properties. The continental source flows along the European continental shelf and feeds the flow in the FSC (Fig. 1.2). It contains more Mediterranean Water influence, and is therefore saltier than the oceanic source. The FSC inflow branch is not the focus of this thesis, therefore attention will be focused on the oceanic source. It should be noted, however, that about half of the total inflow of Atlantic water to the Nordic Seas occurs in the FSC (Hansen and Østerhus, 2000; Rossby and Flagg, 2012). Brambilla and Talley (2008) suggest that the open ocean source provides much of the Atlantic water which flows through the FSC, citing observational evidence which calls into question the

scheme proposed by Hansen and Østerhus (2000).

The subtropical Atlantic waters being carried towards the ridge in the North Atlantic Current are considered the oceanic source. This water is modified along its path by mixing with subpolar waters and by air-sea interaction. Hansen and Østerhus (2000) call this water Modified North Atlantic Water (MNAW) and suggest that it is the main source of Atlantic water to the IFR inflow branch. They note that MNAW is a type of Sub Polar Mode Water (SPMW), a thick low stratification water mass with weak vertical gradients of temperature and salinity formed in winter by air-sea interaction (McCartney and Talley, 1982). SPMWs carry heat and salt into dense water formation regions in the Nordic and Labrador Seas. Brambilla and Talley (2008) use hydrographic and Lagrangian drifter data to define the circulation of SPMW in the northeast Atlantic. They find a complicated multi-branched circulation carrying SPMW to the IFR, FSC and Iminger and Labrador Seas to the west. The scheme revises the older view of a smooth cyclonic gyre circulation found in McCartney and Talley (1982). Brambilla and Talley (2008) identify three branches of the North Atlantic Current carrying SPMW to the GSR: the Rockall Trough Branch feeds the Faroe-Shetland Channel, and the Subarctic Front and Central Iceland Basin branches feed the Iceland Faroe Ridge region. The branched structure of the northward flow is also seen in the studies of Sarafanov et al. (2012) and Chafik et al. (subm.).

1.2 The Iceland-Faroe Ridge and Front

The Iceland Faroe Ridge is the widest gap in the GSR, and includes the largest frontal area between North Atlantic and Nordic/Arctic waters. The gap between Iceland and the Faroes is approximately 300 km wide and 450 m deep. The ridge is aligned northwest to southeast. Throughout this thesis the cross-ridge direction towards the Nordic Seas will be referred to as 'poleward', and the cross-ridge direction towards the Iceland Basin is termed 'equatorward'. This description derives from the ultimate fate of watermasses moving in those directions. The vertical water mass structure

above the Atlantic flank of the IFR (AIFR) can be roughly described as Atlantic waters sitting above a thin layer of dense overflow whose isopycnals lay parallel to the ridge topography. A decade of repeat hydrographic surveys by Meincke (1972) show that MNAW is ubiquitous in the upper layers above the AIFR. The overflow layer will be discussed in a later section, this section will focus on the upper Atlantic layer feeding the inflow to the Nordic Seas. The Atlantic waters above the IFR are predominantly MNAW, with an intermittent layer of Intermediate Water (IW) between the MNAW and the overflow. IW is a 'biogeochemically defined' water mass from the permanent pycnocline of the Iceland Basin, visible as an oxygen minimum in the density range $\sigma_\theta = 27.55 - 27.65$kg m^{-3} (van Aken and de Boer, 1995; Sarafanov et al., 2008). Ullgren et al. (in press) show that the distribution of IW on the IFR and in the FBC is patchy, and that it may be entrained into the overflow when present.

The interface between Atlantic waters and the overflow layer rises from the IFR crest and slopes up to the north, forming the Iceland Faroe Front (IFF). The IFF marks the boundary between the North Atlantic and Nordic/Arctic waters at depths shallower than the IFR crest. Hansen and Østerhus (2000) point out that the frontal system is more complicated than that simple description; a second front, the Jan Mayen, follows the IFF in the west and breaks off to head north. The Jan Mayen Front separates the East Icelandic Current from Nordic and recirculated Atlantic waters. The density contrast across the IFF is ~ 0.5 kg m^{-3} and the dynamic height (relative to the ridge crest depth) change is approximately 25 dynamic cm (0.25 J kg^{-1}). Numerous water masses converge at the Iceland Faroe Front. The Atlantic waters, MNAW and IW, have been mentioned above. Read and Pollard (1992) provide the most comprehensive list of Nordic and Arctic water masses at the front. These include Arctic Intermediate Water (AIW), Norwegian Sea Deep Water (NSDW), East Icelandic Current Water (EIC), and East Icelandic Water (EIW). Read and Pollard (1992) define Modified East Icelandic Water (MEIW) at the IFF as a mixture of the cold fresh waters originating near Iceland. MEIW is the primary low salinity water

mass found at the IFF (Meincke, 1978).

The IFF is topographically locked, meaning its average position is approximately aligned with the IFR crest and the isobaths north of the Faroe Islands (Hansen and Meincke, 1979; Smart, 1984). The position can vary by hundreds of km on the order of weeks or months, but appears to be seasonally invariant (Smart, 1984). Summer time heating can obscure the surface expression of the front, but the subsurface position does not appear to have seasonal dependance.

The front is more steeply sloped near its start at the Iceland shelf (0.015) and flattens by fivefold by the Faroe Plateau (Read and Pollard, 1992). The downstream diffusion of the front is due to mixing generated by vigorous eddying and meandering (Hansen and Meincke, 1979; Allen et al., 1994), and the associated conversion of potential to kinetic energy induced by baroclinic instability (Willebrand and Meincke, 1980). Mesoscale eddies in the size range 15-50 km are ubiquitous in the IFR region (Hansen and Meincke, 1979; Niiler, 1992; Pistek and Johnson, 1992; Allen et al., 1994). The front appears to be baroclinicly unstable (Willebrand and Meincke, 1980; Allen et al., 1994), with breaking meanders shedding the observed eddies. Allen et al. (1994) estimate the fastest growing unstable wavelength to be 47 km with a period of 4.3 days. They suggest most (85-99%) of the energy of perturbations comes from vertical rather than horizontal shear (baroclinic rather than barotropic instability).

The layer of Atlantic water is squeezed vertically as it flows onto the IFR. To conserve Potential Vorticity (PV) this vortex squashing should be accompanied by the development of anticyclonic relative vorticity. Indeed anticyclonic shear does develop as the Faroe Current forms along the IFF. In particular a strong anticyclonic meander is often present at the start of the front near the Iceland shelf (Hansen and Meincke, 1979; Smart, 1984; Allen et al., 1994). The sloping isopycnals of the IFF are balanced by the Faroe Current carrying Atlantic water east. It should be noted that the northwest-southeast orientation of the front/ridge means that eastward flow along the front is 'inflow' to the Nordic Seas.

Two relatively direct branches of inflow across the IFR are separated by a turbulent eddy field. At the northwestern end where the IFR intersects the Iceland shelf, a strong inflow is observed to feed the start of the current (Perkins et al., 1998). Perkins et al. (1998) estimate the Atlantic transport in this branch at 3.5 Sv, which is enough to supply the entire Faroe Current. This is inconsistent with observations suggesting that the inflow is fed at multiple locations along the IFF. In particular, a strong inflow is seen the eastern end of the IFR where it joins the Faroe Plateau (seen in the glider surveys described in this thesis as well as in Hansen and Østerhus (2000)). Rossby and Flagg (2012) find a total northward transport across the IFR of 4.4±0.25 Sv, the majority of which occurs at the eastern end of the IFR. The flow in the central IFR between the two fast branches is more sluggish and appears to be dominated by intense eddy activity (Rossby et al., 2009). North of the Faroe Plateau, the along front flow becomes more tightly focused. The long term mean transport of Atlantic water in the Faroe Current across 6°W north of the Faroe Islands is 3.5±0.5 Sv with negligible seasonality in Atlantic water transport (Hansen et al., 2003).

1.3 Circulation and Modification in the Nordic Seas

In the Nordic Seas the majority of the Atlantic inflow is carried north from the GSR in the two branches of the Norwegian Atlantic Current (NwAC). The outer (or baroclinic) branch of the NwAC is offshore approximately along the 2000 m isobath and feeds Atlantic waters to the interior of the Norwegian Sea (Orvik and Niiler, 2002). The inner (or barotropic) branch flows along the Norwegian shelf break and is often called the Norwegian Atlantic Slope Current (NwASC) (Skagseth et al., 2008).

Atlantic water in the Faroe current flows along north of the Faroe Islands until it reaches the northeast edge of the Faroe plateau. Here the IFR and FBC branches of inflow are fairly close together, separated by the width of the FSC entrance. The current and front lose their topographic guidance at that point. The majority of the Faroe Current flows into the outer branch of the NwAC (Hansen and Østerhus,

2000), but Rossby et al. (2009) show that a considerable amount can jump to the inner branch, the NwASC, which is fed mainly by the FSC inflow branch.

Most of the water mass transformation converting the Atlantic inflow into deep, dense water occurs in the Nordic Seas, not the Arctic (Mauritzen, 1996). The majority of the transformation happens in the deep Norwegian and Lofoten basins (Isachsen et al., 2005). These basins are isolated from the mean currents in the Nordic Seas and it appears that eddy transport plays a critical role in delivering warm, salty water from the boundary currents to the deep water formation regions (Isachsen et al., 2005; Spall, 2010).

1.4 Overflows at the GSR

Dense waters formed by diapycnal water mass transformation of Atlantic inflow to the Nordic Seas fill the basins to the north of the GSR. It is this reservoir which spills through gaps in the ridge and forms the dense gravity currents, or overflows, on the Atlantic side of the ridge. Combined with entrained Atlantic waters and convectively formed dense water in the Labrador Sea, the overflow across the GSR becomes the North Atlantic Deep Water that circulates globally in the deep ocean. The primary overflow pathways are through the Denmark Strait, across the IFR, and through the FSC to the FBC. The Denmark Strait and FBC overflows dominate the volume transport of dense water across the GSR. They differ considerably in properties, with the FBC (and IFR) overflow product (called Iceland-Scotland Overflow Water, ISOW) being considerably more saline owing to entrainment of saltier ambient waters than those which overlie the Denmark Strait overflow (DSO). This is an important property of overflows: the product water characteristics depend intimately not only on the conditions in the deep convection regions where dense water is formed, but also on the details and location of entrainment of ambient waters into the gravity currents themselves (Price and Baringer, 1994).

Dense overflows everywhere share some basic features. Overflows form at a topo-

graphic constriction, or sill, behind which a large volume of dense water accumulates. Flow accelerates at the sill and forms a swift near bottom plume. These plumes are often hydraulically controlled, where the upstream wave propagation speed is less than the flow speed and upstream locations cannot 'sense' downstream conditions (Pratt and Lundberg, 1991). Hydraulic jumps which occur in these flows can lead to signification turbulent entrainment. In flows large enough for rotation to be important the plumes adjust to geostrophic balance downstream of the sill and tend to flow along bathymetric contours. Modification of the plume properties tends to be most rapid in close proximity the sill, where turbulent mixing is enhanced as the flow accelerates and the plume is at its shallowest, entraining the most dissimilar waters it will encounter (Mauritzen et al., 2005). Two crucial components of overflow dynamics are the extent to which the source water mass is modified by entrainment of overlaying waters, and the amount of friction in the bottom boundary layer (BBL). The former process influences the eventual neutral depth of the overflow, the product water mass volume transport, as well as providing a pathway for changes in the ambient fluid to be communicated to the overflow and subsequently to the deep ocean. Friction in the BBL is important in breaking the geostrophic balance constraint of overflows, allowing them to descend across depth contours (Wåhlin and Walin, 2001). Both processes depend intimately on turbulent mixing, of heat/salt in the first case and momentum/stress in the second. Stress in the BBL and at the plume/ambient interface can also induce a cross stream helical flow which can influence entrainment Johnson and Sanford (1992); Umlauf et al. (2007); Seim and Fer (2011)

1.4.1 Denmark Strait overflow

The volume transport of the overflow through the Denmark Strait is about 2.9 Sv, roughly equal to the sum of the IFR and FBC overflows east of Iceland (Dickson and Brown, 1994). The DSO exhibits considerable variability on 2-5 day time scales, but, like the FBC, appears not to have a significant seasonal signal (Girton and Sanford,

2003). As is typically the case with dense overflows, entrainment greatly augments the DSO volume transport, to 5 Sv downstream of the sill. Mainly because the entrained ambient waters are colder, the DSO product is denser than the ISOW and underlies it where the two flow together near the southern end of Greenland.

1.4.2 IFR overflow

The IFR is wide, shallow gap in the GSR and overflow across the IFR is believed to be highly variable, occurring in many different locations. The canonical estimate of overflow transport across is ridge is 1 Sv (Hermann, 1967). Chapter 2 of this thesis presents an updated lower bound estimate (0.8 Sv) which is not in conflict with that of Hermann (1967). The overflow across the IFR has only been indirectly measured, and the uncertainty in the canonical estimate is large. The IFR is very broad compared to the Rossby radius, with the main flow oriented along the ridge axis, controlled by the orientation of the IFF and the bottom-following isopycnals of the overflow. The flow of dense water across the IFR is accomplished by cold core eddies shed by the IFF (Allen et al., 1994; Hansen and Meincke, 1979; Willebrand and Meincke, 1980) and by gravity currents flowing through notches in the ridge crest (Steele, 1959; Wilkenskjeld and Quadfasel, 2005). The most prominent of the gravity current IFR overflows occurs at the northwestern end of the ridge where it intersects the Iceland shelf. The region, known as the Western Valley, contains an intermittent, but strong, boundary current of overflow that travels southwest along the Iceland shelf break. Chapter 2 estimates the overflow transport in this branch to be 0.48 Sv, with significant variability on timescales of weeks or less. Observations of Perkins et al. (1994) show the WV overflow to have some eddy characteristics as well as gravity current structure. The overflow across the IFR immediately joins part of the FBC overflow on the Atlantic flank of the IFR, and the two currents travel downstream along the south of Iceland onto the Reykjanes Ridge on the way to joining the DSO in the Irminger Basin.

1.4.3 FBC overflow

The geometries of the FBC and IFR generate dynamically different constraints on the respective overflows, and lead to differences in the character of each. Unlike the IFR, the FBC is narrow and deep with a horizontal constriction with a width on the order of the local first mode Rossby radius of deformation, and is likely hydraulically controlled downstream of its sill (Girton et al., 2006; Pratt et al., 2007; Enmar et al., 2009). The FBC overflow is swift ($O(1\text{ m s}^{-1})$) and unidirectional, in a narrow current (10 km) with a bottom mixed layer of cold ($\approx$0°C) water capped by a thick ($O(100\text{ m})$) interfacial layer below the ambient Atlantic waters. Dissipation levels as high as 10^{-5} W kg^{-1} illustrate the energetic turbulence at work in the overflow causing significant water mass modification throughout the overflow process (Fer et al., 2010). Chapter 3 of this thesis will show that the highest levels of turbulence are found downstream of the sill where the overflow exits the FBC onto the Atlantic flank of the IFR. The long term mean overflow transport though the FBC is 1.9$\pm$0.3 Sv, and exhibits substantial variability on timescales of days but has little ($\sim 10\%$) seasonal or long term variability (Hansen and Østerhus, 2007; Darelius et al., 2011). Observations (Geyer et al., 2006; Darelius et al., 2011, 2013) and modeling studies (Riemenschneider and Legg, 2007; Seim et al., 2010) suggest that the FBC overflow develops mesoscale oscillations downstream of the sill which play a role in modulating turbulent mixing.

The FBC and IFR overflows join together and flow cyclonically along the northern and western edges of the Iceland Basin. Southeast of Iceland the total transport of the two overflows, known as Iceland Scotland Overflow Water, is 3.2 Sv in the depth range 1300-2100m (Saunders, 1996).

1.5 Circulation of the overflow waters in the North Atlantic

Subsequent to crossing their respective sills, the DSO and ISOW continue to flow along bathymetric contours, descending gradually into the deep ocean. The DSO

flows along the western slopes of the Irminger Sea, reaching a depth of 2000-3000 m near the southern tip of Greenland, transporting 4.5 Sv of overflow and entrained water (Bacon and Saunders, 2010).

The ISOW flows cyclonically around the Iceland Basin and travels southwest along the Reykjanes Ridge (RR) (Saunders, 1996). The traditional picture is that ISOW flows southwest along the RR, crossing into the Irminger Basin at the Charlie Gibbs Fracture Zone (CGFZ) (Swift, 1984; Harvey and Theodorou, 1986; Dickson and Brown, 1994; van Aken and Becker, 1996). However an inconsistency was observed between the measured volume transport southeast of Iceland (3.2 Sv, Saunders (1996)) and the ISOW transport through the CGFZ (2.4 Sv Saunders (1994)). A recent modeling study by Xu et al. (2010) suggest that a fraction of the ISOW flows west into the Irminger Sea through gaps in the RR north of the CGFZ, resolving the inconsistency.

The ISOW enters the Irminger Sea and begins to flow cyclonicly about that basin, joining the DSO at the southern tip of Greenland (Dickson and Brown, 1994) to form the Deep Western Boundary Current (DWBC). The canonical estimate of DWBC transport at Cape Farewell (the southern tip of Greenland) is 13 Sv, which includes both ISOW and DSO (Dickson and Brown, 1994). More recent estimates put the Cape Farewell DWBC transport at 9 Sv, and suggest that this represents a statistically significant reduction from the earlier 13 Sv value (Bacon and Saunders, 2010).

1.6 Climate Impacts of Cross Iceland-Scotland Ridge exchanges

The overflows across the GSR and deep convection in the Labrador Sea produce NADW, feeding the lower branch of the AMOC. Along with Antarctic Bottom Water, the NADW transported by the AMOC fills a large part of the worlds abyssal ocean (Johnson, 2008). The production of this water mass ventilates the deep ocean and stores properties (like heat, salt, and dissolved gasses) which are acquired from contact with the atmosphere. Additionally, the production of NADW is responsible for a

poleward heat transport of 0.6 PW in the North Atlantic, a substantial amount of the total oceanic heat transport (Talley, 2003).These characteristics make the circulation and production of NADW, the lower branch of the AMOC, important components of the global climate system. Modeling studies suggest that changes in the AMOC can project onto global climate via changes in sea surface temperature (Danabasoglu et al., 2010). Abrupt climate change events in the paleo record have been attributed to changes in the AMOC (Broecker, 2003). Understanding the downwelling branch of the AMOC, part of which is investigated in this thesis, is critical to our knowledge of global ocean circulation in general, and to our ability to predict future conditions in a changing climate.

1.7 Overview of Chapters

The analysis contained in each of the chapters of this thesis derive from a field program completed between November 2006 and November 2009. Seaglider autonomous underwater vehicles were deployed approximately four times per year in the region surrounding the Faroe Islands with a goal of investigating the cross-ridge exchanges. The chapters of the thesis investigate different aspects of the resulting data. The first two chapters have been published in the Journal of Physical Oceanography as Beaird et al. (2012) and Beaird et al. (2013), the final chapter is in preparation to be submitted for publication.

Chapter 2 is concerned primarily with the overflows (FBC and IFR) on the Atlantic side of the IFR. It presents observations of the mean structure of the overflow current, and briefly comments on variable features. The analysis shows that the second sill of the FBC coincides with the largest changes in the FBC overflow plume, including significant thinning, widening and entrainment. Between the second sill and a topographic feature 75 km downstream, the plume bifurcates with the densest portion (65% of the transport), descending below 1000 m. On the IFR, near bottom velocities are directed along-slope with speeds averaging 21.5 cm s^{-1}. Obser-

vations indicate 80% of baroclinic velocities associated with mesoscale variability of the overflow plume are smaller than the along-slope topographically-induced circulation. Evidence of overflow is found at all locations on the Atlantic flank of the IFR, however the meridionally oriented portion at 13°W has anomalously warm bottom water, and divides FBC and eastern IFR overflow from overflow found in the Western Valley. Individual Seaglider sections identify IFR overflow in a narrow current (8-14 km wide) along the Iceland shelf with a mean transport of 0.43 Sv with significant variability over days to weeks. A lower-bound estimate of 0.8 Sv of total IFR overflow is presented.

Chapter 3 deals with the turbulent mixing which is so crucial to the evolution of the overflow plumes. The Seaglider observations are used to map the distribution of dissipation of turbulent kinetic energy on the Iceland-Faroe Ridge. A method is developed using the finescale vertical velocity and density measurements from the glider to infer dissipation of turbulent kinetic energy. The method, termed the Large-Eddy Method (LEM), is compared with a microstructure survey of the FBC. The LEM reproduces the patterns of dissipation observed in the microstructure survey, which vary over several orders of magnitude. Agreement between the inferred LEM and more direct microstructure measurements is within a factor of two. Application to the 9432 dives which encountered overflow waters on the IFR reveals three regions of enhanced dissipation: one downstream of the primary FBC sill, another downstream of the secondary FBC sill, and a final region in a narrow jet of overflow along the Iceland shelf break.

Chapter 4 investigates the seasonal flux of low salinity mesoscale features across the IFF. This chapter is different from the others in that it deals primarily with upper level circulation above the overflow. Seaglider observations reveal a process of subduction of low salinity waters (termed Low Salinity Frontal Water, LSFW) at the IFF. The features form thermohaline intrusions between the MNAW layer and the IW layer (or overflow when IW is not present). LSFW thermohaline intrusions are

observed only between November and February, and only on the IFR outside the FBC outflow region. The onset of the LSFW flux coincides with the development of deep surface mixed layer south of the front. It is posited that a combination of Mixed Layer Instability (Boccaletti et al., 2007) and internally driven frontal instabilities (Spall, 1995) drive the LSFW flux. Using an assumed ageostrophic vertical velocity, annual average heat and salt fluxes due to LSFW are estimated to be 0.3 to 1.1 $\mathrm{g/(m^2 s)}$ and 0.65×10^4 to $2.65\times10^4\,\mathrm{W\,m^{-2}}$. The estimates are slightly smaller, but comparable to previous estimates due to intrusive interleaving Hallock (1985) and mesoscale eddies (Willebrand and Meincke, 1980; Allen et al., 1994).

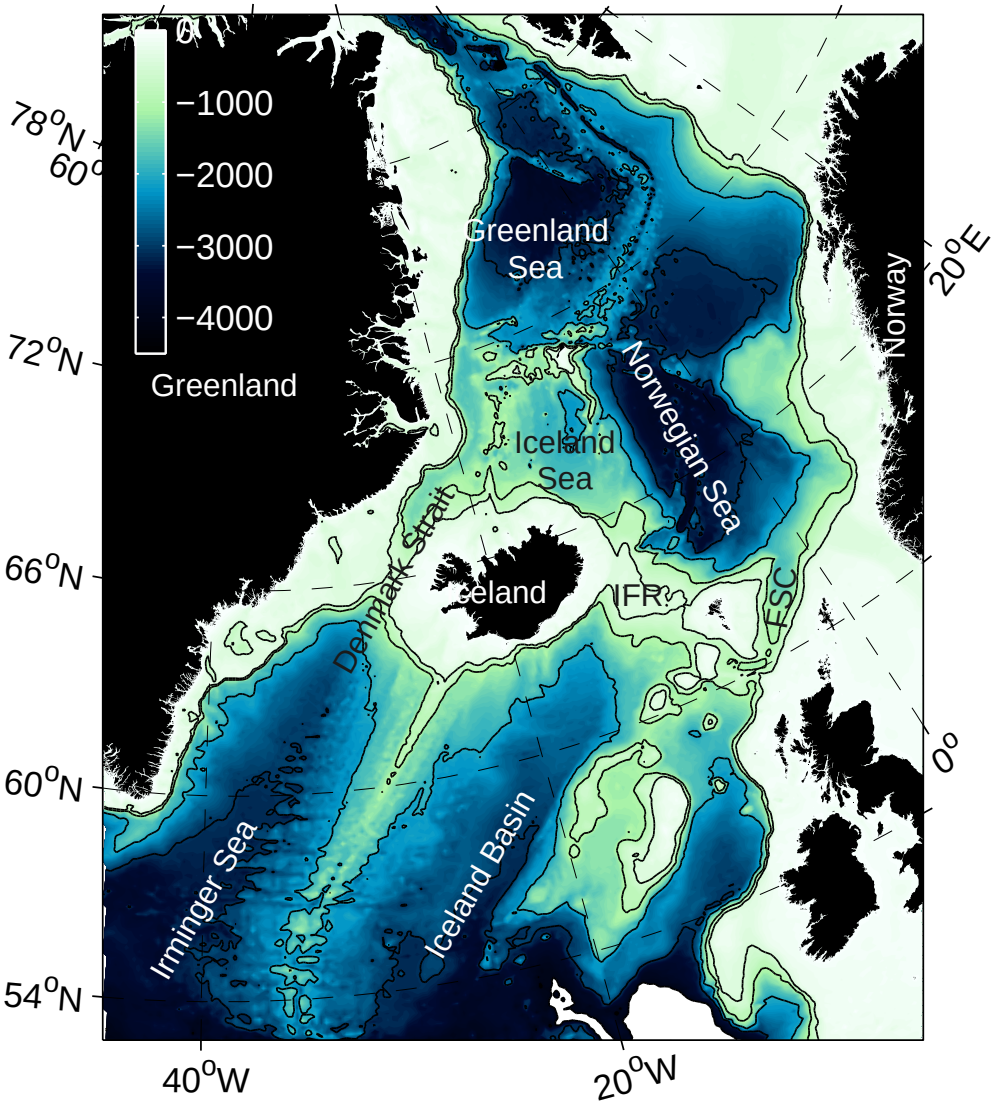

Figure 1.1: Bathymetry of the northern North Atlantic and Nordic Seas.

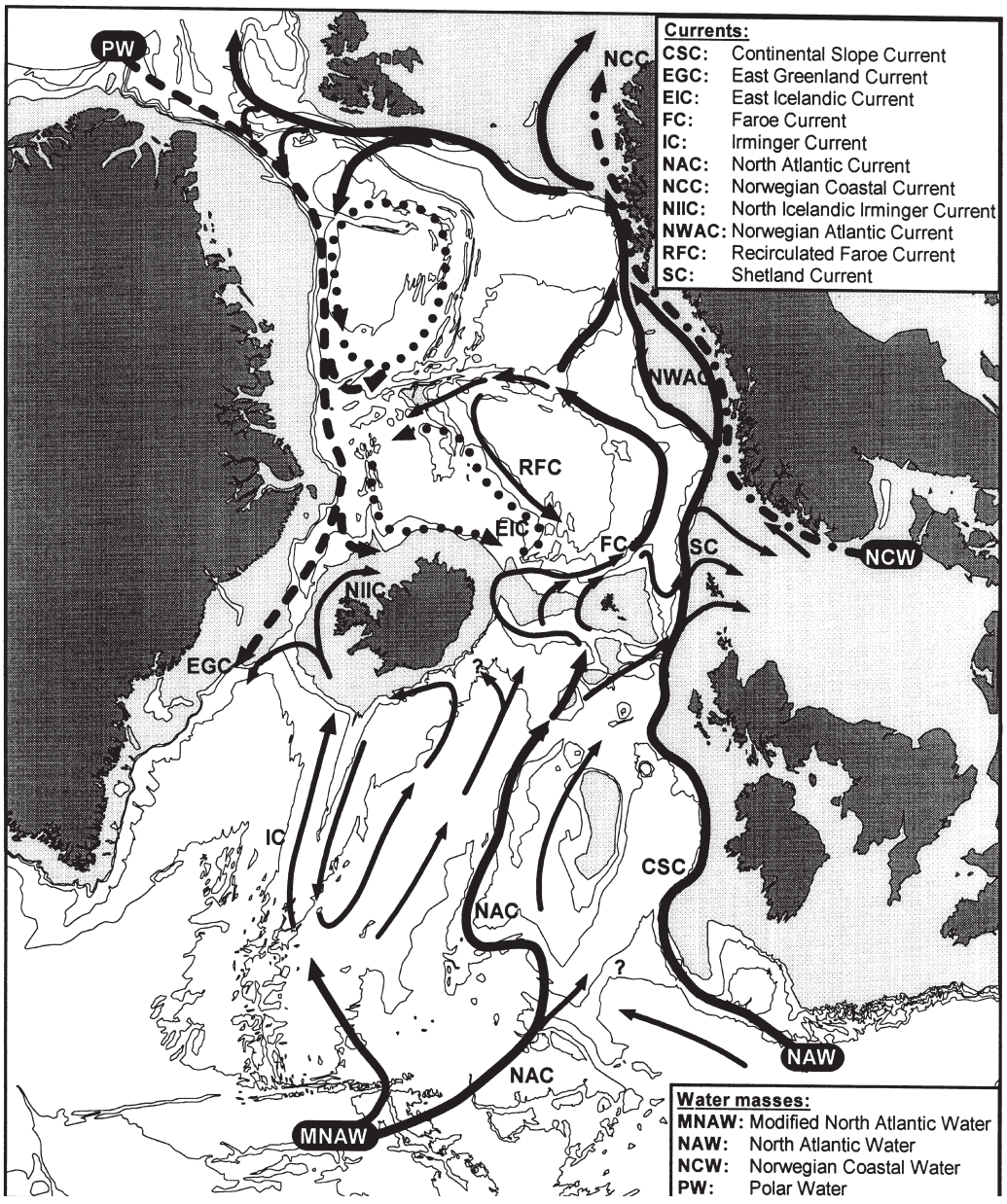

Figure 1.2: Schematic surface circulation from the review paper by Hansen and Østerhus (2000). Acronyms for currents and water masses are labeled in the Figure.

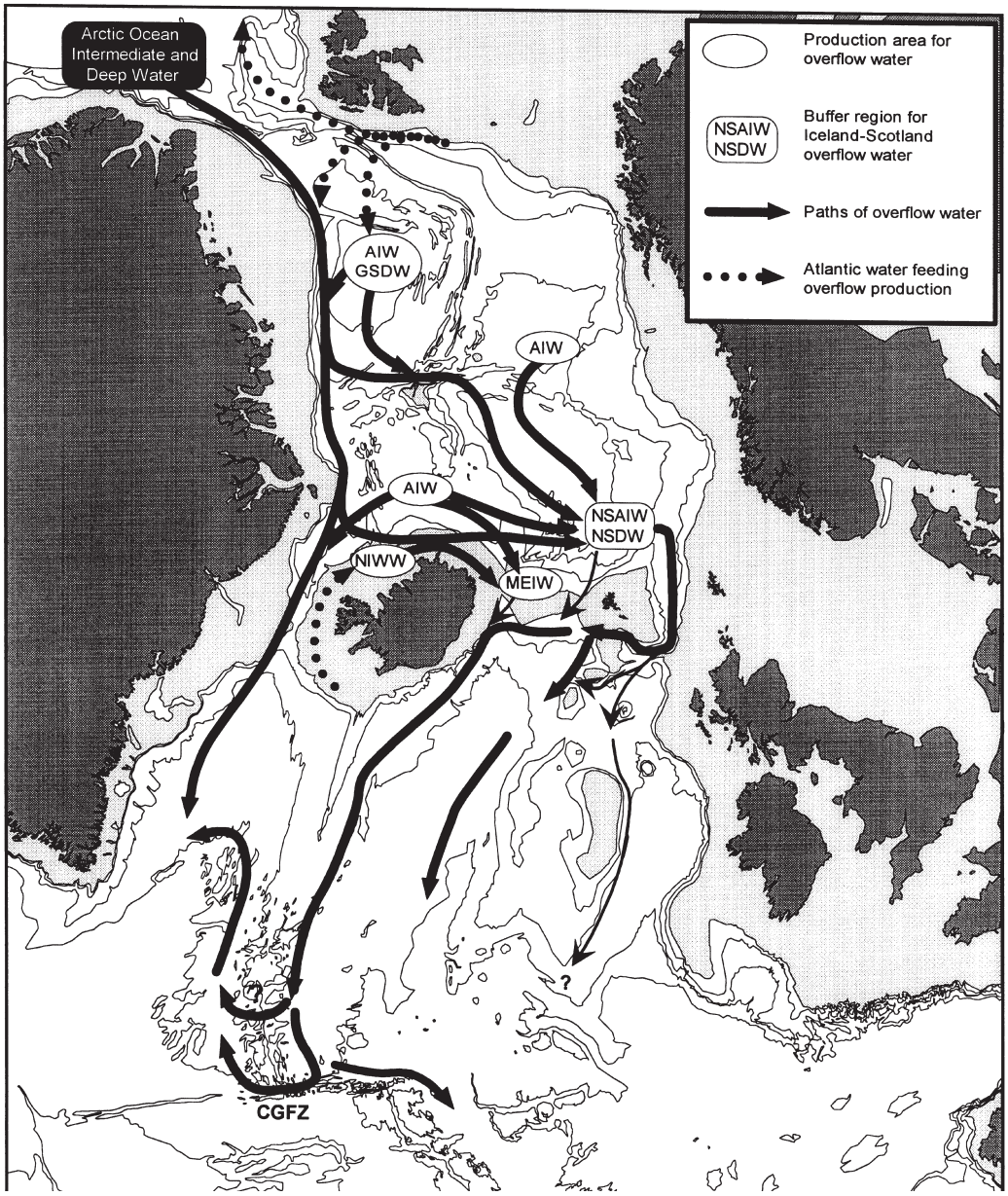

Figure 1.3: Schematic deep circulation from the review paper by Hansen and Østerhus (2000). Abbreviations are given for a number of water masses involved in the overflow of dense water from the Nordic Seas to the North Atlantic: Arctic Intermediate Water (AIW); Greenland Sea Deep Water (GSDW); North Icelandic Winter Water (NIWW); Modified East Icelandic Water (MEIW); Norwegian Sea Deep Water (NSDW); Norwegian Sea Arctic Intermediate Water (NSAIW). The Charlie Gibbs Fracture Zone is labeled CGFZ.

Chapter 2

OVERFLOW WATERS AT THE ICELAND-FAROE RIDGE OBSERVED IN MULTI-YEAR SEAGLIDER SURVEYS

2.1 Introduction

The Greenland-Scotland Ridge (GSR) forms a continuous barrier over which both cold and warm water exchange between the North Atlantic and the Nordic Seas is confined to the upper ocean (≤ 850 m). Poleward of the ridge the Nordic Seas are filled with cold recently ventilated waters, while to the south the North Atlantic is warmer and saltier at the same depths. The GSR is split by Iceland into eastern and western regions, with overflow of dense Nordic origin waters occurring on both the western side, though the Denmark Strait, and the eastern side, across the Iceland-Faroe Ridge (IFR) and the Faroe Bank Channel (FBC) (Fig. 2.1, Table 2.1). A small volume of dense water also overflows the Wyville Thomson Ridge southeast of the Faroe Islands. The overflows combine with Labrador Sea Water to form North Atlantic Deep Water (NADW), a major constituent of the global abyssal ocean (Johnson, 2008). Above the IFR the warm and cold branches of the Atlantic Meridional Overturning Circulation (AMOC) are squeezed into close contact (Fig. 2.2). Because the ambient stratification through which a dense plume descends controls many of the plume's properties, including its eventual detrainment depth (Price and Baringer, 1994), the arrangement of cold and warm waters of the AMOC on the IFR has implications for the abyssal circulation of a large part of the Atlantic ocean. The behavior of these dense overflows is critical to the large scale ocean circulation.

The waters around the Iceland-Faroe Ridge have been the focus of intense study dating back to the early 20$^{\text{th}}$ century (Hansen and Østerhus, 2000). This paper

reports on the mean circulation of eastern overflows that occur across the Iceland-Faroe Ridge and through the Faroe Bank Channel, based on three years of intensive hydrographic surveys by Seaglider autonomous underwater vehicles. Seagliders collected more than 17,400 hydrographic profiles between November 2006 and November 2009 in three-month missions begun quarterly near the Faroe Islands. These surveys greatly increase the quantity of data available on the IFR, especially downstream of the FBC. The spatial resolution of the surveys (from 3 to 6 km) is a considerable improvement over past shipboard studies. We are able to establish our methods by comparing our observations to well-known values (e.g. FBC overflow transport), while the extent and resolution of the Seaglider data allows us to improve understanding of the distribution and transport of the overflows on and across the IFR, establish variability of certain overflow features, and identify regions of dynamical significance to the overflows.

The eastern overflows are principally composed of three source water masses (Fig. 2.3, Table 4.1): Norwegian Sea Deep Water (NSDW), Norwegian Sea Arctic Intermediate Water (NSAIW) and Modified East Icelandic Water (MEIW) (Hansen and Østerhus, 2000; Fogelqvist et al., 2003). Faroe Bank Channel overflow derives primarily from NSAIW and NSDW sources with a small quantity of MEIW. The IFR overflow contains nearly equal amounts of the three constituents (Hansen and Østerhus, 2000). During the overflow process mixing and entrainment transform the source waters into a product known as Iceland-Scotland Overflow Water (ISOW), a mixture of MEIW, NSDW, NSAIW and entrained Modified North Atlantic Water (MNAW). The overflow transport roughly doubles due to entrainment and the ISOW attains properties of Θ between 2.7 and 2.9°C and S approximately 34.92 with a potential density $\sigma_\theta \geq$27.8 kg m^{-3}. Following Hansen and Østerhus (2000), *inter alios*, overflow waters will be defined as those with potential density, σ_θ, $\geq$ 27.8 kg m^{-3}, a criterion often used to define ISOW farther downstream.

The IFR is approximately 400 km wide with a crest depth varying around 450 m

(Fig. 2.1). In contrast, the FBC is 840 m deep, and narrows to 10 km at its primary sill. The eastern overflows are partitioned unequally between the two passages. The canonical estimates of overflow flux are 1.9±0.3 Sv and 1 Sv for the FBC and IFR respectively (Hansen and Østerhus, 2007; Hermann, 1967). The FBC overflow exhibits a seasonal variation of about 10% of the mean, with a maximum in late summer (Hansen and Østerhus, 2007). No estimate of variability is available for the IFR overflow.

The FBC and IFR overflows have different dynamical constraints. The FBC is narrow and deep with a horizontal constriction width on the order of the local first mode Rossby radius of deformation, and likely exhibits hydraulic control (Girton et al., 2006; Pratt et al., 2007; Enmar et al., 2009). The IFR, on the other hand, is very broad compared to the Rossby radius, with the main flow oriented along the ridge axis, controlled by the orientation of the Iceland-Faroe Front (Fig. 2.2). Cross-ridge flow occurs by eddy flux or in small topographic depressions (Steele, 1959; Hansen and Meincke, 1979; Hermann, 1967; Allen et al., 1994). One of these depressions, referred to as the Western Valley (WV), is located where the IFR joins the Iceland shelf and was repeatedly occupied in this survey, revealing large overflow transport variability.

After passing to the Atlantic side of the GSR, each overflow turns to its right and begins to flow along isobaths under the influence of the pressure gradient and Coriolis forces. The overflow appears as a bottom-intensified current on the Atlantic Flank of the IFR (AIFR) with capping isopycnals lying approximately parallel to the bottom slope (Fig. 2.2) in geostrophic balance with the along-slope current. The vertical density structure over the AIFR includes a thick [$O(100$ m$)$] transitional pynocline between weakly stratified Atlantic and overflow layers (see e.g. Fig. 2.10). The overflow layer is typically ~ 100 m thick and often includes 10-50 m thick well mixed bottom boundary layer, in which bottom stress on the overflow reduces the along-slope velocity creating an imbalance between the Coriolis and pressure gradient

forces. In the resulting Ekman balance, the along-slope vertical shear stress permits the geostrophically adjusted plume to have a downslope velocity component in the boundary layer (Gill, 1982). Eventually the ISOW will descend from sill depths of 500-800 m to 2000-2500 m as it circulates cyclonically in the Iceland Basin (Harvey and Theodorou, 1986; Saunders, 1996; Fogelqvist et al., 2003), crosses the Reykjanes ridge and joins the Denmark Strait overflow in the Irminger Basin. A small portion may recirculate in the Iceland Basin (Harvey and Theodorou, 1986). The rate of descent is intimately related to the levels of turbulent bottom stress in the plume bottom boundary layer. The overflow entrains ambient waters all along its path, but by far the greatest changes in properties occur in the first few hundred kilometers from the sill where turbulence driven diapycnal mixing is highest and plume/ambient property differences are largest (Swift, 1984; Price and Baringer, 1994).

This paper assesses the three-year mean flows as well as the variability of overflow plumes in terms of their instantaneous thickness and temperature. Whether or not the plumes remain continuous, or break into a series of lenses or eddies as they flow away from the sill remains an important dynamical question. Observations show a strong oscillation of the FBC overflow with a period of approximately 88 hours (Geyer et al., 2006; Darelius et al., 2011) indicating spatial and temporal variability in the plume. High resolution regional models suggest that the FBC overflow plume breaks into eddies (Riemenschneider and Legg, 2007; Seim et al., 2010). Observations presented here (section 2.52.5.3) and others (Prater and Rossby, 2005) suggest that farther downstream on the IFR the plume does not appear as a series of isolated propagating eddies.

2.2 Data

Observations considered here were obtained using Seaglider long-range autonomous underwater vehicles. Seagliders are small buoyancy-driven vehicles that profile as deep as 1000 m in a sawtooth pattern, ascending and descending with a typical verti-

cal to horizontal glide ratio of 1:3 (Eriksen et al., 2001). The Seagliders carried Sea-Bird Electronics conductivity (SBE 4) and temperature (SBE 3) sensors, a Wetlabs BB2FVMG optical puck with two wavelengths of backscatter as well as fluorescence, and a Sea-Bird Electronics Model 43 oxygen sensor. The accuracy of the salinity measurement is 0.01. Corrections are applied to the temperature and conductivity measurements to compensate for thermal-inertia and flushing speed issues arising from the unpumped conductivity and temperature sensor (Eriksen, in prep.). Between surfacings the vehicle navigates by dead reckoning based on a flight model that makes use of an on-board compass and three-axis accelerometer. An estimate of depth-averaged horizontal current (DAC) may be obtained from the vector difference between the dead-reckoned displacement over a dive/climb cycle and the geographic displacement based on GPS fixes at the start and end of each cycle. Thus each Seaglider sawtooth, or 'dive cycle', results in two slant-vertical profiles of water column properties and one estimate of DAC. During the Faroes mission, conductivity and temperature were sampled at 20 second intervals. With typical vertical vehicle speeds of 6-10 cm s^{-1}, the vertical resolution was approximately 1.2-2 m. The horizontal separation of these slanted profiles varied with depth, but adjacent Seaglider surfacing locations are separated by 3-6 km. An acoustic altimeter mounted forward on the Seaglider was used to detect and avoid the seafloor. In order to fully sample the overflow plume, gliders in this survey were programmed to begin their dive-to-climb transition 10 m above the acoustically ranged bottom depth. In practice they turned within a few meters of the seafloor and occasionally collided with it.

Between November 2006 and November 2009, 23 successful Seaglider deployments were made resulting in ∼17,400 profiles of temperature, salinity, oxygen, red and blue backscatter, fluorescence and DAC in the Iceland-Faroes region. Of these, 16 deployments were on the AIFR and will be discussed in this paper. The remainder of the deployments were made either north of the Faroes, or in the Faroe-Shetland Channel. The average deployment length was 76 days (set by ship's schedule), covering about

2000 km. Seaglider deployments and recoveries were made quarterly from the *R.V. Magnus Heinason* during the regular hydrographic surveys conducted by the Faroe Marine Research Institute (FMRI). On average two Seagliders were deployed on each cruise.

A plot of bottom temperature (Fig. 2.4) shows the distribution of glider dives. Seagliders were typically deployed near the FBC where they remained for a few days as the shore-based pilot trimmed flight parameters to adjust glider pitch, roll, and buoyancy control. Gliders were then flown along a target isobath of the AIFR, from the FBC in the southeast to the Icelandic shelf break in the northwest. Most missions targeted isobaths between 600 and 900 m on the AIFR, and occasionally ridge-normal sections were occupied, as can be seen in Figures 2.2 and 2.4. Strong depth averaged currents on the IFR made precise repeat sections impossible.

2.3 Methods

To describe the transport and structure of the eastern overflows in the multi-year mean thirteen composite sections were created running the length of the IFR from the mouth of the FBC to the Iceland shelf break (Fig. 2.1). Each section spans the 600 to 900 m isobath and is oriented approximately parallel to the local bathymetric gradient so that cross sectional geostrophic velocities would be parallel to the plume velocities. On the AIFR a substantial part of the FBC outflow descends below 900 m into the Iceland basin, therefore the composite sections do not capture the entire width of the plume beyond the FBC terminus. Some overflow is lost between consecutive sections due to downslope Ekman drainage and some overflow is gained from the IFR crest.

Sections of potential density, temperature and salinity were calculated as follows: Each section has a horizontal grid spacing of 500 m and vertical spacing of 10 m. A single grid point average is found by taking all Seaglider data at the same depth within a radius L. These data were then subsampled by including only observations below

which the bottom depth is within a vertical height H of the bottom depth at the grid point. Subsampling by the bottom-depth criterion reduces the cross-slope length scale of averaging. When averaging on depth surfaces, this anisotropy is desirable because dense overflow isopycnals are 'draped' over the AIFR, lying nearly parallel to the sloping bottom (Fig. 2.2). All observations that meet the above criteria are averaged to obtain an estimate at the grid point. For sections on the AIFR, $L = 15\,\mathrm{km}$ and $H = 40\,\mathrm{m}$. With typical IFR slopes of 1/100, $H = 40\,\mathrm{m}$ implies a cross-isobath averaging length of 4 km. In the Faroe Bank Channel region (sections I through III) and at the Iceland shelf break (section XIII) the averaging length scales used are $L = 5\,\mathrm{km}$ and $H = 100\,\mathrm{m}$, chosen to better suit the steeper topography and narrower current features observed in these regions.

Profiles of relative geostrophic velocity normal to each composite section were calculated from the average density. Reference velocities were created by averaging the Seaglider estimates of DAC using the H and L criteria described above. The depth average of the relative geostrophic velocities at a grid point was adjusted to match the cross sectional component of the average DAC at that point, resulting in a profile of absolute geostrophic velocity. In order to account for reductions to along-slope transport by friction near the bottom, an Ekman layer was imposed on the velocity profiles in a bottom boundary layer. It is assumed that the near bottom geostrophic flow is predominantly perpendicular to the sections. An estimate of Ekman layer thickness was made by averaging the bottom mixed layer depth from each of the density profiles associated with a grid point (typically 10-50 m thick). We subtract an average Ekman layer velocity from the profile of geostrophic velocity in the boundary layer, given by

$$\overline{u_{ek}} = \frac{C_d U_{tbl}^2}{f\delta} \tag{2.1}$$

where $C_d = 2.5 \times 10^{-3}$ is a drag coefficient, U_{tbl} is the geostrophic speed at the top of the boundary layer, δ is the Ekman layer thickness, and f is the Coriolis parameter. This is simply the textbook Ekman transport with a quadratic drag parameterization,

divided by the layer thickness to get an average velocity.

Uncertainty of the transport through the composite sections was assessed by a Monte Carlo approach. We consider the uncertainty of the components of the geostrophic velocity: the cross-sectional component of DAC; and the averaged density field (connected via thermal wind to velocity). We calculate the transports of an ensemble of sections with perturbed density and reference velocities, in which perturbations are based on the uncertainties of the average quantities. The procedure is as follows: a single section in broken into a group of smaller segments each 4 km wide. The number of glider dives which fall within the end points of each segment is used as the number of degrees of freedom (DOF) for standard error estimates. Two sets of random normal variables (100 values each) are produced for each 4 km segment, one to perturb the DAC reference velocity and one to perturb the densities. At each grid column in the segment (there are 8 columns per segment) an ensemble of perturbed reference velocities is created by taking the mean cross track component of DAC, and adding to it the random normal distribution multiplied by the standard deviation of the DAC divided by the square root of the DOF. Thus at each grid column there is a distribution of reference velocities with the statistics of the mean value and its standard error. The choice to use a 4 km wide segment with the same random number distribution was made to mimic correlation between adjacent points, and to be consistent with the averaging scheme used originally. The second random normal distribution is used in the same way (mean plus random distribution times standard error) at every grid point, (x, z) to create an ensemble of perturbed densities. The result is 100 sections of randomly perturbed density and reference velocity. We calculate the absolute geostrophic velocities and transport for each one, and report the standard deviation of the results as uncertainty bars on the mean transport estimates.

Additionally, the DAC observations, whose distribution is that of the points in Figure 2.4, are statistically interpolated onto a regular grid to produce the near bottom circulation map in Figure 2.12. Statistical interpolation, described by (Bretherton

et al., 1976), relies heavily on the spatial covariance between the data and itself and between the data and the grid points to produce an estimate at a grid point given by a weighted linear combination of all observations.

2.4 Faroe Bank Channel

The Faroe Bank Channel is the deepest gap in the GSR, and roughly two-thirds of the flux of eastern overflow waters pass through its narrow channel walls. The following section compares Seaglider observations of the long-term structure of the overflow with some of the numerous previous FBC studies. Transport estimates made assuming geostrophic balance compare well with the estimates of Hansen and Østerhus (2007), who utilized long-term moored velocity measurements upstream at the FBC sill. The increased spatial resolution of the Seaglider data defines in greater detail the structure of the FBC overflow downstream of the sill, indicating dynamically significant regions of plume thinning and bifurcation.

2.4.1 FBC Composite Section

Synthetic Section I is located approximately 20 km downstream of the sill (Fig. 2.5a), near section E of Mauritzen et al. (2005), section B of Fer et al. (2010), and section P of Duncan et al. (2003). Figure 2.5 shows plots of DAC, potential temperature, and absolute geostrophic velocity along the section. Because of the averaging method described above, transports and overflow characteristics should be interpreted as reflecting the mean conditions 5 km upstream and downstream of the section in Figure 2.5a.

The temperature section (Fig. 2.5b) displays the classic shape of the FBC overflow with deeper isotherms on the Faroe Bank side of the channel sloping upwards towards the Faroe Plateau side. In addition to the isotherm tilt, past synoptic sections have revealed interface stratification that is higher on the Faroe Bank side of the channel than on the Faroe Plateau side (Hansen and Østerhus, 2000). This isopycnal pinching,

attributed by Johnson and Sanford (1992) to a secondary frictionally-driven helical flow, is partially obscured by averaging in the synthetic section. However, the mean buoyancy frequency at the 3°C isotherm averaged from individual profiles decreases from 4.3 cycles per hour (cph) on the Faroe Bank side of the channel to 2.7 cph at the Faroe Plateau side (not shown). The cross-channel gradient in the interfacial stratification is a result of the secondary circulation in which bottom water is advected to the left of the main overflow (looking downstream) in a frictional Ekman layer and returned by an interior transverse flow balanced by downstream isotherm tilt (see Figure 4 in Seim and Fer, 2011). At the Faroe Plateau-edge of the plume the tendency for the Ekman transport to pull less dense interfacial waters into the bottom Ekman layer may lead to overturning and increased mixing (Seim and Fer, 2011).

Depth-averaged flow in the FBC is oriented along the channel with speeds up to $\sim$ 30 cm s^{-1} (Fig. 2.5a). The high speeds of the baroclinic overflow dominate the DAC, however Figure 2.5c also shows some barotropic flow. Cyclonic shear across the channel is apparent in the layer above the overflow, with more upstream flow on the Faroe Bank side of the channel, as has been reported previously (Hansen and Østerhus, 2007). The total mean geostrophic transport of waters denser than 1027.8 kg m^{-3} through Section I is 1.8$\pm$0.2 Sv, where the uncertainty come from the standard deviation of the Monte Carlo results described in the Methods. The estimate is in agreement with the long-term average of 1.9 ± 0.3 Sv measured at the sill by moored ADCPs (Hansen and Østerhus, 2007), though it might have been expected that entrainment would increase the transport at Section I relative to the primary sill transport (20 km upstream). Averaging is done on depth surfaces and despite the attempt to compensate for the shorter cross slope decorrelation length by using the H criterion, horizontal averaging works to flatten isopycnal tilt. Reducing the averaging length scale increases the cross-channel isopycnal tilt, but drastically reduces the data available for the composite section. As a consequence, the overflow transport estimate reported here is a lower bound for the three-year mean.

Section I transport may also be compared with the synoptic sections E of Mauritzen et al. (2005) and B of Fer et al. (2010), each of whom use $\sigma_\theta \geq 27.65$ kg m^{-3} to define the overflow. Mauritzen et al. (2005) estimate the instantaneous overflow to be 2.0 Sv, which is slightly lower than our long-term estimate of 2.35 Sv (re-calculated for waters with $\sigma_\theta \geq$27.65 kg m^{-3}). Fer et al. (2010) also report a transport of approximately 2 Sv at their section B. The transport weighted mean ISOW ($\sigma_\theta \geq$27.8 kg m^{-3}) properties at Section I are $\Theta = 1.11$°C, $S = 34.96$ and $\sigma_\theta = 27.98$ kg m^{-3}. Section I shows the effects of entrainment of MNAW, diluting the mean plume values at the sill reported by Hansen and Østerhus (2007): $\Theta = 0.25$°C, $S = 34.93$ and $\sigma_\theta = 28.01$ kg m^{-3}. Seaglider vertical velocity observations which were used to infer dissipation of turbulent kinetic energy in the FBC (Beaird et al., 2012), revealed a 'hot spot' of mixing between the primary sill and composite Section I responsible for the observed dilution of mean plume properties.

2.4.2 FBC Exit

The FBC overflow plume encounters a secondary sill at the northwestern end of the FBC, beyond which the overflow spills onto the Atlantic side of the IFR. The plume undergoes significant changes in the region between the secondary sill and a topographic prominence approximately 65 km downstream ('bump', Fig. 2.6). In this region, the plume thins, bifurcates, and encounters elevated mixing.

An objective map of all Seaglider plume thickness observations (Fig. 2.6, top) illuminates several changes that occur as the overflow exits the FBC. Within the channel, the overflow plume is over 200 m thick, with the thickest part of the plume on the Faroe Plateau side of the channel. At the secondary sill (about 9°W), the plume thins to approximately 115 m, and spreads horizontally. This thinning corresponds to the point at which the plume flows onto the face of the IFR, evolving from an enclosed channel flow to a gravity current on a slope. Thinning and widening of the plume qualitatively suggests hydraulic control at the secondary sill. Plume widening is also

seen in the models of Riemenschneider and Legg (2007) and Seim et al. (2010), and is attributed in the former to a transverse hydraulic jump (Pratt et al., 2007). Using three techniques for calculating Froude numbers, Girton et al. (2006) find subcritical flow in much of the plume, observing supercritical values only in sections at, and just beyond, the secondary sill.

Between the secondary FBC sill and the 'bump', the overflow plume bifurcates into a shallow and deep branch. A portion of the overflow is funneled around the bump to the north, and a larger portion flows to the south into deeper water (across the pink contour in Fig. 2.6). The shallow pathway is seen as a relatively thick branch ($\geq$100 m) extending northwest from the bump in Figure 2.6. The continuation of the deeper branch is not shown in Figure 2.6 because it is below the maximum dive-depth of Seagliders. Thus, downstream of the intersection of the plume edge and the 1000 m isobath (pink contour in Fig. 2.6), the thickness map does not represent the full extent of the overflow (for observations of the deeper branch see Fig. 7 in Duncan et al. (2003) section S, and Fig. 3:108 in Hermann (1967)). The majority of the coldest overflow from the FBC follows the deeper branch. This is clear from the bottom temperature distribution in the bottom panel of Figure 2.6, where the coldest observations downstream of the FBC tend to follow a trajectory to the south of the topographic bump. In section 2.52.5.1 it will be shown that roughly 0.6 Sv (about a third of the transport at composite Section I) flows in the shallow branch.

The region of thinning, widening and bifurcation corresponds well to observations of enhanced mixing identified in discrete sections by Mauritzen et al. (2005) (100 km downstream of the primary sill) and Fer et al. (2010) ($\sim$80 km). Analysis of Seagldier vertical velocity data (Beaird et al., 2012) indicates that turbulent dissipation in the overflow plume is greatly enhanced in the region between the secondary sill and the topographic bump. This region of elevated dissipation is larger than, and distinct from, another located just downstream of the primary sill. Observations of Girton et al. (2006) and Fer et al. (2010) as well as model results of Riemenschneider and

Legg (2007) find critical Froude numbers in this region and suggest mixing produced by a 'wave regime' as found in the lab by Cenedese et al. (2004). Figure 2.6 shows bottom temperatures rise from around -0.5°C near the FBC primary sill to over 0°C just beyond the secondary sill (purple-to-blue transition). Much of the change occurs at and immediately beyond the second sill, evidence of increased entrainment of warm Atlantic water.

The abrupt changes that occur downstream of the terminus of the FBC suggest that, perhaps unsurprisingly, the secondary sill marks the most important transition region for the FBC overflow, where the majority of entrainment, watermass modification and dynamic adjustment occurs.

2.5 Iceland-Faroe Ridge

Beyond the Faroe Bank Channel the overflow plume spills out onto the Iceland-Faroe Ridge, which forms the northern boundary of the Iceland Basin. As the FBC overflow travels downstream it gradually descends deeper into the Iceland Basin as a consequence of frictional downslope transport. Observations of the pathways of descent are scarce, but a plausible picture emerges in the model results of Xu et al. (2010) (see their Fig. 7). By the time it reaches the slope south of Iceland the overflow is found between 1300 and 2300 m depth (Saunders, 1990; Fogelqvist et al., 2003). Along the crest of the IFR the FBC plume is joined by the weaker and more intermittent IFR overflow. It is difficult to distinguish between the FBC overflow and the IFR overflow because each share similar source waters having been mixed with the same overlying MNAW.

2.5.1 IFR Composite Sections

Figure 2.7a depicts the layers of ISOW density for each of the 13 composite sections shown in Figure 2.1. Each section is offset 300 m in depth. The figure indicates that, in the mean, isopycnals associated with dense overflow waters lie approximately

parallel to the topographic slope. The orientation of the isopycnals with respect to the ridge slope produces shear leading to bottom-intensified along-slope geostrophic flow in the overflow layer.

Figure 2.7b shows the depth of the 4.5° isotherm ($\sigma_\theta \approx 27.75$ kg m^{-3}) from individual dives. Variability of plume thickness about the mean is approximately constant across the slope. Substantial variability exists in the thickness of the overflow layer, however the general arrangement of isotherms parallel to bottom slope is a robust feature discussed later in Section 2.52.5.3.

The first three sections in Figure 2.7a indicate a rapid downstream decrease in the thickness of the ISOW layer. This decrease occurs as the overflow leaves the FBC, mainly between Sections II and III, which are located on either side of the secondary sill of the FBC. Large mixing and entrainment erode the densest waters. The first three sections are located upstream of the bifurcation, thus they cover the entirety of the overflow and any changes in mean properties must be due to entrainment of overlying MNAW (individual bottom temperature observations find the plume edges to be inside the bounds of these sections at all times,Fig. 2.6). The bifurcation occurs between Sections III and IV, where only a portion of the overflow remains above the 1000 m isobath. A significant loss of the densest waters between Sections III and IV suggests the densest part of the overflow follows the deeper branch (as in Fig. 2.6). Downstream of Section IV, thickness and mean density of the ISOW layer decline until Section XI, after which the ISOW layer grows as a result of the addition of IFR overflow water. The overflow layer is thinnest at Sections X and XI. This part of the AIFR, just beyond the bend near 13° W where the ridge becomes meridionally oriented, contains only a thin layer of overflow water.

Transport of overflow waters through all the composite sections is plotted in Figure 2.8. Included in the figure are transport estimates from various other studies, with error bars where included by the authors. The bounds on the composite sections are the result of the approach described in the Methods section. Assuming that the

overflow is entraining, the transport should increase downstream between Sections I, II and III where the entire plume width is covered. Figure 2.8, however, unexpectedly shows a decrease in transport at sections II and III. This decrease occurs in the region at, and downstream of, the secondary sill where dissipation is enhanced and hydraulic control takes place (Girton et al., 2006; Pratt et al., 2007; Fer et al., 2010; Beaird et al., 2012). The decreased transport through Sections II and III suggests that the turbulent plume is not in geostrophic balance in that region, and thus the assumptions made to obtain these transport estimates are not valid. The decrease occurs even when lighter ISOW density definitions are used, thus the decrease is not due to increased entrainment and transport in slightly lighter waters.

Between composite Sections IV and IX transport remains relatively constant at about 0.6 Sv; only about 33% of the total FBC overflow transport at composite Section I remains above 900 m depth after the bifurcation between Sections III and IV. This constitutes the shallow overflow branch mentioned previously. The remaining 67% of the FBC plume flows into the deep branch. The sections show the geostrophically balanced transports with a reduction in the boundary layer due to the modeled Ekman layer. The frictional ageostrophic flow in the bottom boundary layer should be directed down-slope into the Iceland Basin. This downslope flow can be estimated by integrating the Ekman balance equation over the boundary layer thickness and assuming the stress at the top of the layer is zero, leading to a down-slope transport per unit width of

$$\mathrm{V}_{ek} = -\frac{\tau_b^x}{\rho_o f} = -\frac{C_d U_{tbl}^2}{f} \tag{2.2}$$

where the bottom stress has been parameterized by a drag coefficient (C_d) and the square of the overlying along-slope speed (U_{tbl}) such that $\tau_b^x = \rho_o C_d U_{tbl}^2$. A rough calculation assuming $C_d = 2.5 \times 10^{-3}$ and $U = 21\,\mathrm{cm\ s^{-1}}$ (the AIFR mean, see section 2.52.5.3) suggests that the downslope Ekman drainage over the 146 km between sections IV and VIII is about 0.12 Sv. Thus, assuming along-slope flow, in the absence of additional overflow sources the transport between IV and VIII would decrease by

0.12 Sv. However, Figure 2.8 shows a possible increase of 0.2 Sv, implying about 0.3 Sv addition of IFR overflow. Between sections VIII and XI the transport diminishes from ∼0.75 Sv to ∼0.15 Sv indicating that most of the shallow branch of the FBC overflow and some accumulated overflow from the eastern IFR descend deeper into the Iceland basin in this region. Between sections XI and XIII the dense transport increases by 0.5 Sv. Because the overflow plumes must descend in the mean, any convergence of along-slope flow like this implies additional overflow from the IFR crest. We conclude from the composite sections that at least 0.5 Sv of overflow crosses the western portion of the IFR (sections XI to XIII) in the mean, and the above calculation suggests about 0.3 Sv of overflow across the eastern IFR (sections IV to VIII), bringing the total IFR overflow estimate to 0.8 Sv. This is considered an underestimate of the total IFR overflow as we are calculating the IFR overflow as a residual from convergences in along slope flow, and a simple downslope Ekman layer. Perhaps other ageostrophic contributions to the IFR overflow are missed, but the 0.8 Sv estimate compares moderately well with the (highly uncertain) canonical estimate of 1 Sv for IFR overflow (Hermann, 1967).

2.5.2 Distribution of Overflow on the IFR

Figure 2.9 shows the mean (left panel) bottom potential temperatures and minimum (right panel) potential temperature anomaly from the mean in 7.5×7.5 km boxes on the AIFR. In the mean the FBC overflow stands out clearly, with a bottom layer colder than 1°C extending to the topographic bump near 10°W. The coldest overflow, with temperatures ≤0°C are, in the mean, diluted downstream of the primary FBC sill. A layer colder than 3°C stretches downstream to about 12°W. The meridional arm of the IFR (at about 13°W) is warmer, with the near bottom temperatures averaging between 3-5°C. Maps of overflow layer thickness from three surveys of the OVERFLOW '60 experiment likewise show the meridional portion of the IFR with a thin covering of cold water (Hermann, 1967, Fig. 3:108). Previous studies have

identified the northwestern-most depression in the IFR, the Western Valley, as a site of frequent overflow (Perkins et al., 1998). The appearance of a thin stripe of low (relative to regional means, $\leq 3°C$) mean temperatures along the 500 m isobath of the Iceland shelf break provides evidence for this pathway of IFR overflow. This ribbon of low-temperature overflow is isolated from similar temperatures upstream, to the southeast, by the high mean temperature region of the meridional arm of the AIFR. Thus the source of the shelf break overflow must be local, implicating the WV region.

The minimum temperature anomaly field in the right panel of Figure 2.9 adds information about the variability of the overflow circulation on the AIFR. The minimum temperature anomaly in the FBC is small compared with the rest of the AIFR. The large minima along the southwestern edge of the FBC are due to the coarse spatial bins overlapping the relatively sharp plume edge in that region. On the AIFR outside the FBC, the magnitude of the minimum temperature anomalies increases, indicating variability in the amount of mixing and entrainment which has taken place in the plume at a particular location. The Western Valley exhibits the coldest minimum anomalies, reflecting strong variability of the WV overflow. Figure 2.9 agrees the results of mean sections reported by Meincke (1972), indicating warmer near bottom temperatures on the meridional portion of the IFR, and enhanced variability on the eastern half of the IFR and at the Iceland shelf break.

Potential temperature depth-profiles and temperature-salinity (Θ-S) plots from the four boxes outlined in black in Figure 2.9 are shown in Figure 2.10. These profiles are included to show instantaneous profiles, and point out variable and persistent features of the overflow. In the background of each panel are profiles from the upper 800 m of both the Nordic Seas (blue) representing the source of the overflow, and from the Iceland Basin (red) showing ambient conditions around the plume on the AIFR. The boxes are chosen arbitrarily, but each is along the 750 m isobath, and each represents a different region of the IFR: The FBC (box 1), a mid-IFR location (box 2), the meridional arm region (box 3), and the Western Valley (box 4). Profiles in each

box all have the characteristic deep pycnocline of the overflow plume implying that if the overflow plume propagates as a series of isolated eddies or lenses of cold water (as in Nof et al., 2002) these lenses are features superposed on a thin, continuous, sheet of overflow.

The intensity of the stratification varies, as does the temperature and mixed layer depth of the plume layer. Taking the bottom mixed layer (BML) to be the height above bottom (HAB) where the temperature differs from the bottom-most value by 0.1°C, the stratification in the interfacial layer (0.05-0.1 °C m^{-1}) ensures that BML thickness, even with this coarse definition, will be overestimated at most by a few meters, a small percentage of BML thickness anywhere in the FBC or on the IFR. The profiles of box 1 show thick BMLs (∼150 m), low BML temperatures (-0.4 to -0.1°C), and thick interfacial pycnoclines (∼200 m). Box 1 has little temperature variability with respect to downstream locations, however BML thickness varies from 125 m to 180 m. Boxes 2 through 4 exhibit enhanced plume temperature variability. Plume temperature is at a maximum in box 3, while box 4 clearly contains recent cold overflow from the IFR. The appearance of lower salinities at intermediate density in boxes 2-4 suggest the presence of less modified low salinity MEIW and hence overflow from the IFR crest.

Several temperature profiles in boxes 2 to 4 appear colder by nearly 2°C in the upper 400 m than the rest of the profiles. The colder profiles have been taken within cold core eddies that emanate from the Iceland-Faroe Front. The eddies have a cold surface expression, colder near bottom temperatures and layers of low salinities. The role these eddies play in the exchange of North Atlantic and Nordic Seas waters across the IFR will be investigated in a separate paper.

Mean and variability of the near bottom layer properties on the AIFR between 500 and 1000 m depth are presented in Figure 2.11. The figure shows the mean and standard deviation of the bottom mixed layer temperature (top), and height-above-bottom of the 4.5°C isotherm (bottom) plotted against distance from the FBC

sill. Bottom mixed layer temperatures on the AIFR are around 3°C, rising on the meridional portion of the AIFR (300 to 375 km), falling again in the WV (375 to 400 km). The HAB of the 4.5°C isotherm, a good representation of the overflow layer thickness, on average is between 75 and 100 m on the AIFR. The standard deviation of BML temperature is about 33% of the mean, and is about 50% for overflow thickness. These remain fairly constant on the AIFR outside the FBC.

2.5.3 Near-Bottom Velocities

The near bottom mean velocity field over the Atlantic Flank of the IFR is shown in Figure 2.12. Absolute geostrophic velocities were calculated from a mean density field averaged in 7.5×7.5 km wide by 10 m tall boxes. Shear was computed from horizontal density gradients and integrated to produce a vertical profile of relative velocities, the depth average of which was then matched to a statistically interpolated field from the Seaglider DAC observations. The absolute geostrophic velocities in Figure 2.12 are plotted 75 m above the bottom in an effort to both be within the overflow plume and avoid the frictional boundary layer in which geostrophic balance does not hold. Qualitatively the velocities confirm the canonical near-bottom circulation scheme on the AIFR, with along-isobath flow from the southeast to northwest becoming southwestward at the Iceland continental shelf (Hansen and Østerhus, 2000). This circulation reflects the parallelism of isopycnals and ridge topography seen in Figure 2.7. This field can be compared with the tracks of Prater and Rossby (2005), found from "bottom-following" RAFOS floats drifting approximately 100 m above seafloor. The three floats passed into the deep branch of the bifurcation, remaining with the majority of the FBC overflow generally deeper than 1000 m. Quantitatively the measured geostrophic velocities support the trajectories of the Prater and Rossby floats (gray markers in Fig. 2.12). Near-bottom geostrophic velocities average 18-30 cm s^{-1} with maxima of 60-70 cm s^{-1} near the Faroe Bank Channel outflow (below 600m isobath, mean: 21.5 cm s^{-1}, standard deviation: 11 cm s^{-1}). These estimates

agree well with the mean speeds of the RAFOS floats, typically 20-30 cm s^{-1} with peaks of 40-50 cm s^{-1} (Prater and Rossby, 2005). The maximum speeds in the FBC (60-70 cm s^{-1}) are lower than expected and are a consequence of the coarse 7.5×7.5 km grid, which is too large to capture horizontal density gradients in the narrow FBC. Both the geostrophic velocities and the float trajectories suggest the smoothness and continuity of the near-bottom flow. However, this mean flow is embedded in the well-documented strong eddy field of the region (Allen et al., 1994). The root-mean-square DAC over the entire IFR is 17.15 cm s^{-1}, with higher values on the ridge shallower than the 500 m isobath and in the FBC outflow. The standard deviation of the DAC is 11 cm s^{-1}. The variability in the DAC is smaller than the average near-bottom current speed, which helps to explain the direct trajectories of the Prater and Rossby (2005) RAFOS Floats.

To assess the importance of mesoscale velocity relative to the mean (along-slope) velocity, we compute the thermal wind shear due to sloping isopycnals observed between pairs of dives sorted into groups according to whether the glider was heading along or across the IFR slope. The slope of an isopycnal (S_{isp}) in the core of the stratified interface between the plume and the ambient Atlantic water is taken to be representative of interface tilt, and is assumed to represent the majority of the thermal wind shear. The calculations below use the slope of the 4.5°C isotherm to represent S_{isp}, an approximation valid in this region where density is dominated by temperature. The Margules relation may be derived from the thermal wind shear to give an expression for the strength of the baroclinic velocity in the plume:

$$\Delta U = \frac{g}{\rho_o f} \Delta\rho S_{\mathrm{isp}} \tag{2.3}$$

where $\Delta\rho$ and ΔU are the density and velocity difference across the plume interface. Inspection of cross-ridge sections like that in Figure 2.2, suggests that there is a strong background slope of the isopycnals that is nearly parallel to the topographic slope, and perturbed by mesoscale variability. To estimate the relative importance of the

background slope and the mesoscale perturbations of the slope to velocities in the overflow plume, pairs of dives on the AIFR are separated into two groups. The cross-ridge ('x-ridge') group, contains all dive pairs where the magnitude of the bottom slope (as measured by the acoustically-ranged bottom depth and dive separation) between the two dives is at least than 80% of the local topographic gradient calculated from ETOPO 1 minute bathymetry. On the AIFR, below 500 m between composite sections IV and XII, 800 dive pairs meet the criteria. The second group, referred to as along-ridge ('a-ridge'), consists of dive pairs where the bottom slope is less than 20% of the topographic gradient; 433 pairs met the criteria. The S_{isp} calculated from the x-ridge group should contain the background isopycnal slope suggested by Figure 2.2, as well as some mesoscale signal. The a-ridge group should only contain S_{isp} associated with mesoscale features, as there is no observable along-ridge mean isopycnal slope on the AIFR outside the FBC. Characterizing the isopycnal slope statistics of each group permits a description of the magnitude of eddy-like features relative to the larger scale topographically-induced component of the overflow circulation.

The distribution of isopycnal slopes in Figure 2.13**b** from the a-ridge group is nearly Gaussian and centered at zero, while the distribution of the x-ridge group is shifted to the right, centered at 5×10^{-3}. This supports the hypothesis that the along-ridge group samples the eddy-like mesoscale variability of the plume interface slope with zero mean. The x-ridge group contains the same mesoscale variability, along with the background isopycnal slope approximately parallel to the topography seen in Figure 2.2. The parallelism becomes apparent in Fig. 2.13**e** where the distributions of the ratio of isopycnal slope to local topographic slope show the x-ridge group centered on one, and the a-ridge group centered on zero. For each group, the density anomalies from an Iceland Basin mean density profile are shown in panel **a**. Calculating the magnitude of the velocity jump for each group from equation 2.3 leads to panel **c** in Fig. 2.13. The panel also contains the distribution of velocity jump calculated using the local topographic gradient in place of S_{isp} in eqn. 2.3. The mean velocity

magnitudes of the a-ridge, x-ridge, and topography groups are 13.6, 35.7, and 34.1 cm s^{-1} respectively, suggesting that the eddy component of baroclinic velocity is only half that due to the cross-IFR isopycnal tilt. The velocity due to cross-ridge isopycnal tilt is very close to that predicted by the topographic slope, implying that the topographic slope alone provides a good estimate of plume velocity magnitude.

Assuming that the a-ridge group provides information on eddy-like variability and that $S_{\mathrm{isp}} \approx S_{topo}$ for the x-slope case, any dive pair may be used to obtain the eddy component of baroclinic velocity by removing the slope due to topography, $S_{eddy} = S_{\mathrm{isp}} - S_{dive\_depth}$, and compare its implied velocity to the topographically-induced velocity at the dive location.

$$\frac{\Delta U_{\mathrm{eddy}}}{\Delta U_{\mathrm{topo}}} = \frac{S_{\mathrm{isp}} - S_{dive\_depth}}{S_{topo}} \tag{2.4}$$

In Fig. 2.13**f** the ratio of eddy velocity to topographic velocity is shown for the a-ridge (gray), x-ridge (thin black), and all dives on the AIFR (thick black). Removal of the bottom slope collapses the x-ridge velocity distribution onto the a-ridge distribution. The distribution of all dives show 80% of the eddy velocity jump magnitudes are smaller than 1, i.e., weaker than the topographically-induced baroclinic velocities. This analysis suggests that eddy-like mesoscale variability influences baroclinic velocity in the overflow plume, but its strength is only a fraction of the background state, which may be approximated by the topographic slope.

2.6 Western Valley

At the northwestern end of the IFR, where the ridge meets the Iceland shelf, a relatively deep depression cuts the ridge crest. Referred to as the Western Valley (WV), this region has been identified as a location of at least intermittent overflow across the IFR (Perkins et al., 1994, 1998; Wilkenskjeld and Quadfasel, 2005). The observations of bottom temperature upstream of the WV (in the sense of along isobaths in the direction of the FBC) are warmer than those in the WV against the Iceland shelf

(Fig. 2.9 and Fig. 2.14). A decrease in bottom temperature along a given isobath in the WV provides evidence that overflow is entering the region from the direction of the IFR crest. This hypothesis is supported by the properties of the overflow found in the WV, which is relatively cold and fresh, suggesting that it is close to its source and has not had a significant amount of time to mix with the overlying Atlantic Water (e.g. Fig. 2.10, box 4, located in the WV).

Additional support for western IFR origins of WV overflow comes from analysis of a simple overflow model. The model, developed in Killworth (2001), assumes a quadratic turbulent bottom drag and local equilibrium turbulence solution. Overflows in the model follow a simple trajectory where their rate of descent is constant assuming that turbulence in the bottom boundary layer remains high. To identify the possible origins of the overflow water each point along composite Section XIII was taken as an end-point of the Killworth model, which was then run backwards using a range of descent rates to estimate the starting location of each point.Figure 2.15 shows the results using a descent rate of 1 m in 600 m of horizontal travel. The trajectories of points along Section XIII trace out a 'watershed' of overflow found in the WV, i.e., the region of the IFR crest from which overflow would drain into the WV. Different descent rate parameters give qualitatively similar solutions, namely overflow found in the Western Valley crossed the IFR through the WV proper or on the northwestern half of the IFR. Steeper descent rates (1/400, 1/200) restrict the WV overflow source farther to the northwest.

Where the IFR abuts the Icelandic plateau, the Iceland shelf becomes the dominant topographic feature. Overflow isopycnals lean against the Iceland slope as the flow changes direction towards the southwest, flowing away from the IFR towards the Reykjanes Ridge. Current meter records in the region indicate long term near bottom velocities are steady and directed along the Iceland shelf with mean speeds of 50 cm s^{-1} (Perkins et al., 1998). It is unclear from the Perkins et al. (1998) study if the steady near-bottom velocities imply a steady overflow transport as contempora-

neous temperature records are not published with the current meter data. Multiple Seaglider transects in the region indicate the overflow transport in the WV is more variable than the current meter records of Perkins et al. (1998) suggest.

The Seagliders in this study made 28 transects across the WV between 2006 and 2009. An attempt was made in each transect to approach Iceland shelf normal to the isobaths so that cross sectional transport estimates of along slope flow could be made using geostrophy. Shelf break currents and eddies distorted the sections somewhat but rough estimates of along-slope overflow transport can be made. Very often a narrow current of dense water, between 8 and 14 km wide, was found leaning against the Iceland shelf, the density and thickness of which varied considerably. Figure 2.16 presents four example density sections, two of which have large overflow transport, and two exhibit very little overflow. The figure contours all density anomalies greater than 27.65 kg m^{-3}, but we again use the $\sigma_\Theta \geq$27.8 kg m^{-3} criterion to define the overflow transport of the Iceland shelf-break overflow current. Between 26 June and 7 July 2009, a single Seaglider made four sections normal to the Iceland shelf break (not pictured). The Seaglider found a shelf break overflow current with transports of 0.44 Sv (27-28 June), 0.68 Sv (28-30 June), 1.17 Sv (30 June- 1 July) and 0.07 Sv (6-7 July). Though not exactly co-located (three of the four are within 10 km of each other, the fourth, the 28-30 June section, was within 25 km), these sections were close to one another and demonstrate significant variability of the overflow in the Western Valley in a period of days or weeks. The mean (standard deviation) overflow transport from the 28 transects is 0.43 Sv (0.48 Sv), (Fig. 2.8) , with a minimum of 0.05 Sv and a maximum of 2.13 Sv. These values are likely an underestimate of the total IFR overflow considering that the overflow across the eastern IFR has most likely descended below 1000m by the time it reaches the Iceland shelf.

Käse et al. (2013) found a seasonal cycle in WV overflow transport in both observations from an ADCP as well as two numerical models. They find maximum overflow transport in summer with considerable variability on timescales of days to

weeks. Of the 28 Seaglider sections, two were made in February, 10 in June, and 16 in September. Although this distribution cannot establish a seasonal cycle, nonetheless the mean transport values in June (0.69 SV) and September (0.29 Sv) are larger than the mean of the two observations in February (0.2 Sv).

The steady overflow current measurements in the WV led Perkins et al. (1998) to postulate that numerous overflow sources and long transit times insulate the narrow Iceland shelf break overflow current from the variability of the IFR overflow events. The present observations suggest considerably more variability in the transport of this current. The 'watershed' of overflow in the WV appears to be only the northwestern portion of the IFR, restricting the number of overflow locations and therefore the possibility that long transit times and multiple sources can buffer the Iceland shelf break current against variability in its sources.

2.7 Conclusions

We have presented analysis of three years of new hydrographic data in the region of the eastern Greenland-Scotland Ridge. Mean hydrographic properties support existing knowledge about the Faroe Bank Channel overflow while the large quantity and high spatial resolution of the observations allows for a more detailed description of the region, in particular the distribution of the overflow downstream of the FBC. New estimates of an Iceland-Faroe Ridge overflow in the Western Valley have been presented.

We find geostrophically balanced flow at Section I in the FBC with a long-term mean transport of 1.8±0.2 Sv of dense water ($\sigma_\Theta \geq 27.8$ kg m^{-3}), consistent with measurements at the channel sill (Hansen and Østerhus, 2007). The FBC overflow remains thick ($\geq$200 m) until a secondary sill is crossed approximately 50 km downstream of the main sill, at which point the plume thins ($\sim$115 m) as it evolves from a channel flow to a gravity current on a slope. This secondary sill coincides with the largest changes in the properties of the overflow plume. Between the second sill and

a topographic feature near 10°W, composite sections suggest that the plume is not is geostrophic balance. This region is one where elevated mixing, critical Froude numbers, and hydraulic criticality have been observed in past studies (Fer et al., 2010; Girton et al., 2006; Pratt et al., 2007). Between the secondary sill and the topographic feature the overflow bifurcates with densest portion of the plume, and 67% of the total transport, descending below 1000 m. A shallower branch of approximately 0.6 Sv remains at intermediate depths on the IFR. Seaglider inferred dissipation is also highest in this region (Beaird et al., 2012). We conclude that the region at and just downstream of the second sill of the FBC marks a more important dynamical transition than the primary FBC sill.

On the Atlantic flank of the Iceland-Faroe Ridge the along-slope overflow transport remains fairly constant at 0.6 Sv for 150 km. Absolute geostrophic velocities above the frictional BBL average 21.5 cm s^{-1}, predominantly along bathymetric contours. Rough calculations suggest the observed mean along slope flow must be maintained by approximately 0.8 Sv of overflow from the IFR.

Bottom mixed layers range in thickness from 0 to 70 m with temperatures between 1 and 5°C. Individual profiles show that a near bottom pycnocline, evidence of overflow, is ubiquitous on the AIFR. This pycnocline is nearly parallel to the slope of the ridge bathymetry, supporting the along-slope mean circulation. Pycnocline slopes associated with mesoscale variability are a fraction of the cross-ridge slopes, suggesting that the baroclinic velocities of the mesoscale features play a second order role in the circulation of the overflow plume on the Atlantic flank of the IFR.

Around 13°W the IFR becomes meridionally-aligned and along-slope transport through the sections diminishes to about 0.2 Sv. This portion of the IFR is characterized by relatively warm near-bottom temperatures (mean: 3 - 5°C, minimum: 2 - 3°C) that isolate the colder, less diluted, overflows on the eastern half of the ridge from the cold overflow waters found in the Western Valley at the Iceland shelf break.

We frequently find relatively undiluted overflow water adjacent to the Iceland

shelf in the WV, waters that evidently crossed the IFR, if not through the WV itself, somewhere on the northwestern portion of the IFR. Repeated Seaglider sections normal to the Iceland shelf show that the standard deviation in the overflow transport (0.48 Sv) is as large as the mean (0.43 Sv) in the current adjacent to the Iceland Shelf. It appears that significant variability in the overflow transport in the WV exists on timescales of days to weeks.

2.8 Figures

Table 2.1: Geographic abbreviations frequently used in text.

Acronym	Name
FBC	Faroe Bank Channel
IFR	Iceland-Faroe Ridge
AIFR	Atlantic Flank of Iceland-Faroe Ridge
WV	Western Valley

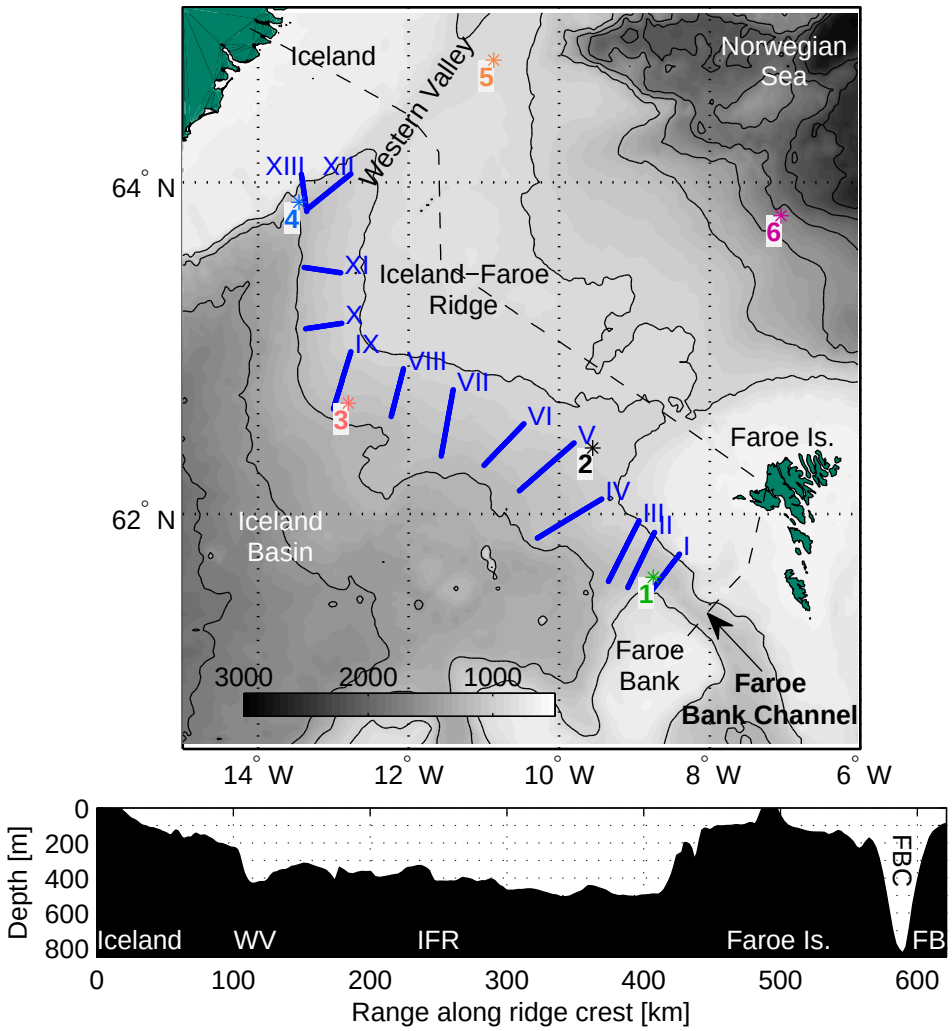

Figure 2.1: Top: Bathymetry and location of features in the area of study. Blue lines indicate the locations of synthetic sections discussed later in the text. Colored numbered squares mark the locations of the profiles in Figure 2.3. Bold contours are plotted at 500 m intervals beginning with the 500 m isobath and continuing deeper. Bottom: A profile of ridge crest depth along the dashed line in the top panel. Abbreviations in the ridge profile are as follows: WV (Western Valley), IFR (Iceland-Faroe Ridge), FBC (Faroe Bank Channel), FB (Faroe Bank).

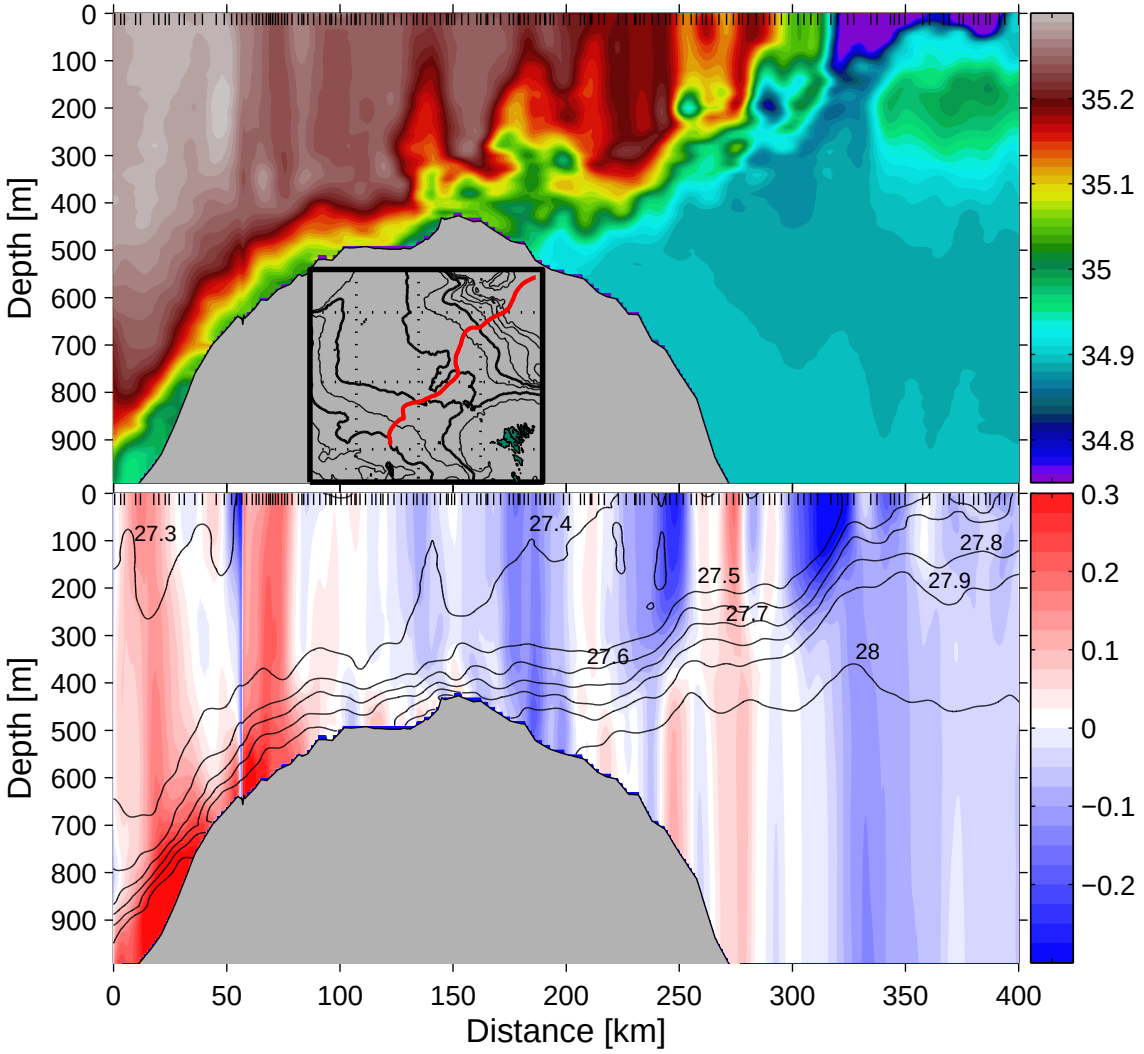

Figure 2.2: Top: Salinity contours on a section normal to the IFR occupied by a Seaglider, 3-23 December 2007. Dive and climb positions are shown as black vertical tick marks at the top of the figure. Location of the track is shown in the inset map. Bottom: Absolute geostrophic velocity (cross-section component, color contours [m s^{-1}]) and potential density (black contours [kg m^{-3}]). Positive velocities are towards the northwest.

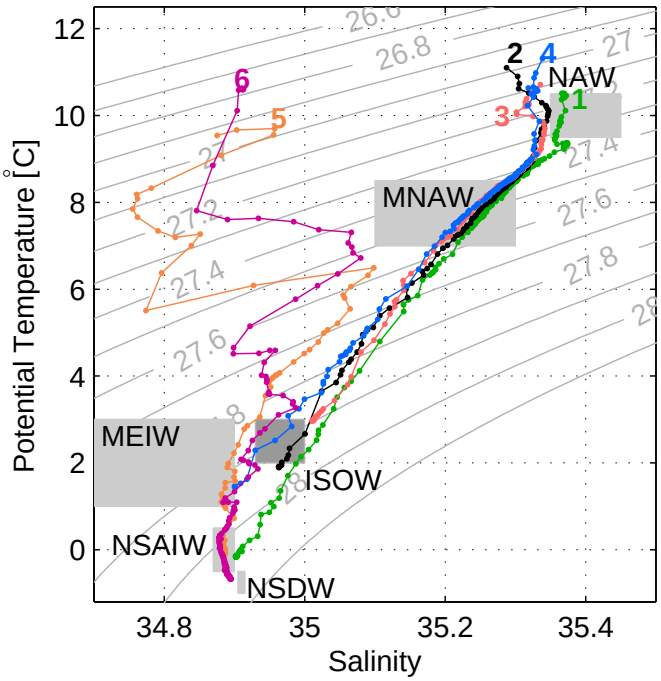

Figure 2.3: Potential temperature vs salinity for six profiles at the location of the numbered colored squares in Figure 2.1. Watermass definitions for North Atlantic Water (NAW), Modified North Atlantic Water (MNAW), Modified East Icelandic Water (MEIW), Norwegian Sea Arctic Intermediate Water (NSAIW), Norwegian Sea Deep Water (NSDW), and the Iceland Scotland Overflow Water (ISOW) product are shown as gray boxes covering the property ranges of each type. Potential density is contoured in gray.

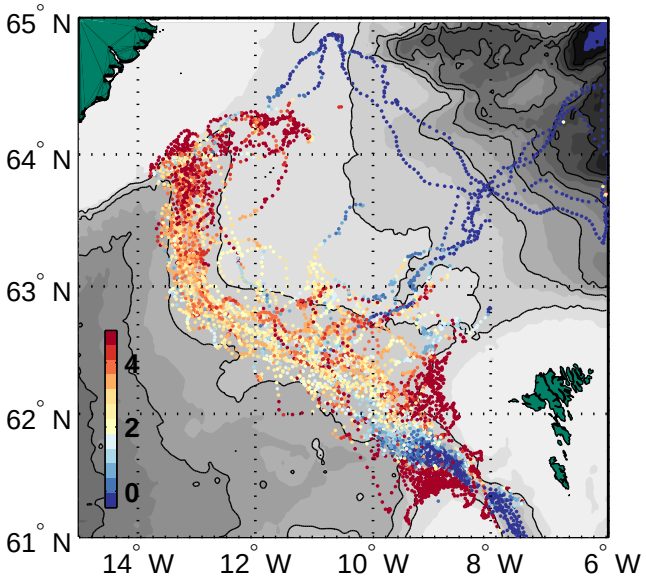

Figure 2.4: Bottom temperatures [°C] on the Iceland-Faroe Ridge from all Seaglider dives between November 2006 and November 2009. Shaded bathymetric contours are plotted every 250 m, with bold contours every 500 m below 500 m.

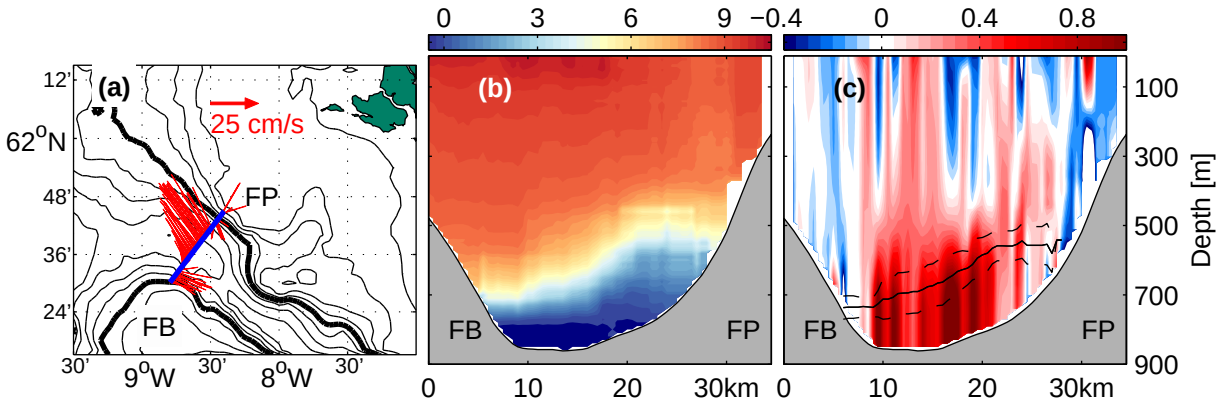

Figure 2.5: (a) Location of Section I in the FBC and averaged DAC vectors (red) used to reference geostrophic velocity calculations. Depth contours at 100 m intervals with 500 m contour in bold. Depth [m] by cross-channel distance [km] sections of (b) potential temperature [°C] and (c) absolute geostrophic velocity [$\mathrm{m\,s^{-1}}$, positive to the northwest]. The mean depth of the 3°C isotherm observed in individual dives is plotted in black with dashed lines indicating ± one standard deviation. 'FP' refers to the Faroe Plateau side of the channel and 'FB' is the Faroe Bank side.

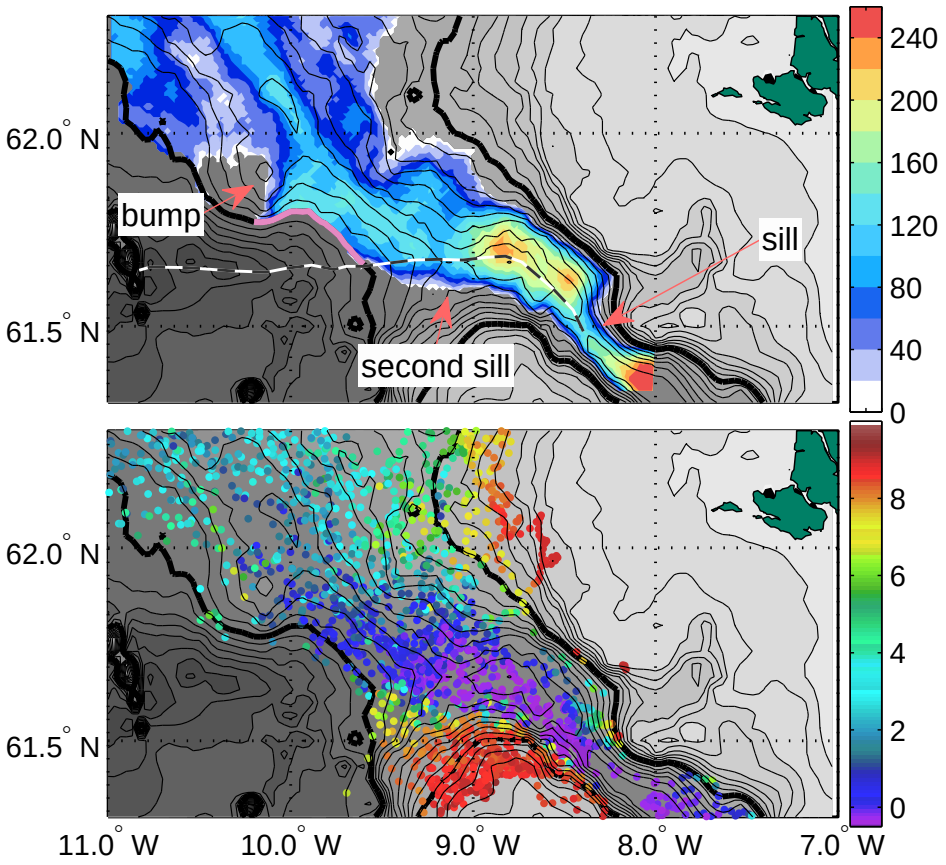

Figure 2.6: Top: Thickness [m] of the ISOW layer near the Faroe Bank Channel exit based on a fine-grid objective map of all Seaglider data. Plume thickness is defined as the vertical distance between the mapped $\sigma_\theta = 27.8$ isopycnal surface and the seafloor. Bathymetric contour interval is 50 m, with 1000 m and 500 m isobaths in bold. The thalweg (deepest point) is indicated by a back-and-white dashed line. The portion of the 1000 m isobath where the downslope plume edge is deeper than the reach of the Seaglider is highlighted in pink, indicating the area through which the deeper branch of the plume flows. The primary and terminal (second) sills of the FBC are labeled, along with the topographic 'bump' which marks the end of the plume bifurcation region. Bottom: Near bottom temperatures [°C] from individual Seaglider dives in the FBC outflow region.

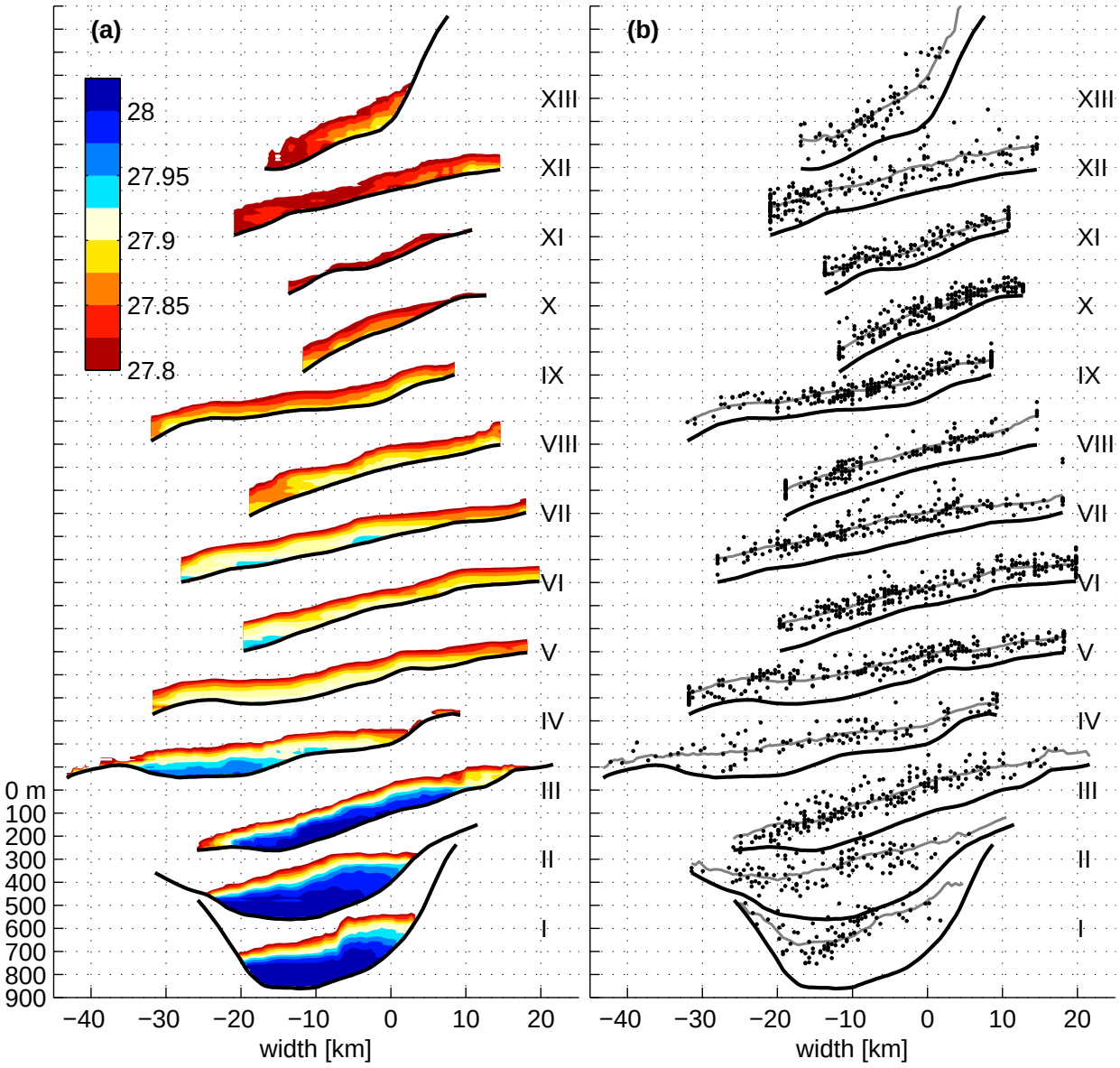

Figure 2.7: Mean overflow potential density contours, (a), and observations of the depth of the 4.5°C isotherm, (b), for each of the 13 composite sections shown in Figure 2.1. Sections are offset 300 m in depth for clarity, with vertical tick marks placed every 100 m. Labeled depths refer to Section I. Roman numeral section numbers are centered on 600 m in the reference frame of each section. Dark lines indicate bathymetry along each section. Width is measured with respect to the location of the 700 m isobath. In (b) black dots show observations of the depth of the 4.5°C isotherm while the thin gray line shows the mean depth.

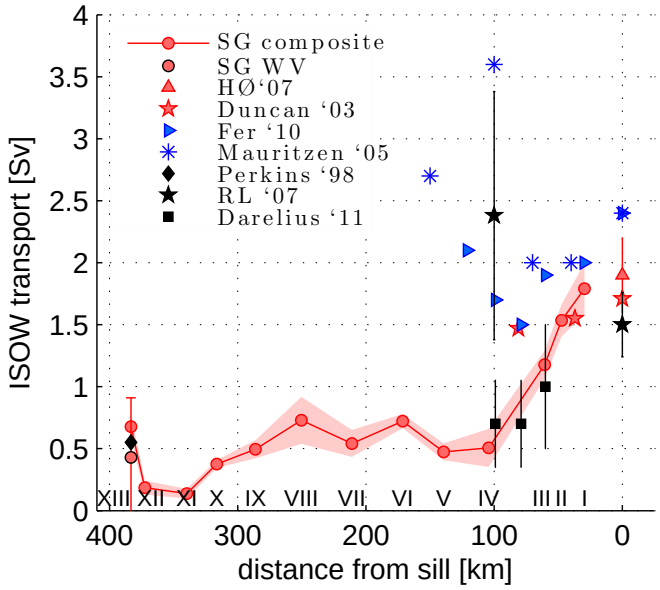

Figure 2.8: Cross-sectional transport through composite Sections I-XIII ('SG composite') vs. distance from FBC sill. Standard deviations from the Monte Carlo approach are shown by the pink patch. The average transport through individual Seaglider sections in the Western Valley is shown as well ('SG WV'). Included are transport estimates from various authors: Blue symbols indicate estimates using the $\sigma_\theta \geq$27.65 criterion, whereas red symbols use $\sigma_\theta \geq$27.8. Black markers indicate other plume definitions used by various authors (model tracers (RL '07: Riemenschneider and Legg, 2007), depth-of-no-motion (Perkins et al., 1998), and waters colder than 3°C in Darelius et al. (2011)).

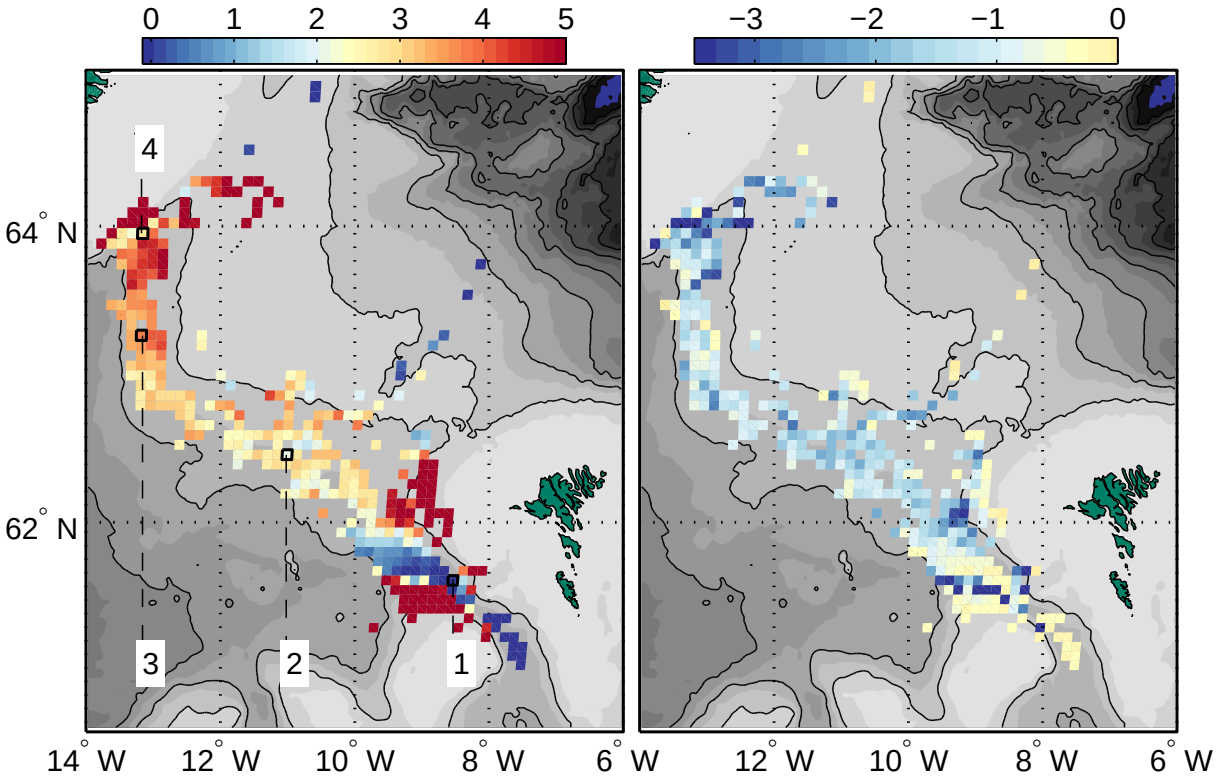

Figure 2.9: Left panel: mean bottom potential temperature [°C] in 7.5 × 7.5 km boxes. Right panel: minimum bottom potential temperature anomaly from the mean in the same boxes [°C]. Numbered and outlined boxes in the left panel correspond to the profiles in Fig. 2.10.

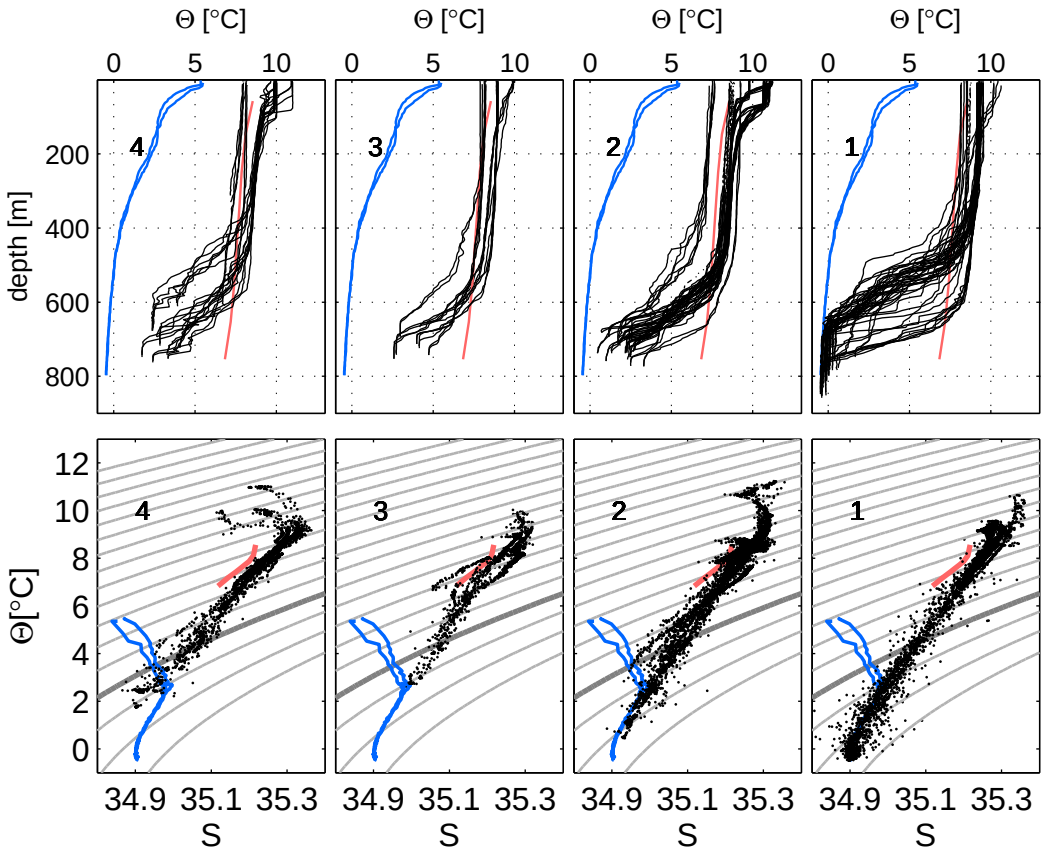

Figure 2.10: All potential temperature profiles (top row), and all Θ-S curves (bottom row) contained in the four boxes outlined in black in Figure 2.9. The FBC box is on the right (box 1), moving to downstream boxes toward the left. The bold contour on Θ-S plots is the 27.8 isopycnal, and at 0.1 kg m^{-3} intervals. Blue profiles show 'upstream' conditions in the Nordic Seas and red profiles show 'ambient' conditions in the Iceland Basin.

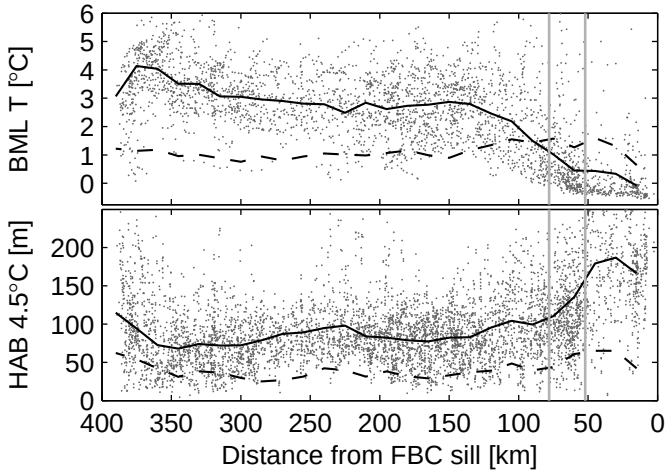

Figure 2.11: Bottom layer property means (solid line) and standard deviations (dashed line) on the IFR between the 500 and 1000 m isobaths in 15 km bins of distance from the primary FBC sill. Individual observations are plotted in light gray. Top: bottom mixed layer temperature. Bottom: height-above-bottom of the 4.5°C isotherm. The vertical grey lines around 50 and 80 km indicate, respectively, the location of the secondary FBC sill, and the point at which the FBC overflow first intersects the 1000 m isobath.

Table 2.2: Regional water mass property ranges (Fogelqvist et al., 2003; Hansen and Østerhus, 2000)

Acronym	Name	Temperature range	Salinity range
NSDW	Norwegian Sea Deep Water	-1.03°C	34.91
NSAIW	Norwegian Sea Arctic Intermediate Water	$-0.5 \rightarrow 0.5$°C	$34.87 \rightarrow 34.9$
MEIW	Modified East Icelandic Water	$1 \rightarrow 3$°C	$34.6 \rightarrow 34.9$
MNAW	Modified North Atlantic Water	$7 \rightarrow 8.5$°C	$35.1 \rightarrow 35.3$
NAW	North Atlantic Water	$9.5 \rightarrow 10.5$°C	$35.35 \rightarrow 35.45$
DSOW	Denmark Strait Overflow Water	$0.7 \rightarrow 1.9$°C	$34.84 \rightarrow 34.87$
ISOW	Iceland-Scotland Overflow Water	$2.7 \rightarrow 2.9$°C	34.92

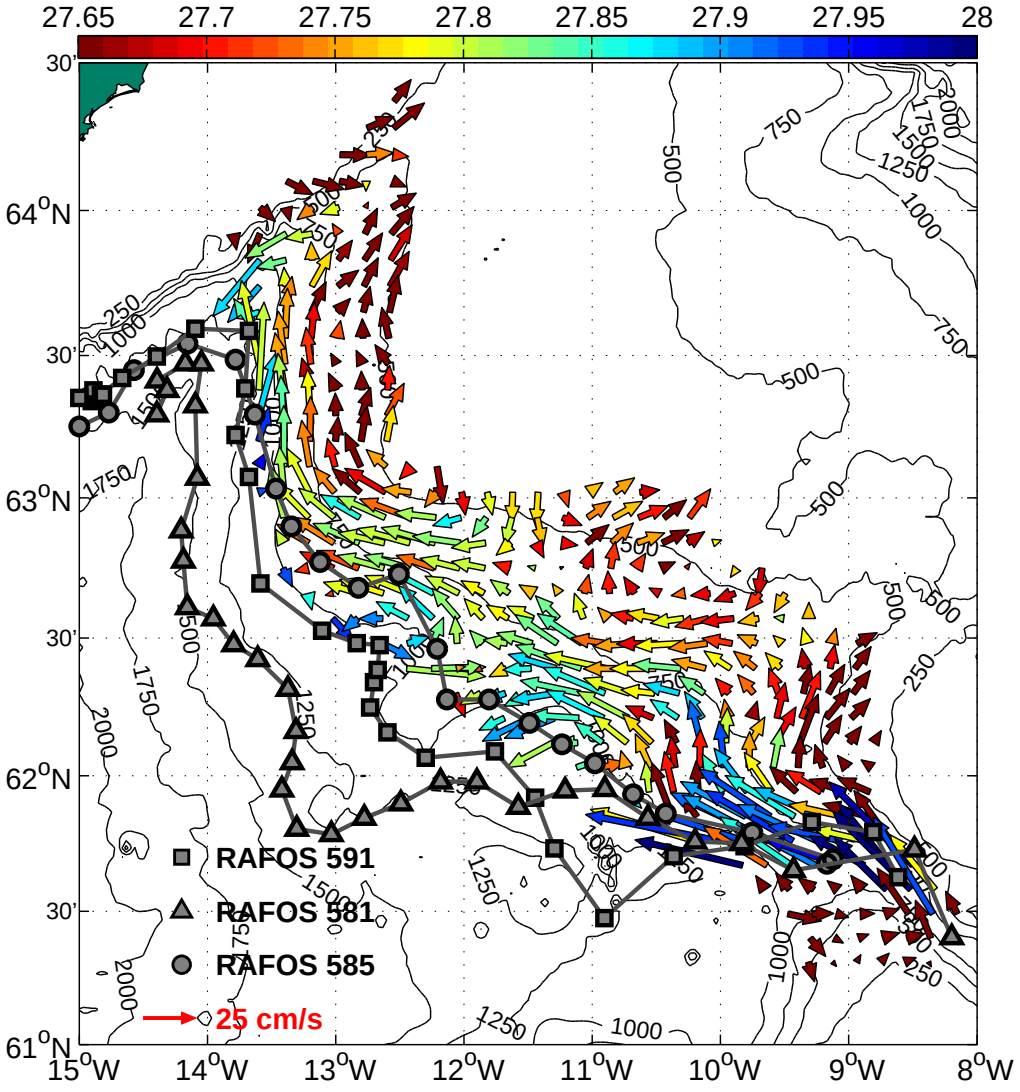

Figure 2.12: Near bottom absolute geostrophic velocities (75 m above bottom) and RAFOS float trajectories (Prater and Rossby, 2005). Vector color indicates potential density at 75 m above the bottom.

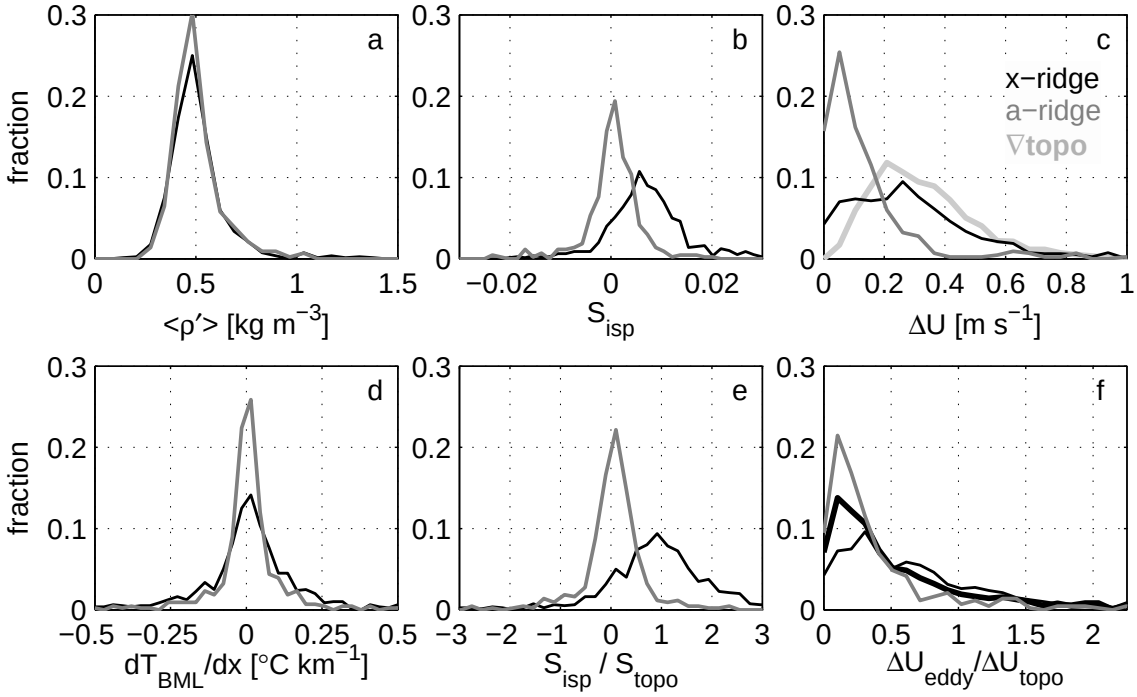

Figure 2.13: Distributions of variables related to eddy and mean baroclinic velocities on the AIFR. In panels **a** through **e**, dark black represents the cross-ridge group, medium grey represents the along-ridge, and in **c** light grey represents velocities based on topographic slopes. **a**: distribution of vertically averaged plume density anomaly from ambient Iceland Basin density. **b**: Isopycnal slopes between dive pairs. **c**: Magnitude of the velocity jump across the plume interface due to the isopycnal slope and density anomaly as in equation 2.3, the light grey shows the velocity jump if $S_{\rm isp}$ is replaced by the local topographic gradient. **d**: Distribution of the along-section bottom mixed layer temperature gradient between sequential dives. **e**: Distribution of the ratio of isopycnal slope to topographic slope. **f**: Distribution of the ratio of velocity jumps due to eddy isopycnal slopes to that due to topographic slope for the x-ridge (thin black), a-ridge (gray) and all dives (thick black).

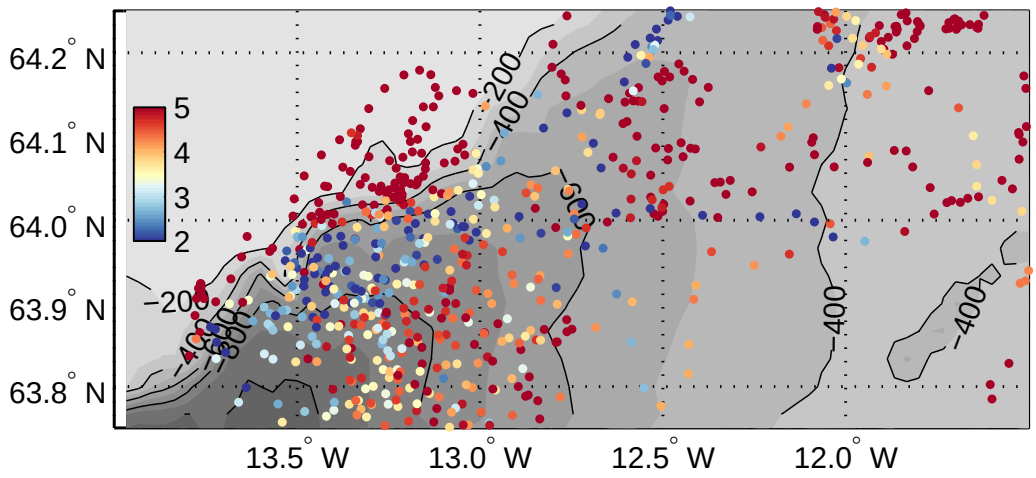

Figure 2.14: Bottom temperatures from individual dives in the Western Valley showing anomalous cold waters along the Iceland shelf.

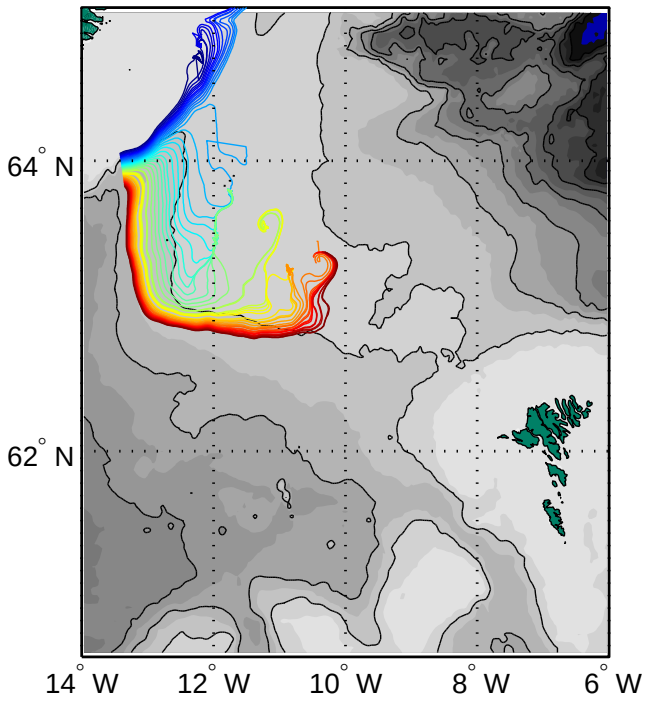

Figure 2.15: Trajectories of particles arriving at Section XIII (Fig. 2.1) computed using the constant descent rate (1/600) model of Killworth (2001) . The model is run backwards for 300 km from the blue points along Section XIII. Color is proportional to the distance of the arriving trajectory along Section XIII.

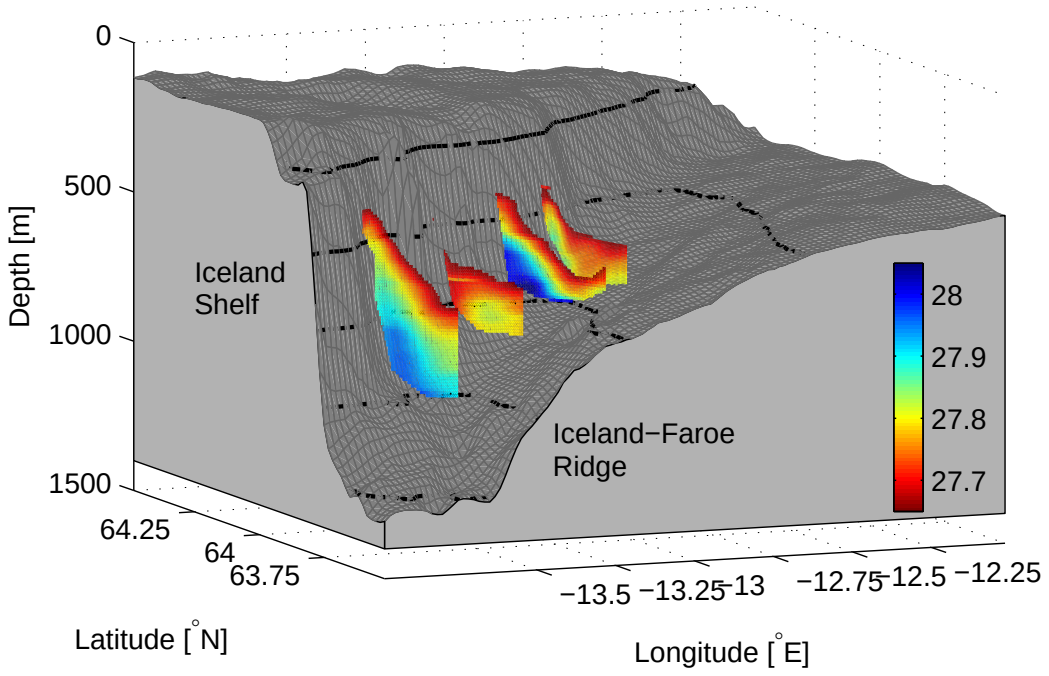

Figure 2.16: Four representative Seaglider sections intersecting the Iceland shelf from September 2007 and June 2007, 2008, 2009. Contours of σ_Θ are shown in color for only the portion of the sections with density greater than 27.65 kg m^{-3}. Two of the sections encounter large overflow events and two see little overflow.

Chapter 3

DISSIPATION OF TURBULENT KINETIC ENERGY INFERRED FROM SEAGLIDERS: AN APPLICATION TO THE EASTERN NORDIC SEAS OVERFLOWS

3.1 Introduction

The Faroe Bank Channel (FBC) and its smaller neighboring overflow across the Iceland-Faroe Ridge (IFR) account for one-third of total Nordic Seas outflow into the North Atlantic (Hansen and Østerhus, 2000). Considerable effort has been focused on the region in general, and on the FBC in particular. Along with entrained Atlantic waters, which double the initial overflow volume transport, these overflows make up a large part of the North Atlantic Deep Water (NADW). NADW has global extent in the deep ocean and its circulation forms the lower limb of the Atlantic Meridional Overturning Circulation. The location and intensity of turbulent mixing and entrainment in these overflows has an important impact on the ventilation of the deep ocean and the oceanic meridional heat transport. Entrainment of overlaying waters is particularly interesting in this region where wintertime mixed layers can sometimes reach the depth of the overflow plume interface.

A comprehensive review of North Atlantic-Nordic Seas exchanges is given by Hansen and Østerhus (2000) and of the FBC overflow by Hansen and Østerhus (2007). At the sill thresholds, approximately 3 Sv of Nordic origin waters form energetic bottom-intensified gravity currents flowing into the Iceland Basin. Of the total 3 Sv, 1.9 Sv exits through the FBC, and the remainder crosses the IFR. The Faroe Bank Channel overflow is swift ($O(1\text{ m s}^{-1})$) and unidirectional, with a bottom mixed layer

of cold (≈0°C) water capped by a thick (O(100 m)) interfacial layer below the ambient Atlantic waters. Dissipation levels as high as 10^{-5} W kg^{-1} illustrate the energetic turbulence at work in the overflow (Fer et al., 2010). The FBC overflow exhibits considerable mesoscale variability which plays a role in the mixing and descent of the plume (Darelius et al., 2011; Seim and Fer, 2011). After exiting the FBC, the overflow plume makes an inertial turn to the right and flows along isobaths on the Atlantic flank of the IFR, driven by a balance of pressure gradient, Coriolis and frictional forces. As it flows downstream, the plume descends slightly due to the frictional relaxation of the geostrophic constraint. The FBC plume is joined along this path by overflow from the IFR, which is more spatially intermittent but has very similar source waters.

By the time these waters have traveled downstream to form Northeast Atlantic Deep Water (NEADW) their volume flux will have doubled to 6 Sv and their temperature and salinity properties will be significantly diluted by entrainment of overlying Atlantic waters. These overflows occur in physically small regions (the FBC sill is ≈ 10 km wide), exhibit complex sub-mesoscale flow features, and depend intimately on very small scale mixing processes. Despite the small scales of the overflows, their influence is felt on basin, planetary and climatic scales. It is critical, but notoriously difficult, to represent overflows in numerical models (Legg et al., 2009). The intensity of mixing and entrainment in the overflow plumes affects their eventual volume flux, descent rate, end-member properties and detrainment depth. In addition to the obvious effect on plume properties, recent studies of the Mediterranean Outflow also suggest that the upper ocean responds directly to the potential vorticity forcing from the descent and entrainment of overflows (Kida et al., 2008).

Several indirect mixing estimates (mainly based on heat budgets) have been made in the FBC (Saunders, 1990; Duncan et al., 2003; Mauritzen et al., 2005), while more recently the first direct microstructure turbulence measurements have been made by Fer et al. (2010), all of which indicate intense mixing in the FBC plume downstream

of the sill. These studies are important to facilitate understanding of mixing in the overflows, however, in each case the shipboard surveys only lasted a short time. The well-documented variability of the FBC overflow (Geyer et al., 2006; Darelius et al., 2011) and the myriad locations of IFR overflow suggest more complete time series and higher spatial resolution of mixing estimates are desirable.

In this paper a three year dataset of Seaglider observations in the FBC and on the IFR is used to obtain a more complete spatial picture of the mixing and entrainment in these overflows. These data extend 300 km further downstream than the majority of the FBC overflow studies mentioned above, and offer the first look at turbulence in the IFR overflows. The analysis presented here hinges on the development of a method to obtain estimates of dissipation of turbulent kinetic energy, ε, from the Seaglider. The method is developed and then validated by comparison between a Seaglider deployment and a contemporaneous microstructure survey (Fer et al., 2010).

3.2 Measurements

The data presented in this study come from two sources: one shipboard and one Seaglider survey. Ancillary data include approximately 2-month long measurements from a moored instrument located at the center of the shipboard and Seaglider surveys. The glider data were collected over three years, between November 2006 and November 2009. Deployments were made every three months, with 23 successful missions producing roughly 17,400 profiles of temperature, salinity, dissolved oxygen, fluorescence, optical backscatter and vertical velocity in the Iceland-Faroes region.

The Seaglider is a small, autonomous, buoyancy-driven vehicle which profiles to a maximum depth of 1000 m in a sawtooth pattern (Eriksen et al., 2001). The gliders deployed in this survey were equipped with unpumped custom Sea-Bird Electronics conductivity (SBE 4) and temperature (SBE 3) sensors, a Wetlabs BB2FVMG optical puck with florescence and two wavelengths of backscatter, and a Sea-Bird Electronics oxygen sensor (SBE 43). During the Faroes mission, the gliders sampled water column

properties at 20 s intervals. With typical vehicle descent/ascent rates of 6-10 cm s^{-1}, the vertical resolution of the profiles was approximately 1.2-2 m. The vertical to horizontal glide ratio of 1:3 gives horizontal resolution of 3.6-6 m between consecutive samples, while dive and climb profile separations vary with depth due to the slant-vertical path of the instrument. Adjacent glider surfacings are typically 3 to 6 km apart. An acoustic altimeter mounted forward on the Seaglider is used to detect and avoid the seafloor. In order to fully sample the overflow plume, these gliders were programed to begin their dive-to-climb transition 10 m above the acoustically ranged bottom.

The distribution of the Seaglider data in the FBC and downstream on the IFR is shown in Figure 3.1. Each point in the figure represents one dive/climb profile pair and color indicates the bottom temperature, or the temperature at the deepest observation made by the instrument. Typically Seagliders were deployed in the FBC where they remained for several days as the pilot trimmed flight control parameters. Trimmed vehicles were subsequently flown northwestwards along isobaths of the IFR. After reaching the Iceland shelf break the gliders were piloted back to the FBC or, on occasion, across the IFR into the Norwegian Basin.

The shipboard survey was made from the R.V. Håkon Mosby during the period 29 May - 8 June 2008 (Fer et al., 2010). During the cruise, 90 profiles were collected using a vertical microstructure profiler (VMP2000, Rockland Scientific Instruments, VMP hereafter). The VMP had a depth rating of 2000 m and was equipped with pumped SBE-CTD (conductivity, temperature, depth) sensors, a pair of airfoil shear probes used for measuring the dissipation rate of turbulent kinetic energy (ε), and fast response temperature and conductivity sensors. The turbulence and slow sensors sampled at 512 Hz and 64 Hz, respectively, at a nominal profiling speed of 0.6 m s^{-1}. Stations were taken on six cross-sections along the path of the overflow plume starting from the sill crest to about 120 km downstream of the sill, a downstream section, as well as two repeat stations of approximately 12 h duration (Fig. 3.2). The downcast

of the VMP typically reached 10 - 50 m height above bottom (HAB). The profiles of ε were obtained from the shear probes of the VMP as 1 m vertical averages, by integrating the vertical wavenumber spectrum of shear and assuming isotropy. The lowest detection level (noise level) in ε measurements based on shear probe data in the quiescent portions of the water column was 10^{-10} W kg^{-1}. Details on the sampling and data processing can be found in Fer et al. (2010) and Seim and Fer (2011).

Additionally, we make use of vertical velocity and temperature measurements acquired by temperature loggers and a downward looking acoustic Doppler current profiler (ADCP, RDI 300 kHz Workhorse Sentinel) moored at 61° N 41′, 9° W 11′ at the 804 m isobath, between 14 May and 18 July 2008. The mooring is located about 60 km downstream of the FBC sill, referred to as B2 in Darelius et al. (2011) and CM in Seim and Fer (2011). We refer to the mooring as B2, consistent with Darelius et al. (2011). The ADCP installed in a spherical buoy at 200 m HAB ensemble averaged 50 profiles every 5 min with 2 m vertical depth bins, returning high quality data with negligible tilt from vertical (1.6 ± 0.7 ° roll and -1.4 ± 0.7 ° pitch). Temperature time series were recorded by a number of temperature (SBE39 and RBR TR-1050) and CTD (SBE37 MicroCAT) sensors mounted on the mooring at 20, 101, 148, 140-200 (10 m intervals), 201 and 210 m HAB. Vertical displacements of the instruments due to horizontal currents were calculated following Dewey (1999), and temperature records were linearly interpolated onto a vertical grid using the inferred instrument depths (Darelius et al., 2011). The time series of the HAB of the 3°C isotherm is used to highlight the low-frequency variability associated with the FBC overflow. A more complete description of the moored instruments, data processing and discussion on mesoscale variability and plume dynamics can be found in Darelius et al. (2011) and Seim and Fer (2011).

A comparison will be made between the dissipation measurements from the VMP and the estimates from a concurrent Seaglider deployment. Seagliders are designated by the letters ‘sg’ followed by a serial number. Around the time of the VMP survey

in June 2008, Seaglider 5 (sg005) was deployed in the Faroe Bank Channel. The data from sg005 will be compared with the VMP survey to determine calibration coefficients for the Seaglider ε estimate.

3.3 Methods

3.3.1 Vertical Velocities from Seaglider

The Seaglider can furnish an estimate of vertical water velocity, w, by taking advantage of an accurate vehicle flight model and its on-board pressure sensor. The validity of the flight model assumptions is critical, but in principal the w estimate is straightforward: The vehicle vertical speed through a quiescent ocean, w_{model}, is calculated by a flight model using the measured pitch and buoyancy, while the absolute vertical speed is calculated from the time rate of change of pressure on-board the glider, w_{meas}. Removing the relative vehicle speed from the absolute gives the ambient water vertical velocity: $w = w_{\text{meas}} - w_{\text{model}}$. Detailed descriptions of the flight model and the process of determining w may be found in Frajka-Williams et al. (2011) and Eriksen et al. (2001). We will reproduce the basics of the calculation here.

Assuming steady flight, the force balance on the Seaglider is between the lift (L) from the wings, the drag (D) on the body and the glider's excess buoyancy (B):

$$L = \wp h^2 a\alpha = -B\cos\theta \tag{3.1}$$

$$D = \wp h^2 (bq^{-(1/4)} + c\alpha^2) = B\sin\theta \tag{3.2}$$

$$B = g(-M + \rho V(t,p,T)) \tag{3.3}$$

where h is the hull length, α the attack angle, θ the glide-slope angle, a, b, c are the lift, drag and induced drag coefficients respectively, g is gravitational acceleration, M is the vehicle mass, $V(t,p,T)$ is the total vehicle volume as a function of time (t, a result of controlled pumps/bleeds of hydraulic oil between reservoirs interior

and exterior to the pressure hull), pressure (p), and temperature (T), and $\wp$ is the dynamic pressure. The glide-slope angle (θ) is the angle between the horizontal and the trajectory of flight, while the attack angle (α) is the angle between the chord line of the glider wings and the direction of the incident fluid. The distinction is critical because the glider can only measure its pitch angle (ϕ) from the inclinometer, but lift and drag are functions of the attack angle, while the glide-slope angle describes the ratio of vertical to horizontal motion through the water. The glide-slope and attack angles are related to the measured pitch angle by $\phi = \alpha + \theta$. The dynamic pressure term contains the velocity information, $\wp = \rho(U^2 + W^2)/2$, where U and W are the horizontal and vertical glider speeds and ρ is the water density. The functional forms of lift and drag in equations 3.1 and 3.2 are based on hydrodynamic testing of the vehicle shape (Hubbard, 1980). The flight model is sensitive to the values of the flight parameters $a, b,$ and c and the total vehicle volume $V(t, p, T)$, all of which must be independently determined for each Seaglider. The flight equations 3.1 and 3.2 are solved iteratively for $\wp$ and α. Finally, the modeled vertical vehicle speed is calculated from the dynamic pressure and glide angle as

$$w_{\mathrm{stdy}} = \sqrt{\frac{2\wp}{\rho}}\sin\theta. \tag{3.4}$$

Figure 3.3 provides examples of the resulting vertical velocity profiles from two Seaglider dives. The profile from a dive in the FBC that passes through the energetic overflow plume (Fig. 3.3, left) is significantly more energetic than the profile in the deep quiescent region north of the IFR in the Norwegian Sea (Fig. 3.3, right). Additionally, it is relevant to the dissipation estimate method outlined below to note that the vertical velocity variance at high vertical wavenumbers increases in the FBC overflow plume (Fig. 3.3, left, depth $\gtrsim$ 700 m).

Recent analysis of Seaglider deployments in the Labrador Sea shows sensible w fields in stratified and deeply convecting regions. The Labrador Sea Seaglider w observations of Frajka-Williams et al. (2011) indicate that the root-mean-square w

roughly scales with the amplitude of the surface forcing, that for low stratification WKB scaling holds, and that the vertical wavenumber and amplitude of w profiles increase within the surface mixed layers associated with deep convection. A similar determination of w has been carried out on Slocum gliders in the Mediterranean Sea (Merckelbach et al., 2010), again illustrating the possibility of using gliders to observe oceanic vertical velocities.

Spectra were used to assess noise in the Seaglider vertical velocity measurement. Profiles were taken from a constant stratification portion of the water column (400-900 m) in the open, quiescent, Norwegian basin. The spectra were integrated from where the slope flattened (1/240 Hz) to the Nyquist frequency (1/40 Hz) to find noise variance. Six different gliders in the region suggest similar Seaglider w error estimates of ± 0.2 cm s^{-1}. It should be noted that this value is considered the precision of the w measurement, not the accuracy. It is possible that a full depth offset, or low frequency systematic error exists due to improperly known values of the Seaglider vehicle volume or compressibility. However, as will be mentioned below, a high-pass filter is used in this analysis to look at velocity fluctuations, making offsets and low frequency errors irrelevant. Therefore we adopt an error estimate of 0.2 cm s^{-1}, consistent with the application outlined below.

3.3.2 Large-Eddy method

The method of estimating dissipation employed in this analysis is based on a simple scaling of the turbulent kinetic energy (TKE) equation (Taylor, 1935). We refer to this scaling as the 'Large-Eddy Method' or LEM. The method relies on the hypothesis (Kolmogoroff, 1941) that a steady turbulent energy cascade exists which allows measurements of the relatively large energy-containing scales to be used to infer the energy loss at viscous scales (Moum, 1996). Energy is introduced to the turbulent flow by instabilities in the large scale mean. In a steady state, this energy must be passed to smaller and smaller scales until it can be dissipated by viscosity. Described by the

Kolmogoroff scale, $\eta = (\nu^3/\varepsilon)^{1/4}$, the dissipation scale for ocean turbulence can be on the order of millimeters. This level of spatial resolution is well beyond the sampling capacity of the standard Seaglider. Assuming no leakage of energy (by, for example, non-dissipative linear internal waves), the cascade of TKE may be described by the energy of the largest eddies in the turbulent flow and their overturning time scale (Tennekes and Lumley, 1972). We let q' be a velocity scale of the largest eddies, and ℓ be their length scale. The eddy timescale may be written as $\tau \sim \ell/q'$ and dissipation, ε, scales as

$$\varepsilon \sim \frac{(q')^2}{\tau} \sim \frac{(q')^3}{\ell}. \tag{3.5}$$

A physical interpretation of equation 3.5 is that the kinetic energy, $(q')^2$, of a turbulent eddy is dissipated in the time it takes to overturn once, $\tau \sim \ell/q'$.

This scaling has been investigated by many authors including Moum (1996), Peters et al. (1995), and Gargett (1999). These authors find the scaling holds in a variety of oceanic regimes, including regions of low average dissipation containing sporadic energetic events (Peters et al., 1995). For stratified flow, a modification may be obtained by using the Ozmidov length, $L_{oz} = \varepsilon^{1/2} N^{-3/2}$, for ℓ in equation 3.5. The Ozmidov length is a measure of the maximum vertical overturn displacement that may occur for a given turbulent energy level and stratification (Thorpe, 2005). Rearranging equation 3.5 using $\ell = L_{oz}$, and introducing a proportionality constant c_ε, leads to an expression for the estimate (e) of dissipation of TKE which is explicitly independent of ℓ:

$$e = c_\varepsilon N (q')^2. \tag{3.6}$$

Use of the Ozmidov scaling in equation 3.6 is equivalent to assuming the overturning timescale of the largest eddies is $1/N$. D'Asaro and Lien (2000a) investigate the scaling in equation 3.6 in their discussion of the wave-turbulence transition, finding

that it should hold in sufficiently high energy environments. The high energy regime where equation 3.6 holds is defined in D'Asaro and Lien (2000b) as the "stratified turbulence" regime where the internal wave bandwidth of the vertical wavenumber shear spectra becomes small. The shear spectra in Figure 14 of Seim et al. (2010) indicate the FBC is energetic enough to be considered part of the stratified turbulence regime.

Equation 3.6 is, of course, still implicitly dependent on a length scale, the length scale over which the velocity fluctuations are calculated. The appearance of the buoyancy frequency, N, in equation 3.6 may also prove problematic for well-mixed layers, however we still find it advantageous to have an "ℓ-less" estimate of ε. Following Gargett (1999) we will use the vertical velocity, w, to define the velocity scale q'. D'Asaro and Lien (2000a) note that for stratified flows with a large internal wave component, kinetic energy is anisotropic and concentrated in the horizontal motions of the waves. Vertical kinetic energy, however, is nearly equipartitioned between waves and turbulence, making vertical kinetic energy a more appropriate choice to study turbulence (D'Asaro and Lien, 2000a). Unlike the ADCP measurements in Gargett (1999), who must use the velocity profile to define both q' and ℓ in equation 3.5, we have parallel density measurements which we use to define the buoyancy frequency used in equation 3.6. We determine c_ε by a comparison of bulk dissipation properties of the FBC as observed from sg005 and the 2008 microstructure survey.

3.3.3 Choosing the Scales

In order to proceed with the estimate of dissipation the velocity and length scales must be determined. We are interested in the kinetic energy and length scales of the largest turbulent motions in the flow field that lead to dissipation. Therefore, the influence of non-dissipative motions such as linear internal waves must be suppressed. A strict scale separation between the internal wave regime and the turbulent regime does not exist in the ocean, and separating turbulent and internal wave motions has

been a long standing problem. However, low vertical wavenumber motions which are clearly related to internal waves or tidal frequency motions may be removed from the Seaglider w record.

In the first step toward obtaining the velocity scale q', a high pass filter is run over the full $w(z)$ profile to obtain a profile of high frequency velocity fluctuations, $w_{hp}(z)$. The filter removes energy associated with low wavenumber motions which are clearly not related to turbulent overturns and has the added benefit of reducing errors associated with any improperly determined flight parameters. As Frajka-Williams et al. (2011) point out, adjustments to the flight model parameters tend to influence low frequency characteristics of the $w(z)$ profile, for example the full depth offsets or large scale divergence. Using $w_{hp}(z)$ removes these low frequency error signals. As noted previously, it is not guaranteed that the filter removes all internal wave motions. We will rely on the agreement between the LEM and VMP dissipation estimates to determine whether non-dissipative motions have been satisfactorily removed.

A fourth order Butterworth high pass filter with a lower cutoff wavelength, λ_c, of 30 m is used. For cutoff lengths shorter than 100 m, the method does not appear to be sensitive to the exact choice of λ_c. A larger λ_c produces higher values of the dissipation estimate profile, which in turn requires a smaller value of c_ε to match the VMP data, but no change in profile shape is evident until λ_c exceeds about 100 m. It is possible that in the FBC the energetic internal wave field leads to this insensitivity. The internal wave field is greatly enhanced relative to the Garrett-Munk spectrum (Fer et al., 2010). The internal waves may be highly nonlinear in the FBC, leading to significant breaking and dissipation. Thus, if much of the internal wave energy is dissipated, a larger λ_c which includes some internal wave energy does not reduce the agreement of the LEM with the VMP dissipation estimates. With this possibility in mind, the smallest λ_c possible has been chosen to allow application of the LEM to regimes other than the FBC. A value of $\lambda_c = 30$ m corresponds to about 300 seconds of glider flight or about 15 sample intervals. Finally, the velocity scale q' is calculated

as the root-mean-square value of the $w_{hp}(z)$ profile over a moving 10 m window. The window ensures that q' is a representative velocity scale over several eddy length scales, which we take to be on the order of the Ozmidov scale. For comparison, the implied Ozmidov scale (calculated from the Seaglider LEM measurements) in the FBC is approximately lognormally distributed and has a maximum likelihood estimate (standard deviation) of 0.77 (2.4) m. The corresponding values from the VMP survey are 0.51 (3.13) m.

Several choices of length scale have been explored. The first, Thorpe displacements (d'), are calculated as the vertical distance between the depths of a given isopycnal in an observed profile and in the profile resorted into its statically stable equivalent. The Thorpe scale, L_{th}, is then obtained by taking the root-mean-square of d' over the vertical extent of an individual overturn event. The Thorpe scale has the advantage of being a direct measurement of overturning scales and of being unaffected by internal wave motions. However, the Seaglider vertical sampling resolution of 1.2-2 m is coarse relative to typical L_{th} values, particularly in regions of strong stratification. Additionally, the slant profiling pattern of the Seaglider could produce spurious L_{th} in strong horizontal gradient regions near Kelvin-Helmholtz instabilities or steep internal waves (Smyth and Thorpe, 2012). Furthermore, it is possible to infer dissipation directly from Thorpe displacements, in some cases, using the relation $\varepsilon_{th} = 0.64\, L_{th}^2 N^3$ (Dillon, 1982) and therefore adding a dependence on w may introduce undue complication. The full analysis described below was also carried out using Thorpe displacements in equation 3.5, and the results were not qualitatively different from those presented. However, as mentioned above, the length scale chosen for the LEM presented here is L_{oz}.

The Ozmidov length scale was chosen for several reasons. First, the definition of L_{oz} as the largest scale at which overturns may occur for a particular turbulent energy level and stratification is consistent with the physical interpretation of the LEM. Additionally, the revised formulation (eq. 3.6) leads to a continuous dissipa-

tion profile, unlike the Thorpe displacements which give undefined values of e where $L_{th} = 0$ or is below the vertical resolution of the observations, which is the case for much of the record. Finally, pervious studies have shown the scaling in equation 3.5 with $\ell = L_{oz}$ to have better agreement with dissipation-scale estimates than equation 3.5 with $\ell = L_{th}$ (Moum, 1996). Equation 3.6 is employed throughout the following analysis.

3.4 Method Validation

3.4.1 VMP & Seaglider comparison survey

A procedure for calculating $q'(z)$, and hence e, has been outlined above. To complete the estimate of dissipation, the proportionality constant c_ε was determined by calibration with the 2008 VMP survey. Of the 90 VMP casts collected, 57 are close to the Seaglider survey region and have been used for the comparison. These are shown in blue in Figure 3.2. From the full three month deployment, 108 dives of sg005 were selected for comparison and are plotted in magenta in Figure 3.2. The Seaglider was launched 21 hours after the VMP survey was completed, making a direct calibration of the Large-Eddy Method impossible. Instead, survey-averaged profiles and probability distribution functions of dissipation were used. When calculating survey-averaged profiles from both the Seaglider and the VMP, only casts which encounter the overflow plume have been considered. It will be shown below that both the VMP and the Seaglider surveys adequately sampled the mesoscale variability of the overflow.

As a consistency check on the Seaglider vertical velocities in the FBC, the distribution of w observations from sg005 was compared with the downward looking ADCP on mooring B2 (Fig. 3.4). ADCP vertical velocity was collected from each of the useable 2 m vertical depth bins which are 6 to 66 m below the instrument: nominally between 610 and 676 m, but due to current-induced knockdown, the ensonified region varies between 594 m and 690 m. Typically the ADCP measured the interfacial layer

between the plume and the ambient Atlantic above. The Seaglider vertical velocities were taken from 42 dives located within 10 km of the mooring. The distribution of Seaglider observed w from depths between 600 and 700 m is plotted in the bottom panel of Figure 3.4. The distributions of ADCP and Seaglider derived w overlap and have similar means and standard deviations: mean (standard dev.) for the glider is $-0.29\,(2.9)$ cm s^{-1} and for the ADCP is $-0.73\,(2.5)$ cm s^{-1}. A quantile-quantile plot in the upper panel of Figure 3.4 plots the empirical distribution of the ADCP velocities against that of the Seaglider. The linear relationship indicates the similarity of the two distributions and increases our confidence in the Seaglider w measurement.

Survey-Averaged Profiles

The height-above-bottom of the 3°C isotherm, a good indication of the maximum stratification in the interface between the overflow plume and the overlaying Atlantic water, is plotted against yearday of 2008 in Figure 3.5. The strong mesoscale variability of the overflow with a period of about 3.5 days is readily apparent. This overflow variability has been documented by other authors, and has significant dynamical consequences for the plume (Geyer et al., 2006; Darelius et al., 2011). The oscillation must be taken into consideration when comparing the Seaglider and VMP surveys. Thick and thin vertical lines at the bottom of Figure 3.5 indicate the times of VMP casts and Seaglider dives. The gap around yearday 157 shows the 21 hour delay between the end of the VMP cruise and the beginning of the sg005 mission. Evidently both the VMP and sg005 sample all phases of the mesoscale variability, as can be seen from the temporal coverage of the two surveys. Average profiles will be unbiased with respect to the phasing of the oscillation. We may reasonably expect the average profiles to be comparable between the two instruments, and representative of the mean conditions of the overflow plume.

In light of the presence of the mesoscale oscillation, the survey-averaged profiles of the VMP and sg005 presented in Figure 3.6 have been calculated with three different

vertical coordinates: the shallowest 200 m was computed with respect to the surface; the bulk of the water column was calculated with respect to vertical distance from the 3°C isotherm; and the bottom 150 meters were averaged with respect to height above the bottom. A linear least squares fit between the Seaglider LEM and the VMP survey-averaged profiles produced a proportionality constant $c_\varepsilon = 0.37$, resulting in the survey-averaged profile in Figure 3.6**c**. This value is broadly consistent with previous studies using equation 3.6, for example $c_\varepsilon = 0.3 - 0.6$ in D'Asaro and Lien (2000b) and $c_\varepsilon = 0.73 \pm 0.06$ in Moum (1996). The noise level, i.e. the lowest detection limit, of the LEM was found by substituting the velocity noise $w = 0.002$ m s^{-1} (section 3.33.3.1) into equation 3.6, giving

$$e_{noise} = (1.4 \times 10^{-6})N. \tag{3.7}$$

For typical FBC buoyancy frequencies ranging between 1 and 4 cph, equation 3.7 gives e_{noise} between $2.5{\times}10^{-9}$ and $1{\times}10^{-8}$ W kg^{-1}. The survey-averaged profile of e_{noise} is plotted as a dashed line in Figure 3.6**c**.

Figure 3.6**a** shows the typical vertical density structure of the FBC region. Near the surface, a seasonal pycnocline overlies a thick, modestly-stratified, layer of Atlantic water ($27.4 \lesssim \sigma_\theta \lesssim 27.6$ kg m^{-3}). The Atlantic layer then lies above a high stratification interface ($27.6 \lesssim \sigma_\theta \lesssim 27.9$ kg m^{-3}) capping the relatively well mixed overflow plume ($\sigma_\theta \gtrsim 27.9$ kg m^{-3}). Dissipation of TKE (Fig. 3.6**c**) varies over 2.5 orders of magnitude throughout the water column. Dissipation is elevated near the surface, falls to a minimum in the Atlantic water above the interface, and gradually increases with depth until the overflow plume layer is reached, remaining high to the bottom. The Seaglider dissipation estimate falls to near its noise level in the Atlantic waters around 250 m above the 3° isotherm. The Seaglider LEM and the VMP dissipation estimates covary over the full water column (Fig. 3.6**c**). Because of the large number of observations that go into the average profiles, 95% confidence intervals are very tight. A more reasonable indication of the agreement between the

Seaglider LEM and the VMP is found by looking at the ratio of the survey-averaged profiles (Fig. 3.6**d**). The vertical mean (standard deviation) of $\varepsilon_{\mathrm{VMP}}/e_{\mathrm{LEM}}$ referenced to the 3° isotherm (Fig. 3.6**d**, center row) is 1.01 (0.53). Faint gray lines in Figure 3.6**d** show that the Seaglider LEM agrees with the VMP to within a factor of two. A two sample Kolmogoroff-Smirnoff test of the survey-averaged profiles in Figure 3.6**c** shows no significant differences in the distributions of the Seaglider LEM and the VMP dissipation.

In Figure 3.7 the same ratio of survey-averaged dissipation profiles is plotted for all Seagliders which entered the FBC region. In this case only the average with respect to the 3° isotherm is computed and the vertical limits are reduced because some gliders did not encounter thick overflow layers. Some of these gliders spent only a few dives in the plume and are not as well suited to comparison with the VMP survey as sg005 (in the sense of not sufficiently sampling the mesoscale variability), however the profile is displayed to show that the LEM is applicable to other Seagliders. We conclude that the Seaglider LEM accurately measures dissipation of TKE in the FBC to within a factor of two.

Outside the FBC, on the less energetic IFR, microstructure measurements are not available for comparison with the Seaglider, and therefore we cannot rule out the possibility that the error is larger than the factor of two found in the channel. In order for the Large Eddy scaling (equations 3.5 and 3.6) to hold, the assumptions of a cascade of energy through fully developed turbulence must be valid. This is certainly the case in the FBC, but may not be entirely valid on the IFR, necessitating caution when interpreting results from the ridge. There are, however, examples of energy cascades observed in lower energy environments (Lueck et al., 1997) and indications that equation 3.5 holds in regions of low average dissipation containing individual energetic events (Peters et al., 1995).

Probability Distribution Functions in Layers

In a second method of comparison between the VMP and Seaglider, dissipation estimates from the FBC region have been sorted into three layers: Atlantic (AL), Interfacial (IL) and Overflow Layer (OL). The OL is the quasi-homogeneous layer of the bottom-attached overflow plume defined as the cold ($< 3°C$) layer above the bottom where the temperature gradient is less than 0.004 °C m^{-1}. The AL is the ambient warm water, excluding the upper 50 m influenced by surface forcing. The base of the AL is identified as the deepest point where the temperature is greater than 7.7°C and the temperature gradient is less than 0.01 °C m^{-1}. The IL is the strongly stratified layer between the top of the OL and the bottom of the AL, where the bulk of the entrainment occurs. Typical thicknesses of these three layers in the FBC are approximately 70m, 100m, and more than 600 m for the OL, IL and AL respectively. The three layers have been chosen because they represent regions where mixing is driven by different mechanisms: turbulence due to internal wave breaking in the ambient (AL); shear instabilities and entrainment (IL); and shear and boundary layer processes (OL).

Probability distribution functions (PDFs) of the Seaglider (colored lines) and the VMP (gray patch) in each layer are plotted in Figure 3.8. The column on the left shows the distributions of the VMP and sg005, on which the calibration of c_ε is based. The right column adds the distributions of all Seagliders that made dives in the FBC region over the full 3 years of field work. Colored circles and gray squares show the maximum likelihood estimate (mle) for each Seaglider and VMP layer distribution. Horizontal bars plotted over the VMP mle squares show 1/2 and 2 times the mle. The Seaglider LEM distributions cover the range of the VMP distributions fairly well, with the best agreement in the OL, and the worst in the IL. The stratification-dependent noise level of the LEM results in fewer measurements of low dissipation, causing disagreement between the VMP and Seaglider PDFs at low magnitude in the

IL and to a lesser extent in AL. The dissipation estimates in the FBC are nearly lognormally distributed. Agreement at high values is most important for lognormally distributed variables. Agreement is better for the high-magnitude tail of the layer PDFs than for the low side. As in Figure 3.7, the right column of Figure 3.8 indicates that the LEM is applicable to the other Seagliders deployed in the FBC.

3.5 Results & Discussion

3.5.1 Seaglider-inferred dissipation section

During its June 2008 deployment, sg005 spent a considerable amount of time targeting mooring B2, after which it traveled out of the FBC and completed a section normal to the IFR. Deployment-length sections of temperature and inferred dissipation rate plotted against profile number are presented in Figure 3.9. Most of the first 400 profiles were in the FBC and constitute the subset used for comparison with the VMP. While trying to maintain its position near mooring B2, occasionally the glider was advected onto the Faroe Plateau (profiles 280-360) where strong anti-cyclonic flow was a persistent hazard to navigation. Those dives on the Faroe Plateau were not included the inter-calibration described in the preceding sections. Figure 3.9 shows high values of dissipation in the overflow plume ($10^{-7} - 10^{-6}$ W kg^{-1}), and much lower levels in the Atlantic layer above. Dissipation is elevated in the near surface layers throughout the deployment. Once the glider exited the FBC, around profile 400, dissipation decreased in the deep overflow layer. However, the Seaglider continued to observe slightly elevated dissipation above the ridge topography in a layer of diluted overflow water (profiles 450-600), and in the Iceland-Faroe Front (600-700). In the quiescent deep waters north of the IFR the sections show very little measurable dissipation.

The literature of the FBC overflow contains many claims that all the important plume water mass transformation happens immediately downstream of the FBC. It

is clear from Figure 3.9 (and Fig. 3.11, later) that the FBC terminus is an extremely active turbulent region. However, Figure 3.9 also indicates that turbulence is elevated in the more diluted overflow layer on the IFR (profiles 450-600), which suggests that entrainment is still taking place downstream of the FBC.

3.5.2 Mixing 'Hot Spots'

As mentioned above, previous studies have, justifiably, focused on the Faroe Bank Channel outflow where direct mixing estimates are now available on discrete ship tracks (Fer et al., 2010). An application of the LEM to the three years of Seaglider data allows us to begin to describe the spatial distribution of mixing of the overflows along the IFR. Individual profiles of dissipation have been integrated over the thickness of the plume (50 m above the depth of the 27.65 isopycnal, H_p, to the bottom, HAB= 0) to produce the map of plume-integrated dissipation ($\rho_0 \int_0^{H_p} \varepsilon dz$) shown in Figure 3.10. The integrals are multiplied by a reference density, $\rho_0 = 1027.4$ kg m^{-3}, to give units of W m^{-2}. The field of plume-integrated dissipation reveals several interesting regions of enhanced mixing on the IFR, including the regions downstream of the primary and secondary sills of the FBC, and in a relatively undiluted IFR overflow plume adjacent to the Iceland shelf.

Downstream of primary and secondary FBC sills

The FBC region stands out as an energetic area where plume-integrated dissipation reaches a maximum of 330 mW m^{-2}, two orders of magnitude above most of the IFR. The Faroe Bank Channel contains both a primary and secondary sill separated by a shallow basin approximately 50 km long and 900 m deep. The primary sill, which is the narrowest and shallowest part of the channel, is 840 m deep and coincides with a horizontal constriction to about 10 km. The secondary sill, marking the terminus of the FBC, is wider and slightly deeper at about 850 m. Beyond the secondary sill the channel opens onto the Atlantic flank of the IFR. Downstream of both the primary

and secondary sills plume-integrated dissipation jumps significantly in two distinct energetic regions (Fig. 3.11).

The energetic region downstream of the secondary sill corresponds well to the regions of enhanced mixing identified in discrete sections by Mauritzen et al. (2005) (100 km downstream of primary sill), Girton et al. (2006) (20-90 km) and Fer et al. (2010) (∼80 km). The largest overflow velocities are often found in this region, where Fer et al. (2010) observed a maximum speed of 135 cm s^{-1}. Analysis of the Seaglider dataset (Beaird et al. 2012 in prep) shows that downstream of the secondary sill the FBC overflow plume widens and thins considerably, while doubling its decent rate. This transition occurs as the plume evolves from a channelized gravity current to a dense flow on a slope. Numerical models produce plume widening in this region (Riemenschneider and Legg, 2007; Seim et al., 2010) which is interpreted by Pratt et al. (2007) as a transverse hydraulic jump. Observations also suggest hydraulic control downstream of the secondary sill region (Girton et al., 2006) where Froude numbers become critical (Mauritzen et al., 2005; Fer et al., 2010; Seim et al., 2010). Additionally, these previous studies, as well as the Seaglider data, indicate that the FBC plume bifurcates into a shallow and a deep branch at a topographic bump located at 61.9° N, 10.12° W.

All these observations are consistent with the large region of enhanced turbulent dissipation centered around 61.75° N, 9.5° W shown in Figure 3.11, referred to as 'Mixing Zone 2' (MZ2). Plume-integrated dissipation is elevated (up to 330 mW m^{-2}) from west of the secondary sill, at about 9° W, to the topographic feature at 10.12° W. The mean plume-integrated dissipation over the whole area is 19 mW m^{-2}. The Seaglider is depth-limited to 1000 m, so from Figure 3.11 it is unclear how far downstream the high dissipation extends in the deep branch of the overflow. However, the extent of the elevated dissipation region can be seen on the shallow side of the plume. It appears that the highest dissipation in the shallow branch has relaxed to IFR mean values by 100 km downstream of the primary sill (∼ 62° N, 9.5° W).

The high spatial resolution of the Seaglider surveys resolves two different zones of enhanced mixing: the previously discussed region beyond the secondary sill (MZ2); and a region immediately downstream from the primary sill (Mixing Zone 1, or MZ1) (Fig. 3.11). Coarser section spacing in previous studies of the FBC has not resolved the separation between these two regions. MZ1 and a relatively quiescent region separating it from MZ2 are contained in the basin between the sills. MZ1 has a maximum plume-integrated dissipation of 195 mW m^{-2}, and the mean is 21 mW m^{-2}, slightly higher than in MZ2. Girton et al. (2006) use three different methods to locate the section of hydraulic control in the FBC, finding general agreement that the critical section lies between 20 and 90 km downstream of the primary sill. The most confident estimate was found to be 50 km downstream, at the secondary sill. That there are two distinct regions of enhanced dissipation in Figure 3.11 seems consistent with the spread in the estimates of the location of hydraulic control, perhaps suggesting time variability of the control section location.

Western Valley jet

A previously undocumented area of enhanced turbulent dissipation is located adjacent to the Iceland shelf at the northwestern end of the IFR (Fig. 3.10). A slight depression in the ridge-crest where the IFR intersects the Iceland shelf, sometimes referred to as the Western Valley (WV), has long been thought to provide a pathway for a portion of the dense overflow across the IFR. Current meter records in the region indicate long-term near bottom velocities are steady and directed along the Iceland shelf with mean speeds of 50 cm s^{-1} (Perkins et al., 1998). It is unclear from the Perkins et al. (1998) study if the steady near bottom velocities imply a steady overflow transport because contemporaneous temperature records are not published with the current meter data. Many (31) Seaglider transects were made in the region, often observing the WV overflow in a 10 km wide jet with 50-70 cm s^{-1} absolute geostrophic velocities. Figure 3.12 shows one such crossing of the WV overflow jet by sg016 in

late July 2008. The maximum absolute geostrophic velocity in the overflow during that crossing was 57 cm s^{-1}. The temperature section shows the narrow jet of cold water balanced against the Iceland shelf break. The accompanying dissipation section reveals elevated turbulence in the jet. The set of Seaglider transects intersecting the Iceland shelf indicates that the overflow transport in the WV is much more variable than the current meter records of Perkins et al. (1998) would suggest. Observed dense water ($\sigma_\theta \geq 27.8$ kg m^{-3}) overflow transports calculated from absolute geostrophic velocities range between 0.07 and 2.13 Sv in six transects made over a 12 day period in June/July of 2009 (Beaird et al., 2013). An episodic overflow event of similar duration appears in the observations of Perkins et al. (1994).

Figure 3.13 shows that the narrow WV overflow region, delineated by the low bottom temperatures in the right panel, is also a region of high dissipation. Maximum plume-integrated dissipation reaches 250 mW m^{-2}, with a mean value of 13 mW m^{-2} in the WV overflow jet. A clear advantage of the Seaglider LEM is the identification of regions such as this one, which was observed during the course of a survey designed to map the hydrography of overflows on the IFR. Dedicated microstructure surveys in the region have never been carried out, so it is only through this ancillary inferred Seaglider measurement that the energetic region was discovered. While the Atlantic water above the overflow in the WV is much the same as that overlying the FBC, there are gradients in Atlantic water properties across the ridge. Additionally, very fresh coastal water from Iceland is occasionally advected off the shelf into the surface waters of the WV. Mixing between the overflow waters and different ambient waters influences the downstream properties of the overflow (Price and Baringer, 1994), potentially resulting in distinct contributions to North Atlantic Deep Water from the WV and FBC overflows. Therefore, mapping the regions of energetic turbulence and the ambient properties by Seagliders provides insight into dense water production by these overflows.

3.6 Summary

Levels of turbulent dissipation have been mapped in one of the two major source regions of North Atlantic Deep water. Mixing and entrainment in these small overflow regions are of great importance to the global abyssal circulation and the climate system. A scaling has been investigated which infers dissipation of turbulent kinetic energy from finescale vertical velocity observed by an autonomous vehicle.

The Large-Eddy Method (LEM) defined here assumes that most of the kinetic energy in a turbulent eddy is dissipated in the time it takes to overturn once. The scaling requires a length scale and a velocity scale of these eddies. The length scale is taken to be the Ozmidov length scale, which is the largest size of an overturn in stratified flow. The velocity scale is estimated from the vertical velocity fluctuations, after removing the low wavenumber and internal-wave induced contribution by a suitably chosen high-pass filter, as the root-mean-square over several eddy lengths. The dissipation estimate depends on a proportionality constant which is determined by calibrating the results from a dedicated Seaglider, co-located with a cruise, against dissipation measurements from a shipboard microstructure survey. A comparison between the Seaglider-inferred dissipation and the microstructure measurements indicate that the LEM reproduces the direct measurements within a factor of two. Survey-averaged profiles of dissipation rate co-vary over several orders of magnitude. The noise level of the LEM is dependent on stratification and varies between 2.5×10^{-9} and 1×10^{-8} W kg^{-1} in the Faroe Bank Channel. The LEM was then tested on 12 other Seagliders which entered the FBC region over three years between November 2006 and November 2009, using the portions of the data collected in the vicinity of the cruise site. The survey-averaged profiles from each glider agreed well with the microstructure measurements.

The LEM, once calibrated, was then applied to the entire dataset of the 13 Seagliders deployed on the Iceland-Faroe Ridge. Maps of plume-integrated dissipation re-

vealed three regions of enhanced mixing. The largest dissipation rates were found in a mixing zone (MZ2), downstream of the secondary FBC sill, consistent with previously documented observations. MZ2 corresponds to suspected regions of hydraulic control, the bifurcation of the overflow plume, as well as a significant widening, thinning and increase in descent rate. The Seaglider data defined the size and diffuse location of MZ2 in a way previously unrealized by discrete ship tracks. Another FBC high energy region was found in MZ1 just downstream of the primary FBC sill. This region is separated from MZ2 by a relatively quiet region at the western end of the shallow basin between the two sills. Previous ship based observations did not resolve these two distinct regions which likely led to the range of values given for the downstream locations of the highest FBC mixing.

Finally a third, previously unknown, region of enhanced dissipation was found in a narrow jet of IFR overflow water leaning against the Iceland shelf break. The values of plume-integrated dissipation in the Western Valley jet were nearly as large as in the FBC. The location of energetic turbulence, and presumably vertical mixing, in the WV is important as the properties of the entrained water mass influence the eventual IFR contribution to North Atlantic Deep Water.

A method has been defined from which an estimate of dissipation of TKE can be made from a standard Seaglider. Comparison with a microstructure survey indicates that the Seaglider Large-Eddy Method is valid within a factor of two in the energetic FBC. The LEM does not have the high accuracy of more direct microstructure measurements, but it offers a relatively economical additional measurement from the increasingly common glider surveys worldwide. In particular the advantage of the LEM is in mapping regions of energetic turbulence with high spatial and temporal resolution. Used as an exploratory vehicle, the Seaglider and LEM may be able to provide focus for more detailed process studies.

3.7 Figures

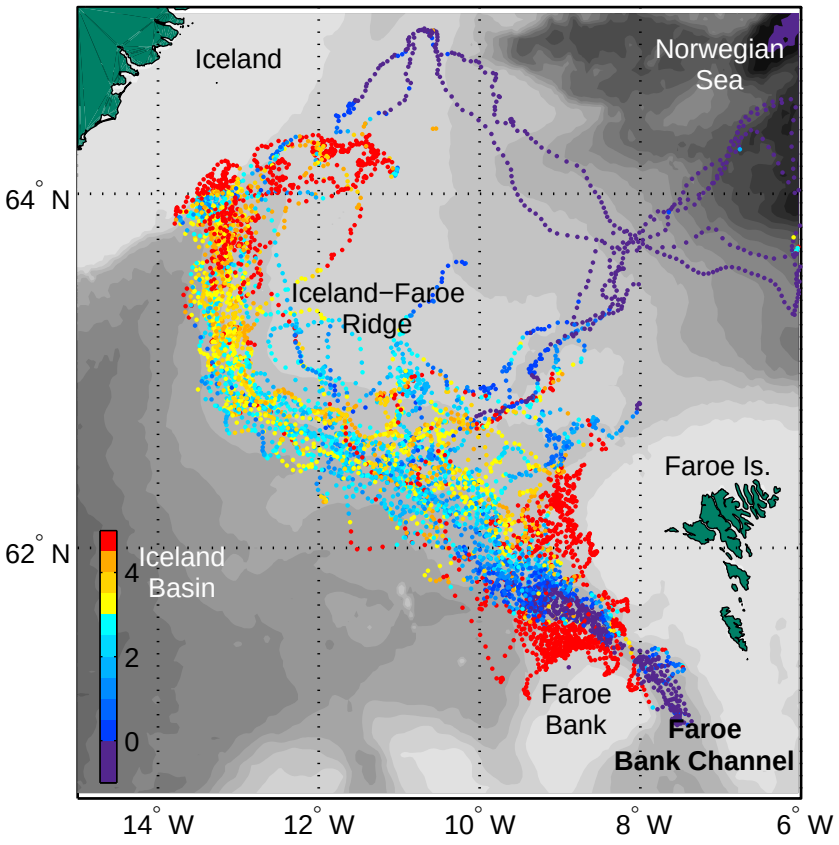

Figure 3.1: Location of all Seaglider dives on the Iceland-Faroe Ridge from November 2006 through November 2009. Each dot indicates the location of one dive/climb pair. Color is proportional to the bottom temperature [° C] with colorscale indicated at bottom left.

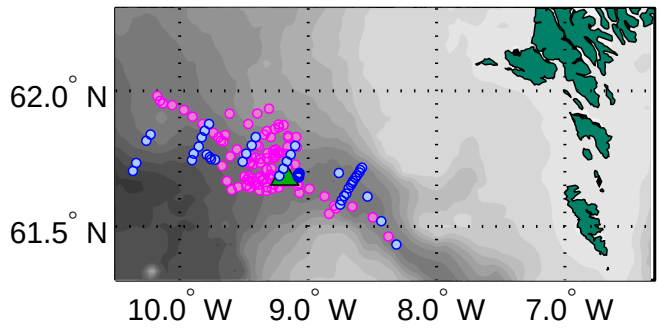

Figure 3.2: Location of 57 VMP casts from the 2008 cruise (blue circles), sg005's June 2008 dives in the FBC (magenta circles), and mooring B2 (green triangle).

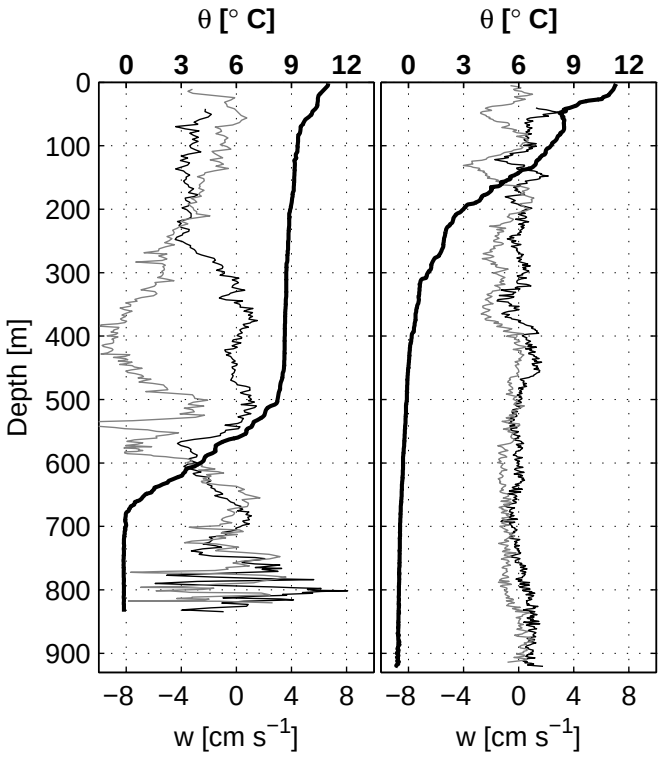

Figure 3.3: Velocity profiles from the dives (black) and climbs (gray) as well as potential temperature (thick black, refer to top axis) from two Seaglider dives. On the left is a dive in the FBC into the overflow plume. The right panel is a dive in a calm, deep, region north of the IFR in the open Norwegian Sea.

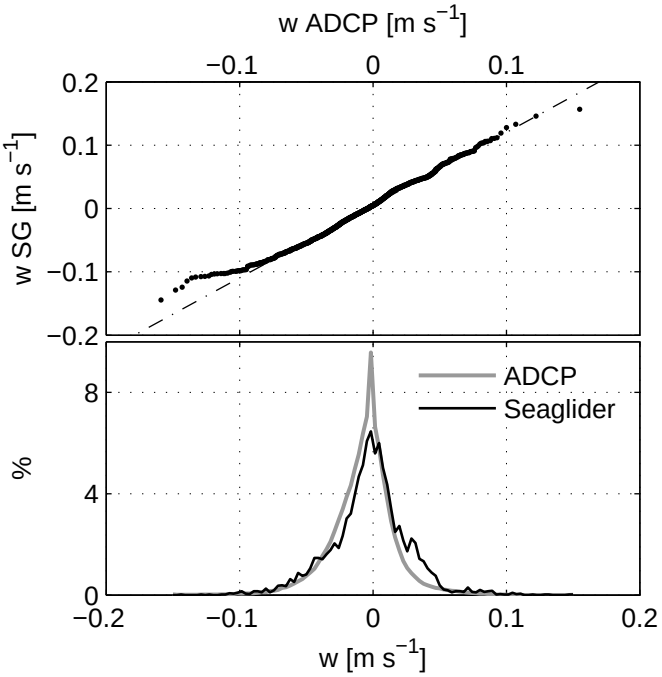

Figure 3.4: The lower panel shows histograms of vertical velocity from the ADCP on mooring B2 (gray) and from 42 dives made by sg005 (black) within 10 km of B2. Velocities are measured between 600 and 700 m by the glider and between 594 and 690 m by the ADCP. The top panel plots the empirical distributions of vertical velocity from the ADCP (x-axis) against that of sg005 (y-axis) in a quantile-quantile plot.

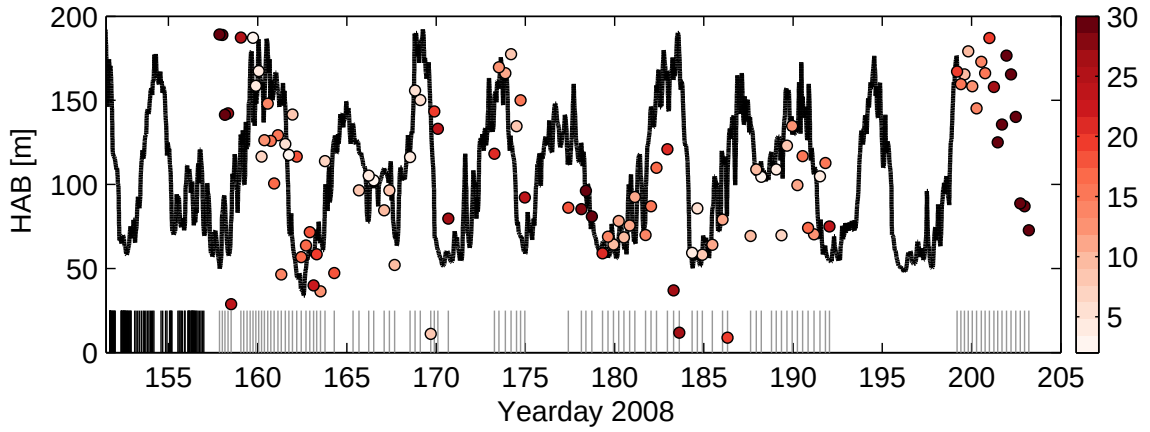

Figure 3.5: Time series of the height-above-bottom (HAB) of the 3°C isotherm from the B2 mooring (black). Short vertical lines indicate the times when the VMP casts (black) or sg005 dives (gray) took place. Colored dots are plotted at the HAB of the 3°C isotherm as seen by the Seaglider, and their color indicates the distance [km] between sg005 and mooring B2.

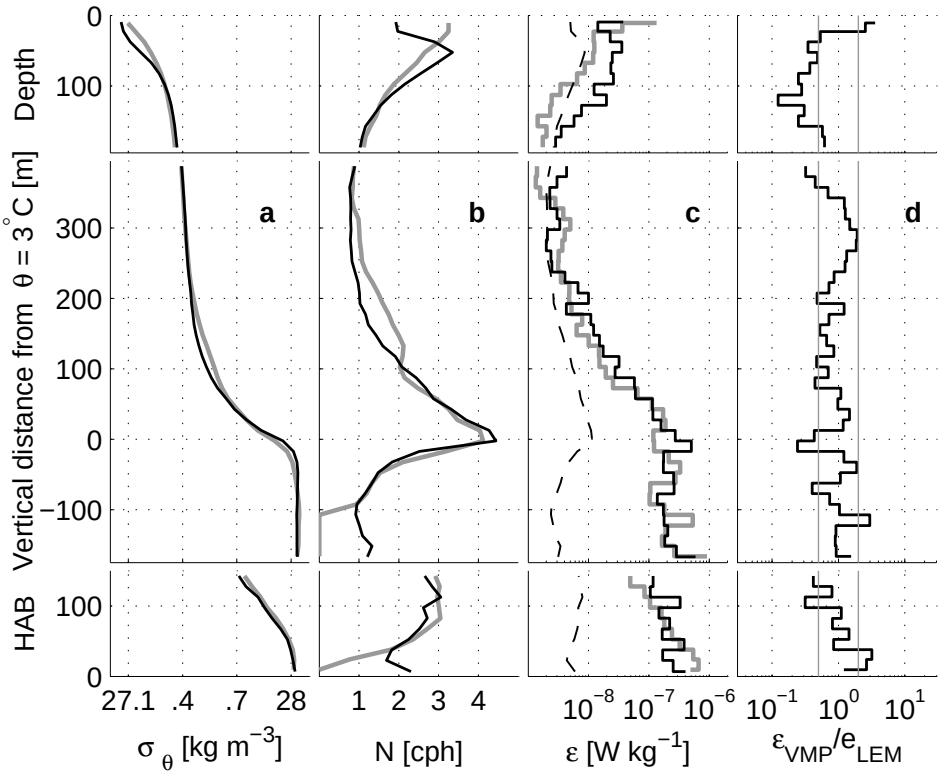

Figure 3.6: Survey-averaged profiles of potential density anomaly, σ_θ, (**a**), buoyancy frequency, N, (**b**), dissipation of TKE, ε, (**c**), and ratio of VMP to sg005 dissipation estimates (**d**). VMP profiles are plotted in gray, Seaglider (sg005) profiles in black. Profiles are averaged with respect to depth (top row), distance from the 3°C isotherm (center row), and height above bottom (bottom row) in 15 m bins. Average noise level (i.e. lowest detection level) for the LEM (eq. 3.7) is plotted as a dashed black line in **c**. Light gray lines in **d** show factor of 2 bounds on the estimate ratio.

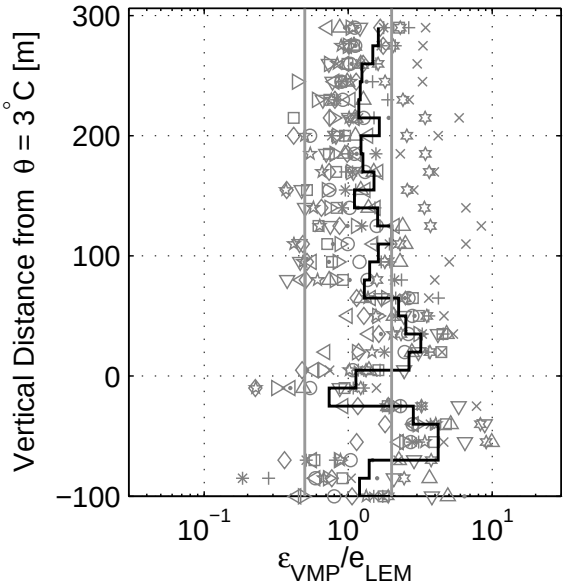

Figure 3.7: Ratio of Seaglider LEM survey-averaged profiles to the VMP average profile for all 13 gliders in the FBC region. Each gray symbol represents a different Seaglider deployment. Averages are made with respect to distance from the 3°C isotherm. Black line shows the mean of all profiles, light gray lines show factor of 2 bounds on the estimate ratio. Glider deployments are represented by the following symbols: $+$ for sg012 Sept. 2007, $\circ$ for sg104 Sept. 2007, $*$ for sg014 Sept. 2008, $\cdot$ for sg005 Sept. 2009, $\times$ for sg103 Feb. 2009, $\square$ for sg101 June 2007, $\diamond$ for sg005 June 2008, $\triangle$ for sg016 June 2008, $\triangledown$ for sg016 June 2009, $\triangleleft$ for sg016 Nov. 2007, $\triangleright$ for sg102 Nov. 2007, $\star$ for sg103 Nov. 2007, and a six-pointed star for sg101 Nov. 2008

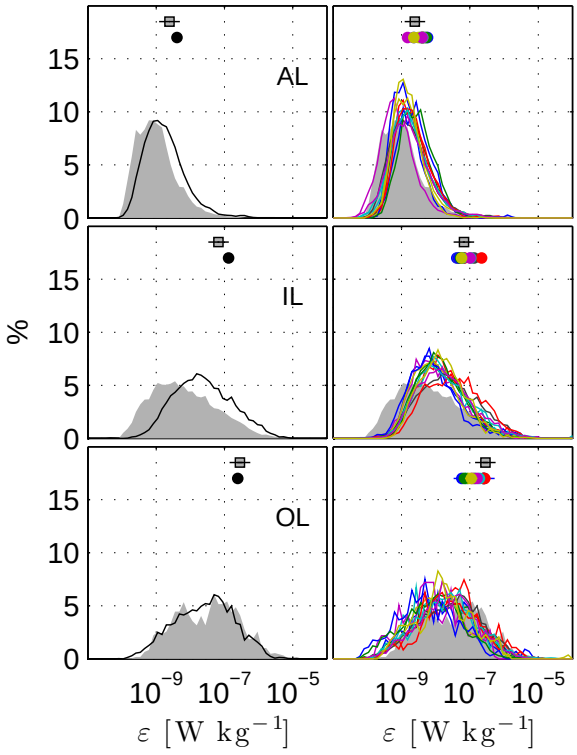

Figure 3.8: PDFs of ε from the VMP (gray patch) and e from the Seaglider (colors) broken into the Atlantic Layer (AL, top row), Interfacial Layer (IL, middle row), and Overflow Layer (OL, bottom row). The VMP and sg005 June 2008 deployment are plotted in the left column. All Seagliders from the 3 years of field work which entered the FBC region are plotted in the right column, along with the VMP. Colored dots plotted in each box show the maximum likelihood estimate (mle) of each distribution. The VMP mle is plotted just above the Seaglider values, with a horizontal line indication a factor of two range about the mle.

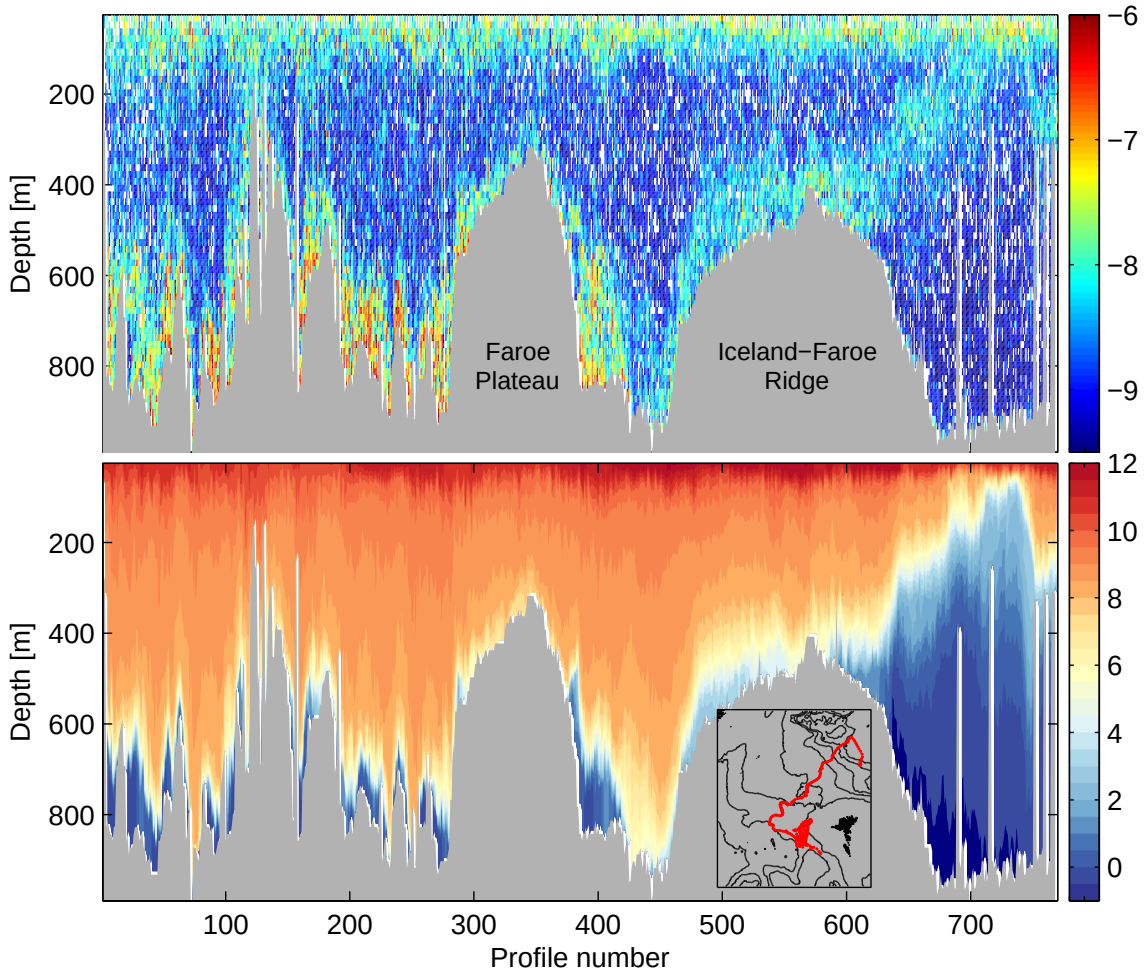

Figure 3.9: Top. Depth versus profile number section of dissipation, $\log_{10}(e)$ [W kg^{-1}], from the entire sg005 deployment, where each dive and climb is counted as a profile. Bottom. Corresponding temperature section [°C]. Inset map shows the dive locations in red, the FBC dives may be seen in more detail in Figure 3.2.

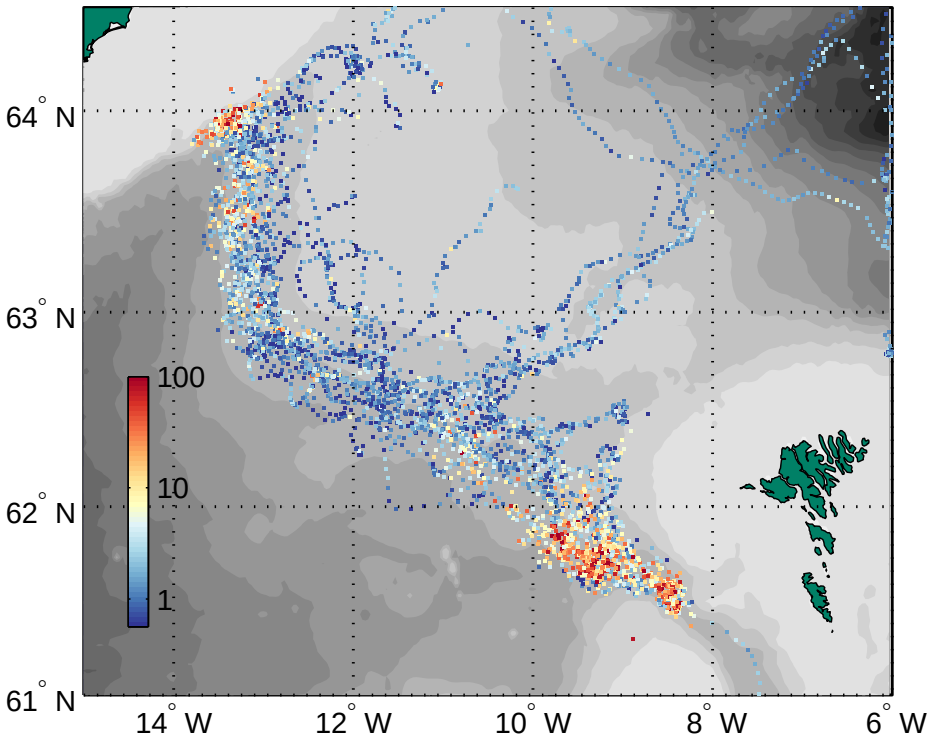

Figure 3.10: Vertically integrated dissipation rates over the plume thickness, $\rho_0 \int_0^{H_p} \varepsilon dz$ [mW m^{-2}], from all Seaglider data.

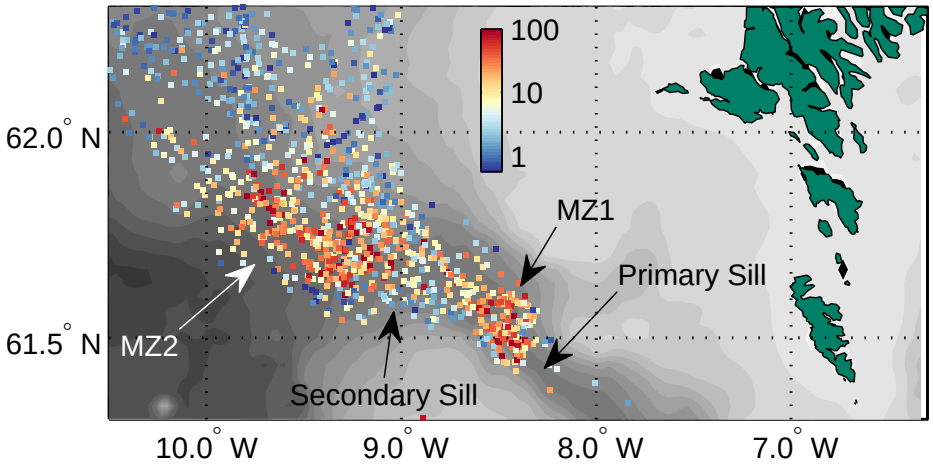

Figure 3.11: Vertically integrated dissipation rates over the plume thickness, $\rho_0 \int_0^{H_p} \varepsilon dz$ [mW m^{-2}], in the FBC. MZ1 and MZ2 indicate the general region of the two enhanced mixing locations described in the text.

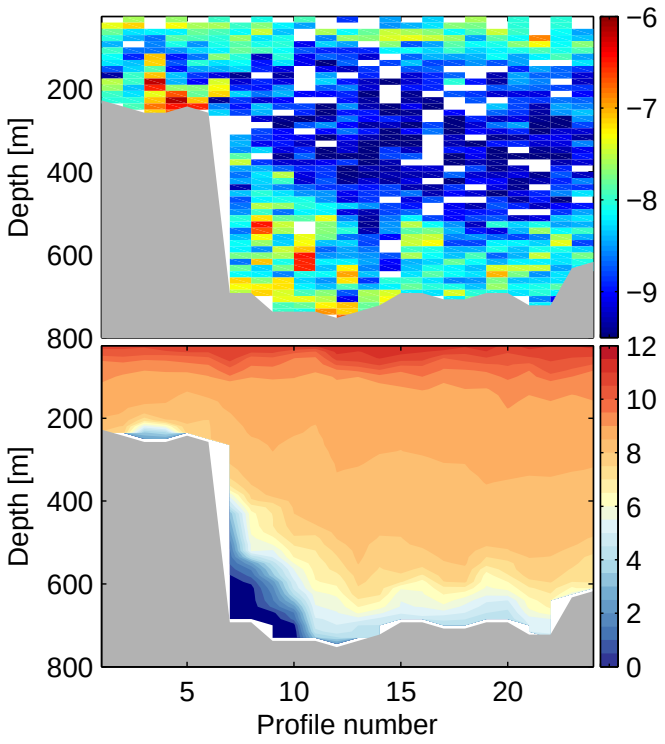

Figure 3.12: Top: Section of dissipation, $\log(e)$ [W kg^{-1}], from sg016 crossing the Western Valley 24-25 July 2008. Depth v. profile number where each dive and climb is counted as a profile. Bottom: corresponding temperature section [°C].

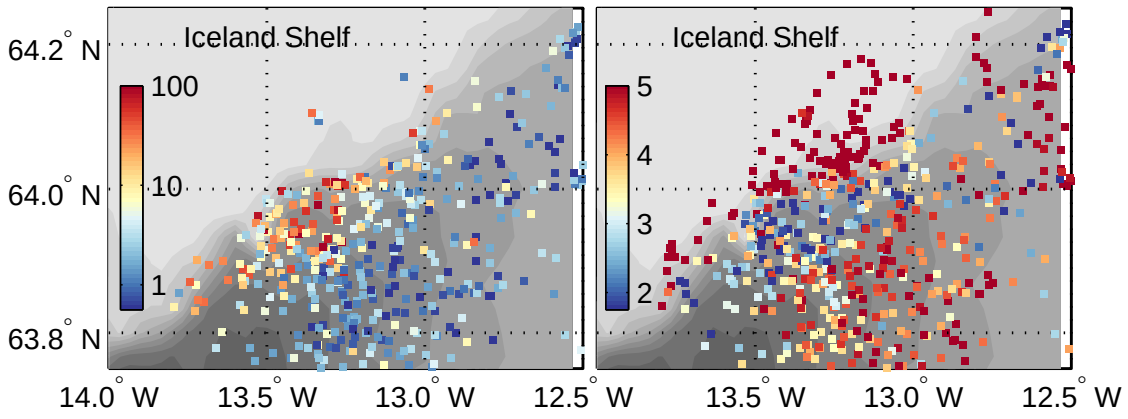

Figure 3.13: Vertically integrated dissipation rates over the plume thickness, $\rho_0 \int_0^{H_p} \varepsilon dz$ [mW m^{-2}], from the Iceland shelf break overflow (left). Bottom temperature [°C] near the Iceland shelf break (right).

Chapter 4

EVIDENCE OF DIRECT EXCHANGE OF LOW SALINITY INTERMEDIATE WATERS ACROSS THE ICELAND-FAROE RIDGE IN WINTER

4.1 Introduction

The Greenland-Scotland Ridge (GSR) separates the North Atlantic from the Nordic and Arctic regions. The Atlantic south of the ridge is predominantly warm and saline, whereas north of the ridge intense water mass modification produces large volumes of cold and relatively fresh waters. Subtropical Atlantic waters arrive at the ridge though the complex pathways of the subpolar/subtropical gyre boundary (Brambilla and Talley, 2008). Meridional flow across the GSR constitutes the headwaters of the globally significant Atlantic Meridional Overturning Circulation. The basic circulation is comprised of poleward flowing surface waters of Atlantic origin, and equatorward flowing dense water formed north of the ridge. The widest gap ($\sim$ 300 km) in the GSR is the Iceland-Faroe Ridge (IFR), the hydrography of which is dominated by the Iceland-Faroe Front (IFF, Fig. 4.1). The IFF is the boundary between the North Atlantic waters and Nordic waters at depths shallower than the IFR crest ($\sim$ 450 m) (Read and Pollard, 1992). Roughly locked to the IFR crest, the isopycnals of the IFF slope up and northward from the ridge. The front slopes more steeply in the west, where it sometimes coincides with the Jan Mayen front (Hansen and Østerhus, 2000), and gradually becomes more diffuse towards the Faroe side of the IFR (Read and Pollard, 1992). Geostrophic balance at the IFF supports the Faroe Current, which carries about 4 Sv (half) of the inflow of Atlantic water to the Nordic Seas (Hansen et al., 2003; Rossby and Flagg, 2012). The surface expression of the front, typically defined

as the 35 isohaline, exhibits significant variability in position on weekly to monthly timescales, but does not vary seasonally (Smart, 1984; Hansen and Meincke, 1979).

The front is baroclinically unstable (Allen et al., 1994; Allen and Smeed, 1996), producing a vigorous eddy field (Hansen and Meincke, 1979) (apparent in the SST of Fig. 4.1). Northward flow of Atlantic waters is focused slightly on the northwestern end where the IFR abuts the Icelandic plateau (Perkins et al., 1998) and at the relatively deep part of the IFR near the Faroe Plateau (Rossby et al., 2009). Cold, fresh, polar waters are carried to the western end of the front by the East Iceland Current (Jónsson, 2007). The trajectories of floats deployed in the Atlantic water south of the IFF by Rossby et al. (2009) illustrate the highly turbulent nature of the northward flow across the ridge.

The canonical description of the IFF as 'topographically locked' to the IFR crest can be somewhat misleading. This description suggests that the isopycnals associated with the IFF intersect the topography of the IFF somewhere near its crest. This simple picture ignores the fact that a layer of dense overflow water exists on the Atlantic Flank of the IFR (AIFR) south of the crest. The presence of the overflow means that some frontal isopycnals continue south of the IFR crest, lying nearly parallel to the AIFR topography (Beaird et al., 2013). The implication is that on some isopycnals the front is continuous from the Nordic Seas to the main pycnocline of the Iceland basin, via the dense overflow on the AIFR. This connection may play an important role in the water mass exchange discussed in this paper.

The typical vertical water mass structure over the AIFR in temperature-salinity (TS) space consists of an approximately linear relationship connecting the upper layer waters of Atlantic origin with the dense Nordic Seas overflow layer above the seabed (Fig. 4.2, see dark gray background patch). The observations reported here reveal a seasonal intrusion of low salinity intermediate water between the Atlantic and overflow waters, disrupting the typical two layer structure.

Low salinity waters of polar origin have been described in the IFF region by nu-

merous authors (Meincke, 1978; Read and Pollard, 1992; Hallock, 1985; Allen and Smeed, 1996). The freshest waters in the IFF region arrive there from the direction of Iceland, and are either composed of runoff/meltwater from Iceland itself, or modified polar waters of the East Greenland Current carried to the front by the East Icelandic Current (Jónsson, 2007). Relatively fresh water enters the IFF in the west and subducts along isopycnals as it is advected along the front in the surface layer (Meincke, 1978; Read and Pollard, 1992). Of particular relevance here are the studies by Hallock (1985), who discusses intrusive interleaving of low salinity water at the front and the associated cross front fluxes, and Meincke (1978) who traces the subducting low salinity water at the IFF. Similar low salinity intrusive features are a prominent feature of the glider dataset discussed in this paper. We find a low salinity water mass at the surface of the IFF, which in wintertime subducts along outcropping isopycnals and is found in much modified form south of the IFR crest (cf. Figs. 4.3 - 4.6). The features found south of the front at depth have temperature and salinity characteristics which are clearly traceable to the surface mixed layer north of the IFF (Fig. 4.2). The result is a cross frontal flux of fresh water in the density range of the Subpolar Mode Waters (SPMW) of the Iceland basin. The presence of coherent low salinity layers so far south of the IFF has not been previously reported. Meincke (1978) trace a low salinity water mass from the IFF around the Faroe Islands to the FBC, demonstrating the erosion of the salinity minimum due to mixing around the pathway. However, they find no pathway for the low salinity waters across the IFR from a June-July cruise. Here we show such a pathway exists in wintertime.

The Seaglider observations reported here reveal a more complicated seasonally variable structure in the upper layer, where low salinity waters from north of the ridge appear as mid depth thermohaline intrusions in winter, skewing the quasi-linear TS curve towards a low salinity end member in the density range $27.4 \leq \sigma_\theta \leq 27.65$. We postulate that a combination of mixed layer instabilities initiated by convective surface layer homogenization south of the front, and subduction forced by baroclinic

instability of the IFF force the low salinity intrusive features equatorward across the IFR. These low salinity anomalies (as well as a low oxygen water mass from the Iceland Basin) can be used as tracers of the intermediate circulation over the IFR.

4.2 Measurements

Between November 2006 and November 2009, quarterly deployments (Feb., June., Sept., Nov.) of Seaglider autonomous gliders were made in the region of the Iceland-Faroe Ridge. The resulting data set consists of over 17,000 full-depth hydrographic profiles (more details can be found in Beaird et al. (2013)). The Seaglider is an autonomous 1000 m profiling glider capable of long duration missions (Eriksen et al., 2001). The glider makes sawtooth profiles with a horizontal to vertical aspect ratio of three to one. During these deployments gliders took samples every 20 seconds ($\sim$ 1.5 m vertical resolution) of temperature, conductivity, pressure, dissolved oxygen, two wavelengths of optical backscatter and fluorescence. Deployments were primarily made in the FBC region after which the gliders were directed along the Atlantic side of the IFR towards Iceland. The majority of observations were made on the AIFR, with occasional cross-rdge sections. Deployments were also made north of the Faroe Plateau and in the Faroe-Shetland Channel, but will not be discussed here.

4.3 Results

4.3.1 Water mass structure south of the front

South of the IFR crest the water column is typically composed of warm, salty, Atlantic waters situated above cold, dense water of Nordic Seas/Arctic origin. The structure can be seen from a cross ridge (Fig. 4.3) section (Fig. 4.4). The water masses can be approximately separated by isopycnals (Fig. 4.5). The dense ($\sigma_\theta \geq 27.8\,\mathrm{kg\,m^{-3}}$, Fig. 4.5) layer has 'overflowed' the Iceland-Scotland Ridge across the IFR or through the FBC. In the mean, Atlantic waters flow northwards into the Nordic Seas, and

the polar waters flow equatorward into the Iceland Basin. Locally, the circulation is largely along topographic contours (into and out of the page in Fig. 4.4), and thus not necessarily immediately North/South, but ultimately the result of the circulation is cross-ridge transport.

The Atlantic waters include Modified North Atlantic Water (MNAW) and the Intermediate Water (IW) of the Iceland Basin (Hansen and Østerhus, 2000; van Aken and de Boer, 1995) (Table 4.1, Fig. 4.2). The majority of the Atlantic layer is made up of MNAW, a relatively weakly stratified subpolar Mode Water formed in wintertime in the subpolar gyre from subtropical waters transported by the Gulf Stream/North Atlantic Current (Read and Pollard, 1992; Brambilla and Talley, 2008). IW resides in the permanent pycnocline of the Iceland Basin and is 'biogeochemically defined': having no characteristic temperature or salinity distinction from MNAW, IW is apparent as an oxygen minimum in the range T$= 6 - 8°$C, S$= 35.1 - 35.25$, and $\sigma_\theta = 27.55 - 27.65$kg m^{-3} (van Aken and de Boer, 1995; Sarafanov et al., 2008). In the Iceland Basin proper, IW marks the extent of the deepest wintertime mixing.

On the IFR, IW is found between the MNAW and the overflow water, but its distribution over the ridge is patchy (Ullgren et al., in press). Being the deepest of the Atlantic waters, IW occasionally mixes and interacts with the dense overflow (Ullgren et al., in press). With its a clear geographic source in the Iceland Basin, the distribution of IW traces the advection of water from the south, just as the (seasonal) low salinity thermohaline intrusions discussed in detail in this paper trace advection from north of the IFR. IW, despite its southern origin, has approximately the same density as the unmodified fresh Nordic origin surface waters at the IFF. However, the modified (by mixing with MNAW) fresh thermohaline intrusions south of the IFF are slightly less dense, and settle above the IW in the water column. The layering and distribution of these two water masses of northern and southern origin demonstrate the vertical complexity of the frontal region of the IFR. A simple two layer system, in which a northward flow of warm salty water sits above an overflow

of dense water, appears inappropriate to describe the circulation in wintertime when the low salinity intrusions are present. The interspersed IW and Nordic fresh water masses in the upper water column illustrate the complex three dimensional eddying meridional circulation occurring above the overflow layer.

4.3.2 Fresh Thermohaline Intrusions

The low salinity thermohaline intrusions found seasonally south of the IFF can be distinguished by their anomalous temperature, salinity, and oxygen characteristics. The intrusions have low salinity (and temperature) in the density range $27.4 \leq \sigma_\theta \leq 27.65$, anomalously fresh relative to the North Atlantic waters of the same density, which include both MNAW and IW. Temperature-salinity (TS) curves from profiles which contain intrusions show fresh anomalies relative to the quasi-linear curves connecting Atlantic and overflow waters (Fig. 4.2). The intrusions skew the TS curve in the density range $27.4 \leq \sigma_\theta \leq 27.65$ toward a point with a temperature and salinity of about ≈ 4.5°C and ≈ 34.7. We will refer to the unmodified source of the low salinity features as Low Salinity Frontal Water (LSFW), as described below, and refer to modified LSFW 'intrusions' south of the IFF since the LSFW features intrude between (and mix with) layers of Atlantic water. As well as being fresh, LSFW is also rich in oxygen, having subducted from the surface of the IFF. Away from the front, the intrusions are readily apparent as wedge-like shapes of varying strengths in the TS relation, laying within the triangle defined by the TS points (8.2,35.2), (4.5,34.7), and (3.75,35) (Fig. 4.2). The background TS relation is typically tight and almost linear between 27.4 and 27.65, making low salinity anomalies conspicuous even when their magnitude is quite small. The 'top' of the wedge in TS space is formed by mixing of LSFW with overlying MNAW, producing the gradual reduction of the salinity anomaly with increasing temperature. The 'bottom' of the wedge is formed by the boundary between fresh anomaly and the low oxygen, high salinity, IW situated below the intrusion. The strength of the thermohaline intrusion, defined as

the maximum isopycnal salinity anomaly from the ambient, quasi-linear, TS relation, varies considerably depending on the amount of MNAW which has been mixed into the intrusion (ranging from 0.55 to 0.05 PSU).

The strongest low salinity signals are found at the surface along the IFF and at the northwestern end of the IFR near the Iceland shelf. The low salinity surface water at the IFF can be seen in a glider section north of the IFR crest (Fig. 4.4b, upper 100 m, in the last 25 km). The characteristic properties of the low salinity water at the surface of the IFF are T$\approx$ 4.5°C and S$\approx$ 34.7 (salinity minimum in Fig. 4.4c, example profile 4). The themohaline intrusions found south of the front point towards mixing of this end member with MNAW (Fig. 4.2). We take T$\approx$ 4.5°C and S$\approx$ 34.7 to be the relatively undiluted source of the themohaline intrusions found south of the front.

The provenance of the low salinity surface water is poorly defined. Hansen and Østerhus (2000) in their review discuss the zoo of relatively cold, fresh water masses which converge at the IFF from the direction of Iceland and whose admixture is most commonly called Modified East Icelandic Water (MEIW Table 4.1, Read and Pollard (1992)). MEIW is typically dense enough to be considered part of the overflow from the Nordic Seas into the North Atlantic. Significant variability in the composition of the water mass leads to a generally broad definition of its properties.

We consider the low salinity water masses observed by the gliders to be a part of the MEIW in the sense that it is a modified (by mixing) form of a variety of low salinity waters which are advected east along the IFF from the direction of Iceland. However the intrusions discussed here are not as dense as the MEIW. Slightly warmer and fresher than the North Icelandic Winter water/ Arctic Intermediate water (NI/AI) described by Meincke (1978), the low salinity water mass of interest is likely some mixture of NI/AI and East Icelandic Current water (EIC) (Read and Pollard, 1992) and thus might fit into a relatively warm, fresh category of MEIW (Table 4.1). Allen et al. (1994) describe patches of cold fresh water ($S = 34.4$ and $T = 4$°C) at the northwest end of the IFF in the upper 50 m of the water column. They suggest

the water mass comes from Icelandic fresh water run off and ice melt carried to the front by the East Icelandic Current. It seems likely that this is a constituent of the low salinity water described here. Read and Pollard (1992) also note that in the summer freshwater at the front spread over the top of the Atlantic water to the south. Investigation of the relatively rare SST images collected on clear days often reveals filaments of cold water streaming off the Icelandic shelf into the IFF (not shown) (cf. Perkins et al. (1998)). All the constituent water masses are known to have significant interannual variability (Hansen and Østerhus, 2000), and perhaps a 'typical' definition of MEIW is impractical.

Examples of thermohaline intrusions

Purely for convenience in this paper we describe the source of the thermohaline intrusions discussed below as Low Salinity Frontal Water (LSFW), but argue that this is just one of the constituents of MEIW, and not a 'new' water mass in any sense. The undiluted LSFW is about 0.55 PSU fresher and 3.5°C colder than the MNAW in the same density range, producing a fairly strong isopycnal salinity and temperature anomaly where the two water masses interleave.

The origin of the observed thermohaline intrusions is the LSFW in the surface layer of the IFF, but the features are found considerably deeper to the south. Therefore some vertical as well as horizontal circulation influences the intrusions. The glider section in Figure 4.4 crosses the IFR and IFF, and shows several stages in the evolution of LFSW into the thermohaline intrusions south of the front via subduction and mixing. The initial subduction and formation of the thermohaline intrusions north of the IFR can be seen in Figure 4.4b, beyond 300 km into the section (also see the close up segment in Fig. 4.15). A low salinity tongue extends down from the LSFW at the surface, along the 27.45 isopycnal. LSWF intrudes below the MNAW and mixes with it, creating the typical wedge-like thermohaline intrusion (Fig. 4.2), with the greatest salinity anomaly near the bottom of the feature. The example profiles 4 and

3 in Figure 4.4c show the transition from surface LSFW (profile 4, with surface low salinity) to thermohaline intrusion (profile 3 with the salinity minimum below the MNAW). Figure 4.4a shows the close proximity of the oxygen rich LSFW features and the oxygen depleted IW. IW is seen in varying intensities rising along the 27.5 isopycnal towards the IFF. Several more highly modified thermohaline intrusions are seen further to the south in Figure 4.4b, on both sides of the ridge crest (between 200-300 m depth at ∼200 km along the section).

From the stages of development of the intrusions in Figure 4.4 a few characteristics of the thermohaline intrusions emerge: the intrusions subduct from the surface layer of the IFF to depths of 300 m (and eventually 600-800 m on the Atlantic side of the IFR); they are modified by mixing with MNAW close to the front; and they become significantly thicker (∼300 m) than the LSFW layer at the IFF (∼100 m). It should be noted that advection of the features in this section should not be mistaken as two dimensional. As mentioned above, the mean circulation in the region is along topographic contours (perpendicular to this cross ridge section), and a complicated three dimensional eddying circulation will be responsible for the advection of the features discussed in Figure 4.4 (see, the complex nature of the SST front in Fig. 4.16).

Despite originating north of the IFR crest, the thermohaline intrusions are too light to be part of the dense outflow from the Nordic Seas. They occupy the upper water column, just slightly denser than the majority of the MNAW which enters the Nordic Seas through the gap between Iceland and the Faroe Plateau. In the canonical circulation scheme, the transport of northern waters to the south only occurs in the dense layer. Thus advection of LSFW thermohaline intrusions into the intermediate depths south of the front is a southward flux in the upper water column, differing from the classical circulation scheme in which all upper level waters flow northward.

Two arbitrarily chosen sections demonstrate the characteristics of the modified LSFW intrusions further south of the IFF on the Atlantic slope of the IFR. One section

is from the same time period as the cross-ridge section in Figure 4.4 (Dec. 2007) and the other shows the modified LSFW on the AIFR the following winter (Nov.-Dec. 2008), indicating the persistent winter time fresh water flux from year to year. The example in Figure 4.6 (contemporaneous with Fig. 4.4) displays much diluted fresh thermohaline intrusions on the Atlantic side of the ridge. A clear progression can be seen in the TS relation from the surface LSFW at the IFF (Fig. 4.4c) to the greatly modified LSFW in sections on the AIFR (Fig. 4.6c). The salinity anomaly is much reduced in the features found on the AIFR, but the TS characteristics clearly indicate the anomalous low salinity water is the product of mixing between the LSFW and MNAW. A very similar diluted signal is seen in the section made in 2008 (Fig. 4.7), demonstrating the presence of the water mass in different years. The thermohaline intrusions are seen as deep as 600 m (Fig. 4.6 at profile 1) and up to 400 m thick in these examples. These sections are chosen as several out of numerous examples from a large set of observations of the penetration of LSFW south of the IFR crest in winter.

Statistics of thermohaline intrusions

The two example sections on the Atlantic side of the IFR (Figs. 4.4 and 4.6) show parcels of LSFW are still clearly identifiable, though mixing with MNAW has eroded the maximum salinity anomaly considerably (from ~ 0.55 to ~ 0.1). Due to significant variability in the strength of the salinity anomaly, combined with noisy salinity data, an objective identification routine for LSFW thermohaline intrusions proved elusive. However, the distinctive shape of the intrusion TS relation, with the trajectory of the TS curve towards LSFW and the intensification of the salinity anomaly at the bottom of the intrusion, makes LSFW influence readily identifiable by eye. Profiles on the AIFR were manually sorted into a group that contained LSFW thermohaline intrusions and a group that did not. Over the ridge 1972 profiles were found to have LSFW influence, compared with 8131 without. Figure 4.8 demonstrates the

difference in TS space between profiles with and without LSFW intrusions. Figure 4.8 displays a kernel density estimate of AIFR TS profiles with (right) and without (left) LSFW intrusions. Contours correspond to the smallest region which contains the appropriate probability mass, meaning the .95 contour is the smallest contour which can be drawn containing 95% of all TS pairs, the 0.1 contour is the smallest curve which contains 10% of all pairs, etc. The darkest colors indicate the highest density regions. Several differences between the TS groups are apparent right away. The most obvious is the skewness towards a point at T$\approx$ 4.5°C and S$\approx$ 34.7, the definition of LSFW. This is obviously the signal by which the groups were classified. Also, the seasonal thermocline is present in the intrusion free group and absent in the intrusion group. This is the first hint that the LSFW thermohaline intrusions occur in winter.

It is important to note that no source of low salinity water in this density range exists south of the IFR. This is further evidence, along with the similarity in TS characteristics to LSFW and the observed stages of subduction in Figure 4.4, that the thermohaline intrusions observed south of the front represent a flux from the north. Ullgren et al. (in press) discuss a low salinity intermediate water which interacts with the FBC overflow. This water mass appears to be a mixture of IW and the Labrador Sea Water that sits below the permanent pycnocline in the Iceland Basin. The low salinity water described in that paper (State III type profiles, cf. Fig 12 in Ullgren et al. (in press)) is denser than and distinct from what we report here.

4.3.3 Seasonality and Geographic distribution of intrusions

Figure 4.9 depicts both the seasonal (right) and geographic (left) distribution of the identified LSFW intrusions (the groups in Fig. 4.8). Profiles containing LSFW thermohaline intrusions are indicated in red, the intrusion free group in black. Two significant patterns in the distribution of thermohaline intrusions are evident. The first significant finding is that profiles with LSFW influence are almost completely

restricted to the AIFR west of the FBC outflow region, where the outflow region is defined as the area south and west of 62°N, 10°W. This pattern implies advection of LSFW thermohaline intrusions across the IFR rather than through the Faroe-Shetland and Faroe Bank Channels. Low salinity waters from the IFF do arrive in the Iceland Basin Via the Faroe Shetland Channel to Faroe Bank Channel (FSC-FBC) pathway but these waters are heavily modified by mixing (Meincke, 1978; Ullgren et al., in press) and lose the sharp intrusive character of the features identified south of the IFR crest in Figure 4.8, right. The FSC-FBC pathway is independent of the one reported in this paper. This provides evidence that the LSFW intrusive features cross the IFR crest rather than transit though the Faroese Channels.

The second new observation is that nearly all the identified intrusions are found between November and February (Fig. 4.9, right). The seasonality perhaps obscures these features from the observational record on the IFR, with its bias towards summer months. In December and January low salinity intrusions are found in $\sim 60\%$ of profiles made on the AIFR (Fig. 4.9, right, solid lines). When the FBC outflow region is excluded from the census (LSFW intrusions are not found there anyway), 80% of profiles on the AIFR contain some evidence of LSFW influence in December and January, and 40% in November and February (Fig. 4.9, right, dashed lines). Themohaline intrusions are almost completely absent between March and October. The seasonal pattern repeats itself in each of the three years of the study. Figure 4.10 shows the total number of profiles on the AIFR in 30 day segments and the number of profiles with LSFW intrusions. There is a spike in observations of intrusions centered on each of the three Januarys, and nothing the rest of the year.

Seasonal histograms of all TS profiles from the AIFR outside the FBC outflow region are shown in Figure 4.11. Again the intrusions are apparent primarily in early winter. Similar TS histograms for the FBC outflow region alone (Fig. 4.12) shows that no low salinity intrusive features are found in that region. The FBC TS curves suggest that there are no significant seasonal changes in either the FBC overflow or the

upper layer Atlantic water (aside from the growth/decay of the seasonal thermocline). This further supports the conjecture of seasonal injection of LSFW across the IFR, rejecting the possibility that the features arrive via the FBC or are the result of seasonal changes in the Atlantic waters, changes which would also be apparent in the upper layer of the FBC.

The seasonal cycle of upper ocean properties and mean isopycnal salinity anomaly (in the range of the intrusions) on the AIFR is displayed in Figure 4.13. Only profiles made outside the FBC outflow region are included. Following the convention of Figure 4.9, red markers indicate profiles with identified LSFW intrusions and black are profiles without. The mean isopycnal salinity anomaly is calculated as the mean over the density range $27.4 \leq \sigma_\theta \leq 27.65$ of the isopycnal salinity anomaly from a straight line in TS space between (6.16, 35.15) and (8.94, 35.28), the approximate background Atlantic TS curve. This is a representation of the LSFW intrusions, though it is an imperfect one as some intrusions do not extend over the full density range, impacting the mean. A strong seasonal cycle of mixed layer density, depth, and convection resistance is apparent. Wintertime mixing is intense in the region south of the IFF, with mixed layers reaching $\geq$600 m (Fig. 4.13, see also Brambilla and Talley (2008)). Figure 4.13 shows that the appearance of LSFW intrusions on the AIFR (red dots, and more negative isopycnal salinity anomalies) in late November coincides with the deepening and increased density of the mixed layer and a reduction of the 500 m convection resistance.

4.4 Discussion

The preceding observations establish the existence of a seasonal low salinity flux across the IFR in winter time. The glider data reported here have the distinct advantage of winter time coverage, allowing this previously unresolved process to be observed. The low salinity intrusions represent a flux of freshwater towards the North Atlantic in the upper water column in winter. This is contrary to the traditional picture of the

upper level flow of Atlantic water towards the Nordic Seas. The flux acts to make the front more diffuse in the winter, creating an intermediate water mass with relatively low salinity that occupies the space over the IFR. In this section possible mechanisms forcing the frontal subduction will be discussed, and a rough order of magnitude calculation will be made showing that the flux of LSFW is a locally important cross frontal mechanism for heat and salt exchange.

4.4.1 Possible mechanisms of subduction

The glider observations show that south of the front the LSFW subducts along isopycnals forming thermohaline intrusions. The subduction at the front implies ageostrophic vertical velocities at the IFF. Vertical motions at the front have been shown to occur by Allen and Smeed (1996), who used high resolution SeaSoar surveys and the omega equation to diagnose vertical velocity in the meanders and eddies of the IFF. That study revealed large vertical velocities up to 100 m d^{-1} in the isopycnal range $\sigma_\theta = 27.4 - 27.6$, the level of the LSFW intrusions. This frontal ageostrophic circulation is in all likelihood partially responsible for the subduction of LSFW seen by the gliders.

The lack of synoptic data and measurements of instantaneous velocity from the glider surveys make unequivocal determination of the dynamics at work impossible. Cross-track absolute geostrophic velocity is available, but the expectation is that ageostrophic circulation plays an important role in transporting and subducting the LSFW intrusions. In order to solve the omega equation, synoptic along and across-front density information is needed, but only four isolated cross-front sections were made. However, we can describe plausible mechanisms responsible for the observed circulation and seasonality based on previous studies of cross frontal exchanges.

The literature on frontal dynamics is extensive. The importance of submesoscale, unbalanced motion in transferring properties both horizontally and vertically has received substantial attention. These type of motions, involving large vertical velocities

and small scale filamentous structure, are active in flows with large Rossby numbers ($O(1)$). Meanders and eddies in the IFR region have the requisite large relative vorticity ($\sim 0.8f$, Allen and Smeed (1996)) and Rossby numbers, and SST images reveal ubiquitous cross frontal filamentation (Figs. 4.1 and 4.16) (Scott and McDowall, 1990; Niiler, 1992) .

The Iceland-Faroe Front is known to be baroclinicly unstable with frequent breaking meanders producing a vigorous eddy field (Hansen and Meincke, 1979; Allen et al., 1994; Willebrand and Meincke, 1980; Rossby et al., 2009). Potential vorticity (PV) on isopycnals changes substantially across the front, as the thick layer of Atlantic water is squeezed over the shallow IFR (Allen and Smeed, 1996). Change in PV across fronts of opposite sign in the upper and lower layers is a necessary condition for the growth of baroclinic instabilities (Gill, 1982).

Subduction at upper ocean fronts can be driven in different ways, through both external atmospheric forcing (buoyancy or wind stress) and internal frontal instability. Externally, a down front windstress will produce Ekman transport which drives dense water over light, causing turbulent mixing and ageostrophic circulation (Thomas and Lee, 2005). Internally, mesoscale eddy induced shear and strain disturb geostrophic balance and generate ageostrophic vertical motions to restore that balance (Hoskins et al., 1978; Pollard and Regier, 1992). Confluent flow in unstable and meandering fronts leads to local frontogenesis and ageostrophic vertical circulation (Hoskins et al., 1978). This ageostrophic circulation due to internal instability has been shown to cause subduction of waters from the cold side of the front under waters of the warm side (Spall, 1995). Detailed observations of the process at work at the northern flank of the Gulf Stream by Thomas and Joyce (2010) show the production of 'cusp-like' thermohaline intrusions with characteristics remarkably similar to those observed here.

A second set of instabilities may be relevant to subduction at the IFF. It is possible that Mixed Layer Instabilities (MLI, Boccaletti et al. (2007)) play a role in this winter

time cross-frontal exchange. MLIs are a class of instability which occur in regions with lateral inhomogeneities coupled with vertically well mixed layers. A region with horizontal density gradients (e.g., a front) that becomes vertically well mixed by strong atmospheric forcing will undergo adjustment where the vertical isopycnals slump due to gravity. The slumping is arrested by the establishment of geostrophic balance. Boccaletti et al. (2007) show that the adjusted state is susceptible to submesoscale baroclinic instability. Those authors describe the MLI in terms of restratification, which is essentially a lateral exchange of density (and other properties), showing that the submesoscale baroclinic instability does significantly more to restratify the fluid than the initial gravitational slumping of the vertical isopycnals. One of the primary differences between MLI and traditional baroclinic instability is in scale: MLIs only impact the upper (well mixed) portion of the water column, while the baroclinic instability of the IFF, say, will extend throughout the depth of the front. Additionally, MLIs have faster timescales than baroclinic instability. At the IFF in winter the conditions for MLI are met, with strong horizontal density gradients and deep wind driven mixed layers (Figs. 4.14 and 4.15). In the IFF case, the MLI would be occurring on top of the steeply sloping front, as opposed to the gentle sloped thermocline case described in Boccaletti et al. (2007).

It seems very likely that the seasonal nature of the LSFW flux is related to the deepening of the surface mixed layer. South of the front the mixed layer reaches down to the densities of the IW in the Iceland basin, up to 600 m in places (Fig. 4.13). North of the IFF the mixed layer is much shallower, but is still 75 m deep. In the winter, the strong potential vorticity barrier of the seasonal thermocline is erased (Fig. 4.14). There is a strong PV gradient on the isopycnals in question (27.4-27.6) in the summer, but in winter the PV on the intermediate isopycnals is low even as the front is crossed. There is still a salinity gradient on the isopycnals, but in winter the surface expression of the IFF is associated with vertical isopycnals and a transition between the very deep mixed layers to the south, and the relatively shallow mixed

layer to the north.

The deep winter mixed layers are an indiction of the vigorous atmospheric forcing present in the IFR region, which lies in the path of the Atlantic storm track. As mentioned earlier, if the strong winds associated with passing wintertime storms blow down-front, a cross frontal Ekman transport could lead to mixing of the LSFW onto the Atlantic side of the IFF. It appears likely that the flux of low salinity water is driven by a combination of ageostrophic subduction due to instability of the IFF, as well as some contribution of MLIs at the surface.

4.4.2 Basic heat and salt flux estimates

A rough estimate of the heat and salt flux due to the subducting LSFW can be made by using vertical velocity data from Allen and Smeed (1996). As mentioned above, meandering at fronts forces vertical velocities which subduct properties along isopycnals (Pollard and Regier, 1992; Spall, 1995; Thomas and Joyce, 2010). Allen and Smeed (1996) calculated ageostrophic vertical velocities of 25-100 m day^{-1} at the IFF using the three dimensional omega equation. Taking these velocities as the vertical component of along-isopycnal flow, and assuming the mean isopycnal slope of the IFF to be 0.01 (it is steeper in the west, and shallower in the east, Read and Pollard (1992)), the ageostrophic cross-front velocities are roughly in the range 0.03-0.12 m s^{-1}. We assume these ageostrophic velocities are responsible for the initial subduction and cross-frontal flux of LSFW. Inspection of a close view of the front in Figure 4.15 suggests the thickness of the initial subducting LSFW (sloping low salinity tongue at approximately 125 m depth and 65 km) of about 40 m. We find the resulting intrusions all along the Atlantic side of the IFR (Fig. 4.9), so we make the assumption that intrusive features occur everywhere along the ∼300 km of the IFF. Heat and salt flux estimates can then be made by multiplying the width, thickness, speed, heat or salt anomaly together and dividing by the area of the IFR gap (∼300 km wide, by ∼500 m deep). The unmodified LSFW isopycnal salinity anomaly is ∼-0.55 psu

and the isopycnal temperature anomaly ∼-3.5°C (e.g. Fig. 4.2). Approximating 1 psu $\approx 1^{\circ}/_{\circ\circ} = 1$ g per kg of water, and using a reference density $\rho_o = 1027.45\,\mathrm{kg\ m^{-3}}$ and the specific heat of seawater $C_p = 3850$ J/(kg°C), rough estimates of the heat and salt flux due to subducting LSFW in winter can be made. The resulting winter time cross-IFF salt flux due to LSFW is in the range -1.35 to -5.4 g/(m^{2}s). The associated heat flux is -3.3×10^4 to -13.3×10^4 W m^{-2}. These values can be compared with previous estimates of cross IFF fluxes. The LSFW fluxes are seasonal, and should be adjusted to annual averages to compare with other flux estimates. Using Figure 4.9 as a proxy for the fraction of the year when LSFW is being subducted at the front suggests the process is active 20% of the time. Therefore the annual average values for salt and heat flux, respectively, become -0.3 to -1.1 g/(m^{2}s) and -0.65×10^4 to -2.65×10^4 W m^{-2}.

The estimates of heat and salt fluxes due to subduction of LSFW are rough, and made with a number of assumptions, the most tenuous of which is the use of Allen and Smeed (1996) omega equation results to obtain ageostrophic cross-IFF velocities. However the numerous observations of strong ageostropic circulation at unstable ocean fronts suggests that the assumption is not unreasonable. The importance of the seasonal LSFW flux can be assessed by comparing the rough estimates above with previously published estimates of flux by mesoscale and submesoscale motions at the IFF. Three studies present such estimates: Willebrand and Meincke (1980), Hallock (1985) and Allen et al. (1994). Willebrand and Meincke (1980) find a northward eddy heat flux of 12×10^4 W m^{-2} from a near bottom current meter moored just north of the IFR crest. Those authors claim the eddy heat flux is of the same order of magnitude as the mean southward advection of NSDW across the ridge, and as the heat loss from the Norwegian Sea due to the advection of low salinity water investigated by Meincke (1978) (although no such calculation is explicitly presented in Meincke (1978), despite the overlapping author of the two papers). Hallock (1985) calculates heat and salt transport across the front by mixing in intrusive interleaving features at the IFF. He

uses the method of Joyce (1977), which balances vertical diffusion across intrusions (using an assumed vertical diffusivity) with horizontal cross front advection, to find salt and heat fluxes of 1.58 g/(m^{2}s) and 5.16×10^4 W m^{-2}. The final estimate of eddy heat and salt flux comes from Allen et al. (1994). They calculate the mean salt and heat content of eddies near the IFF and estimate an eddy generation rate to get fluxes. The resulting flux estimates are 3.5 g/(m^{2}s) and 8.0×10^4 W m^{-2} for salt and heat.

All these flux estimates are of the same order of magnitude. Our range of estimates are also of the same order. The seasonal values are right within the range of the three previous heat flux estimates and the two salinity estimates. The annual mean fluxes reported here are smaller (particularly the heat flux) than the range in the literature. The low end of our annual estimates are roughly 10% of the values from the literature, and 50-100% on the high end. Still, it appears that subduction and cross frontal exchange of LSFW is a significant local contribution to cross frontal flux in winter time. Willebrand and Meincke (1980) notes that these eddy fluxes are locally important to the IFF region, but at least in the case of heat, are a small contribution to the overall budget of the Norwegian Sea. Rossby and Flagg (2012) estimate the total heat and salt inflow to the Nordic Seas to be 171 TW and 1.45×10^8 kg s^{-1}. Hansen et al. (2003) estimate higher values of 247 TW and 2.43×10^8 kg s^{-1} and Østerhus et al. (2005) find 313 TW and 3.03×10^8 kg s^{-1}. Assuming a width of 300 km and depth of 500 m for the IFR, the total heat and salt transport due to the subducting LSFW is 0.97-3.97 TW and 0.45-1.8$\times10^5$ kg s^{-1}. The mescoscale and submesoscale fluxes at the front appear not to be comparable to the large scale advection of Atlantic waters into the Nordic Seas, but may play a role in setting local conditions. For example, Hansen et al. (2003) note decrease in long-term average salinity (0.02-0.04) and temperature (0.25-0.5 °C) of the MNAW core measured at the Faroe Bank (south of the IFR) and at 6°W, north of the Faroes. This cooling and freshening could be a result of mixing of MNAW and LSFW thermohaline intrusions.

4.5 Conclusions

Seaglider surveys reveal a seasonal flux of low salinity mesoscale features southward across the IFR crest in wintertime. The anomalously fresh water subducts from the surface mixed layer above the Iceland-Faroe Front forming thermohaline intrusions to the south. The subducting fresh water mixes with the Atlantic waters south of the front, forming tall, bottom intensified mesoscale features recognizable in TS space as low isopycnal temperatures and salinities. The features are only found between November and February on the IFR outside the FBC outflow region. The flux initiates after the onset of deep winter mixing of the surface layer. In December and January, 80% of profiles contain thermohaline intrusions, 40% of profiles in November and February do. Almost no intrusions are detected outside those four months. The thermohaline intrusions are found in each of the three winters during the glider field campaign (2006-2009).

We speculate that subduction of the low salinity water at the front is driven by ageostrophic motion associated with instabilities of the IFF, as well as mixed layer instabilities at the surface front. The erasure of the strong potential vorticity barrier of the seasonal thermocline by winter time mixing likely results in the seasonality of the signal. Rough calculations of the annual average heat and salt fluxes produced by the features are -0.65$\times 10^4$ to -2.65$\times 10^4$ W m^{-2}and -0.3 to -1.1 g/(m^{2}s). These values are slightly smaller than previous flux estimates due to mesoscale and submesoscale variability at the IFF (Willebrand and Meincke, 1980; Hallock, 1985; Allen et al., 1994). Seasonally, the fluxes are the same size as the previous estimates. This suggests that at least locally, the seasonal subduction of the low salinity surface water mass is an important contribution to cross frontal exchange.

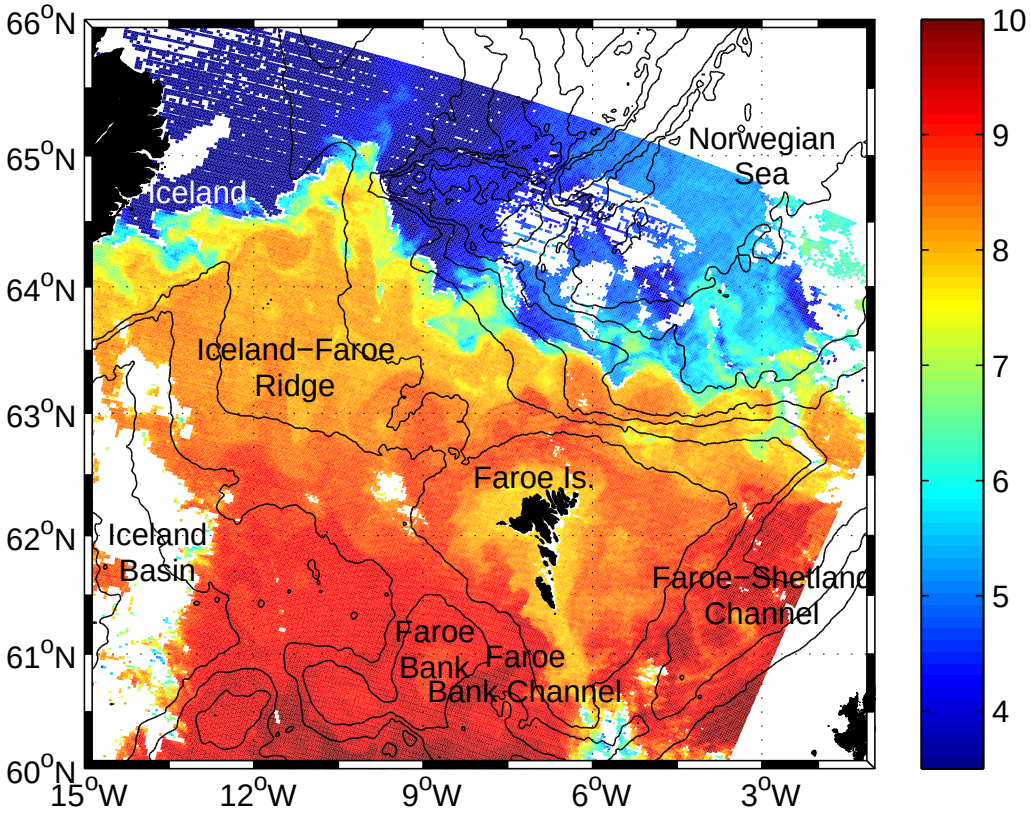

Figure 4.1: A MODIS sea surface temperature image of the Iceland-Faroe Ridge region on 14 May 2009. The Iceland Faroe Front and associated meanders and eddies are clearly visible as warm Atlantic water crosses into the Norwegian Sea. Geographic features are labeled. Bathymetric contours are shown every 500 m.

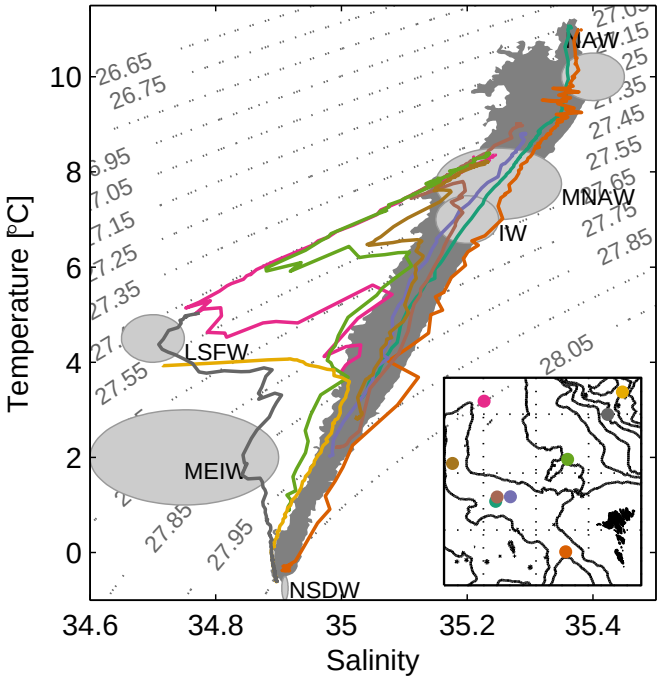

Figure 4.2: Some example TS profiles from around the IFR showing the variable influence of low salinity intermediate waters from north of the IFR crest. Locations of the profiles are shown in matching colored dots in inset map. Typical ranges of some water mass properties are shown in light gray ellipses. 95% of all TS points from the AIFR fall within the dark gray contour shown in the background.

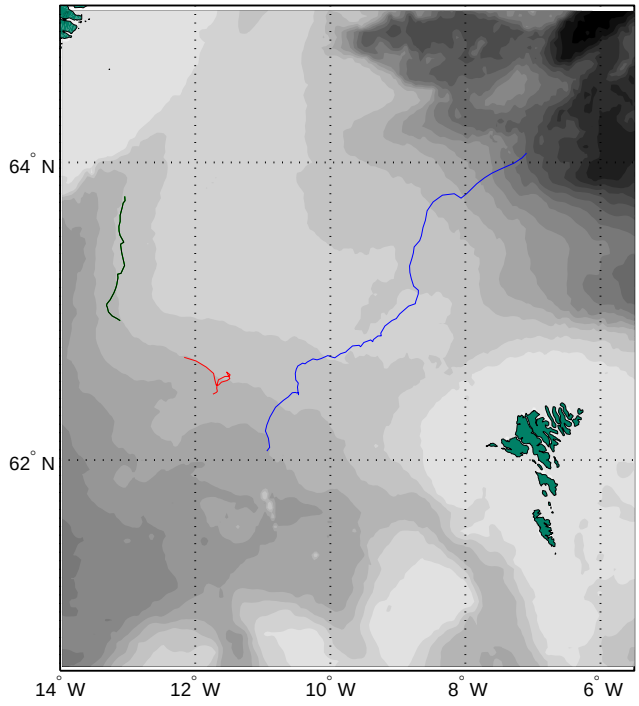

Figure 4.3: Glider tracks from the three example sections shown in Figures 4.4 (blue), 4.6 (red), and 4.7 (green).

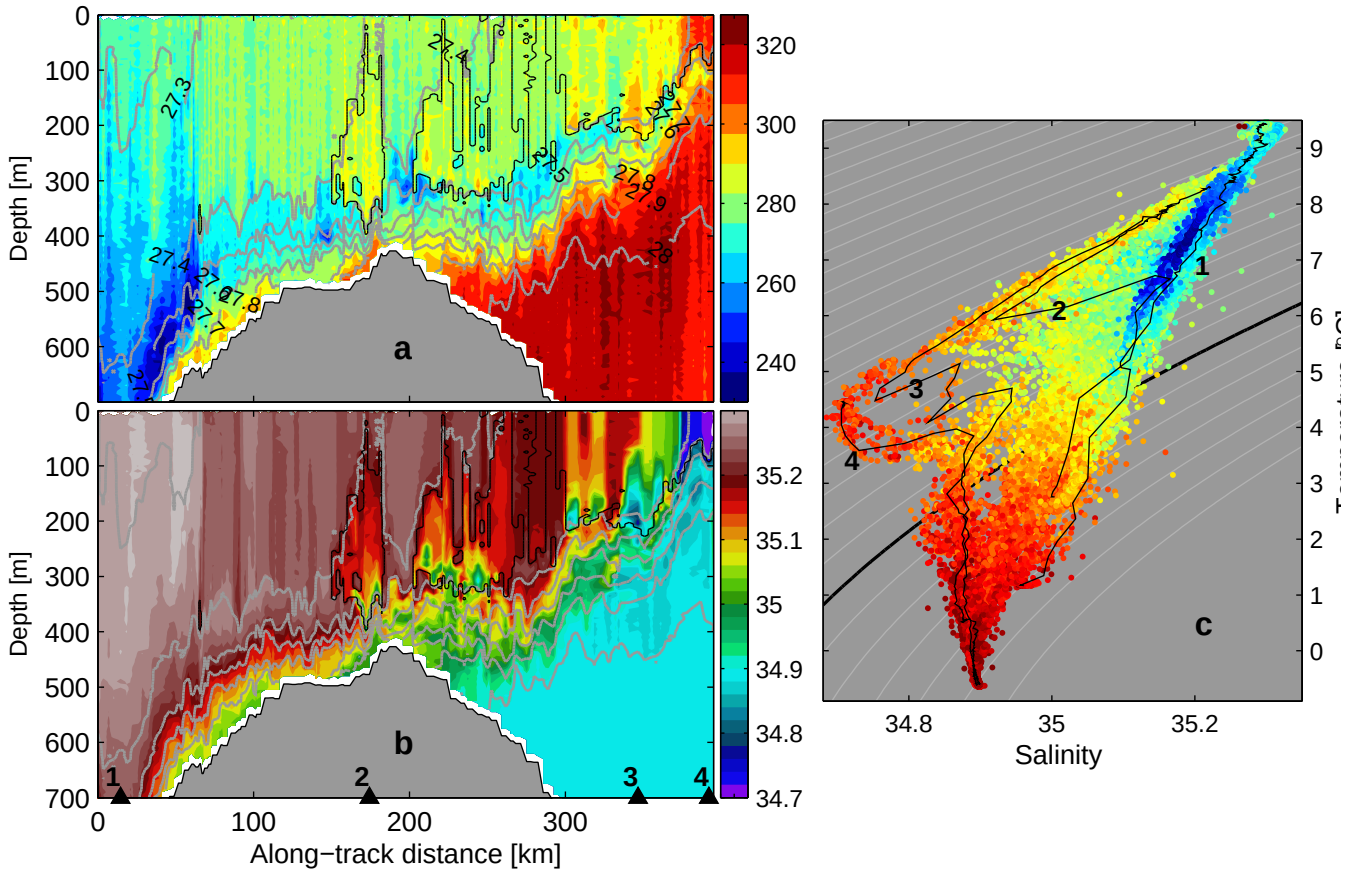

Figure 4.4: (a) Oxygen concentration (μmol kg^{-1}) on a Seaglider section across the IFR and IFF (blue track in Figure 4.3), 2-19 Dec. 2007. (b) salinity along the section. Isopycnals are contoured in gray. (c) Temperature-Salinity relation for the section, with color showing oxygen concentration (same units and scale as (a)). Example profiles are indicated in black, corresponding to the triangles in (b).

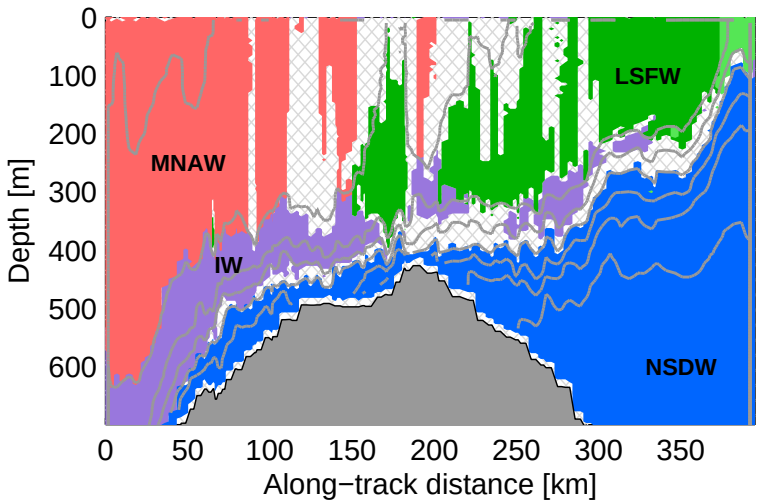

Figure 4.5: Schematic distribution of the the water masses discussed in the text, labeled and approximately delineated on the section in Figure 4.4. Cross hatching indicates regions where water masses are mixed to a degree to not be properly represented by a single label. Gray contours show selected isopycnals. Water masses include Modified North Atlantic Water (pink, MNAW), Iceland Basin Intermediate Water (purple, IW), the Low Salinity Frontal Water and associated thermohaline intrusions discussed in this paper (green, LSFW), and Norwegian Sea Deep Water and overflow water (blue, NSDW). We show the overflow on the Atlantic side of the IFR in blue even though it contains NSDW as well as other waters.

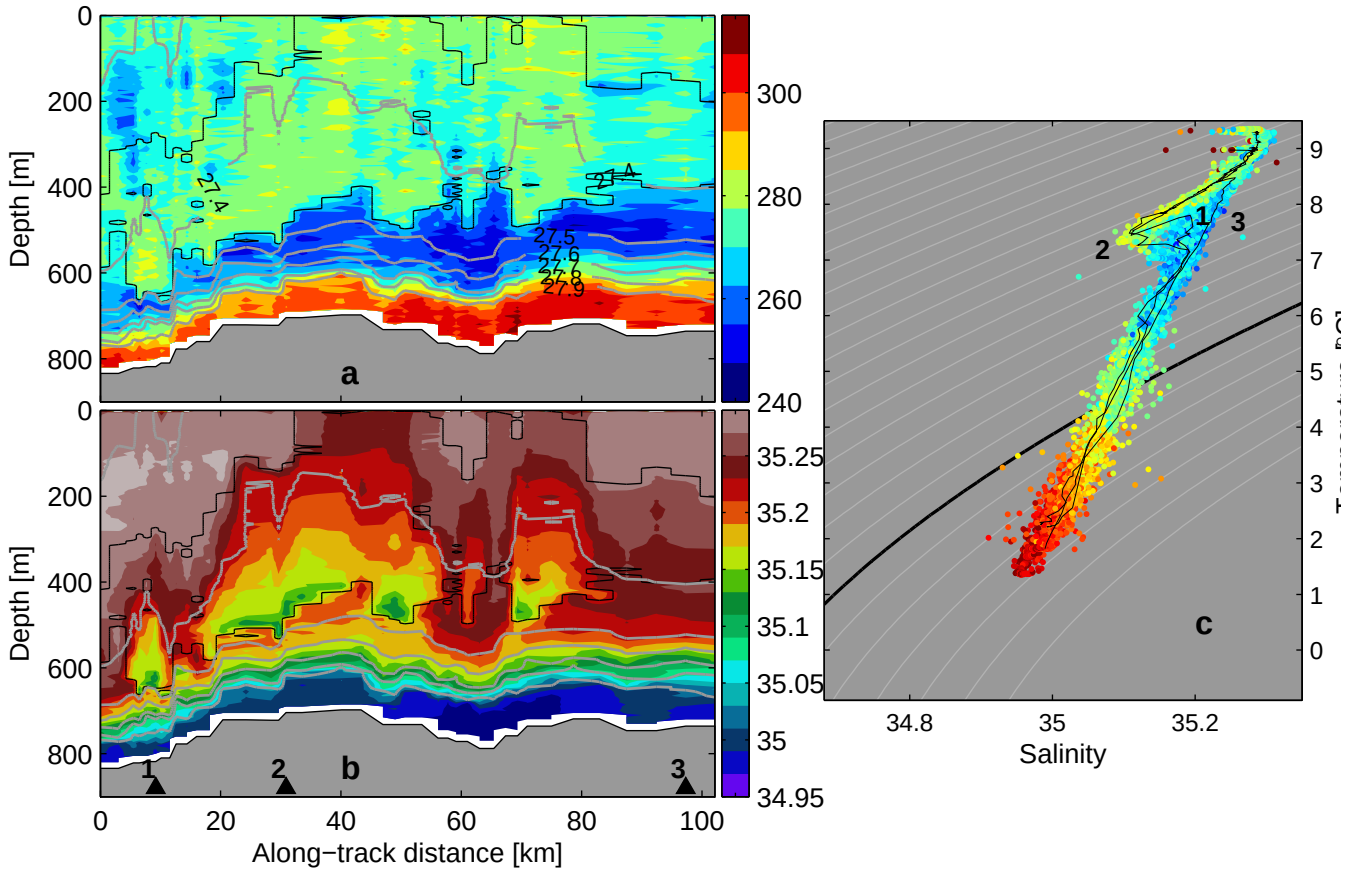

Figure 4.6: (a) Oxygen concentration (μmol kg^{-1}) on a glider section from the AIFR (red track in Figure 4.3), 15-21 Dec. 2007. (b) salinity. Black contour outlines the LSFW. σ_θ contoured in gray on the interval [27.3 : .1 : 28]. (c) Temperature-Salinity relation for the section, with color showing oxygen concentration (same units and scale as (a)). Example profiles are indicated in black, corresponding to the triangles in (b).

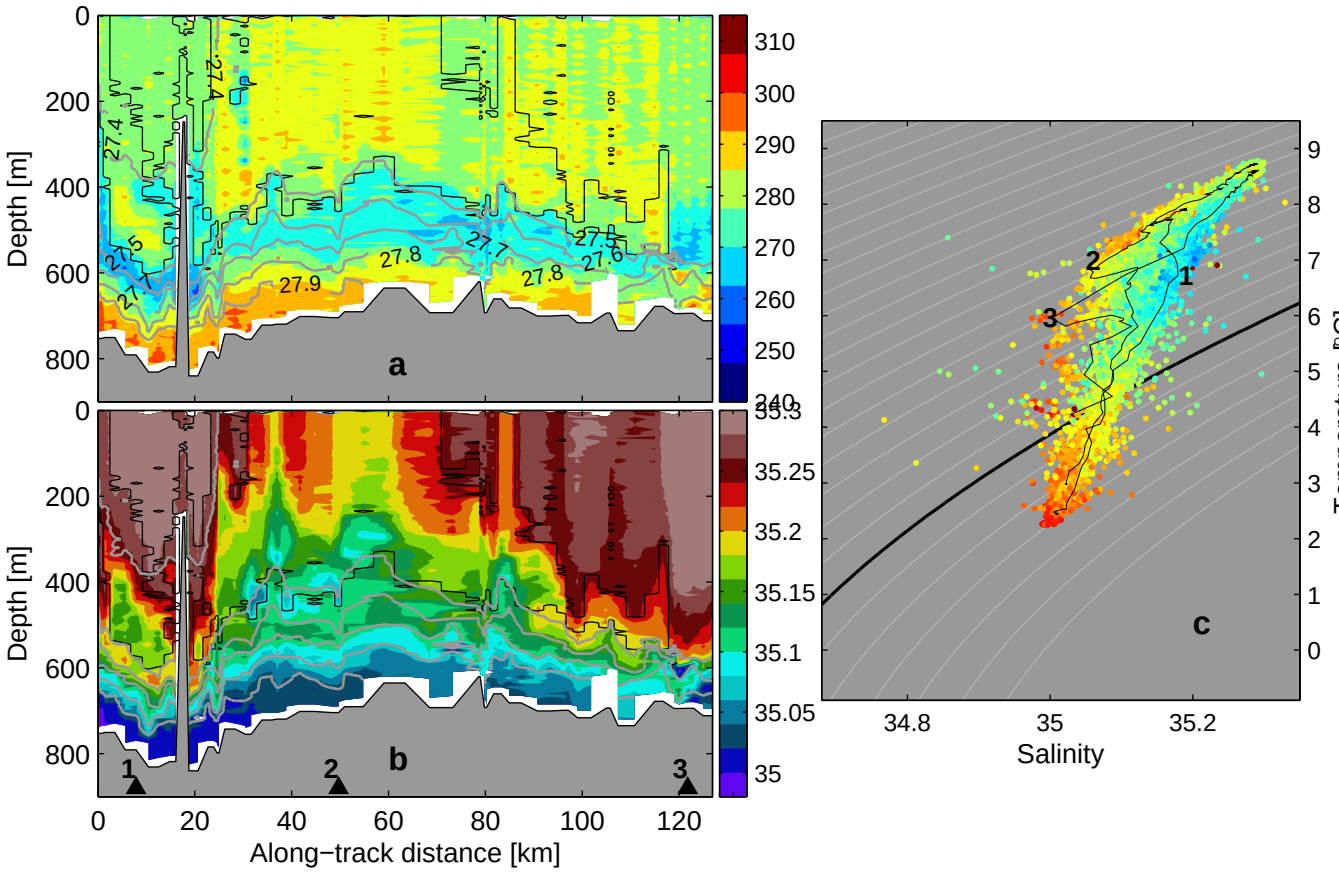

Figure 4.7: (a) Oxygen concentration (μmol kg^{-1}) on a glider section from the AIFR (black track in Figure 4.3), 25 Nov. -2 Dec 2008. (b) salinity. Black contour outlines the LSFW. σ_θ contoured in gray on the interval [27.3 : .1 : 28]. (c) Temperature-Salinity relation for the section, with color showing oxygen concentration (same units and scale as (a)). Example profiles are indicated in black, corresponding to the triangles in (b).

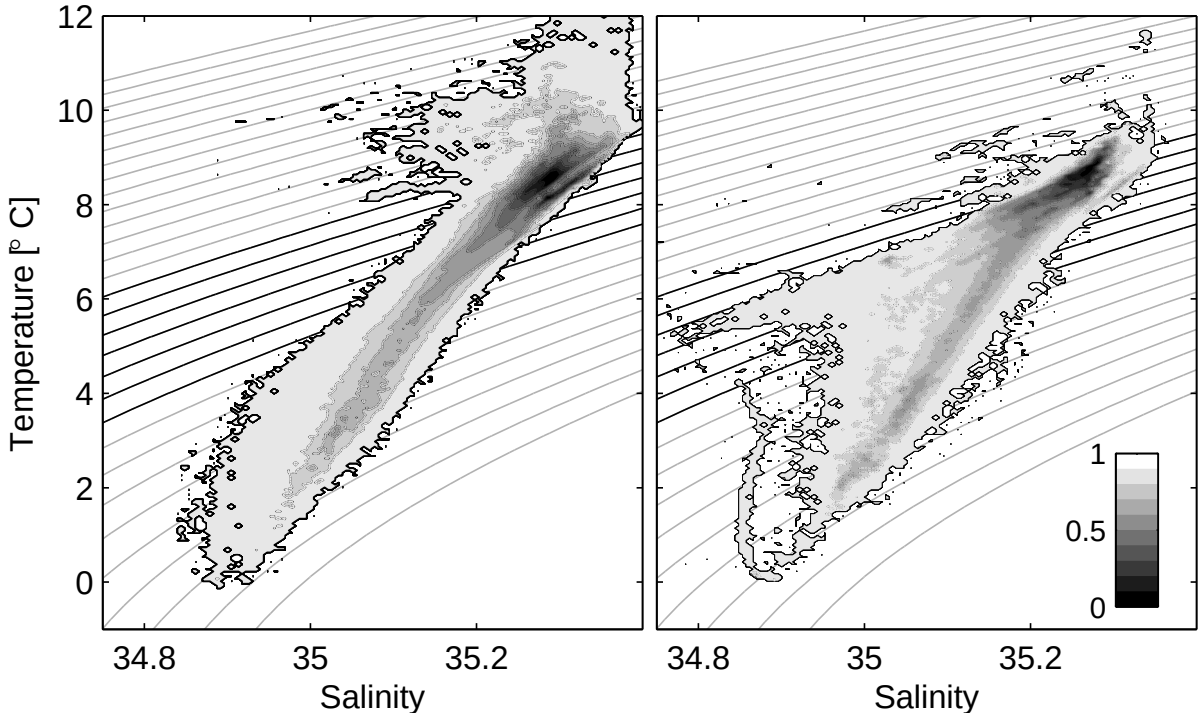

Figure 4.8: Temperature-Salinity kernel density estimates for profiles determined to contain a LSFW thermohaline intrusion (right) and those without an intrusion (left). The contours correspond to the smallest curve that can be drawn to contain the corresponding fraction of TS pairs (i.e. the .95 contour is the smallest area which contains 95% of points, similarly .1 contour is the smallest region containing 10% of all points). The contour interval is 0.1, corresponding to 10% levels. Potential density is contoured in the background with the isopycnal range of interest in bold.

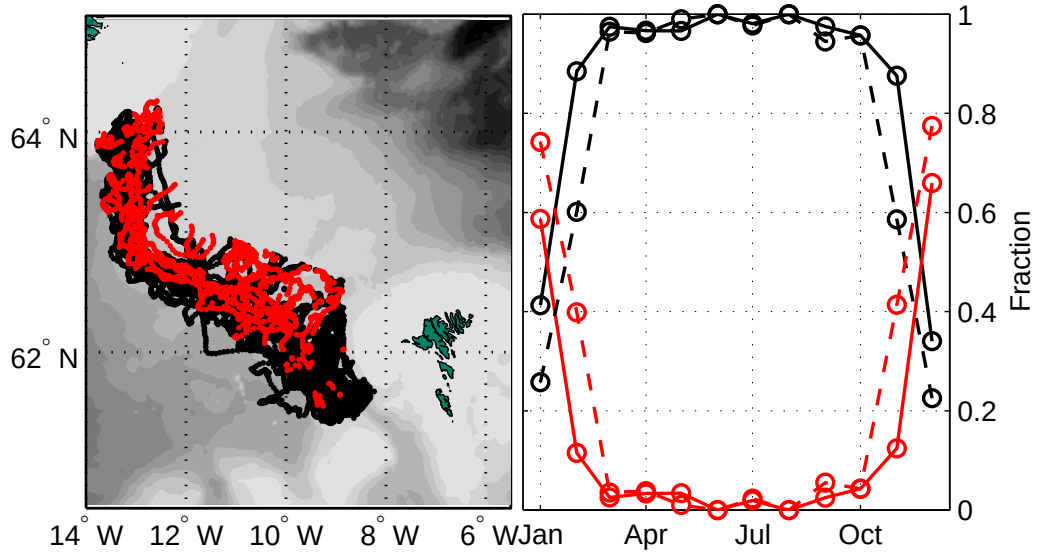

Figure 4.9: Left: geographic distribution of profiles with identified LSFW thermohaline intrusions in the isopycnal range $27.4 \leq \sigma_\theta \leq 27.65$, red points show profiles with intrusions, black profiles without. Right: Seasonal distribution of the fraction of profiles with intrusions (red) and without (black). Solid lines show fractions with the FBC region included, dashed lines show the AIFR excluding the FBC.

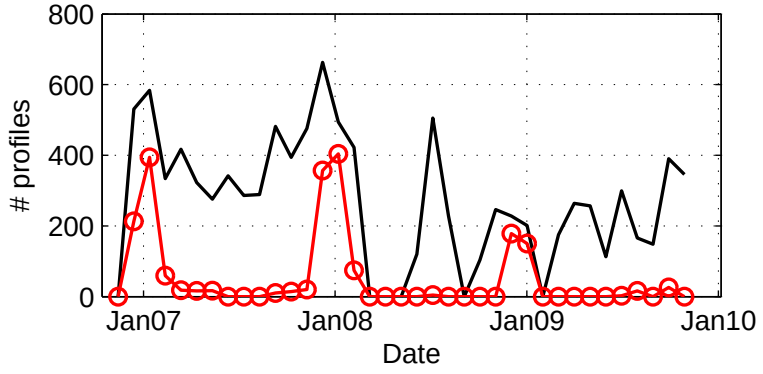

Figure 4.10: The total number of profiles on the AIFR (including FBC) in 30 day bins (black) and the number of profiles with identified thermohaline intrusions (red). The full period of the field study is shown.

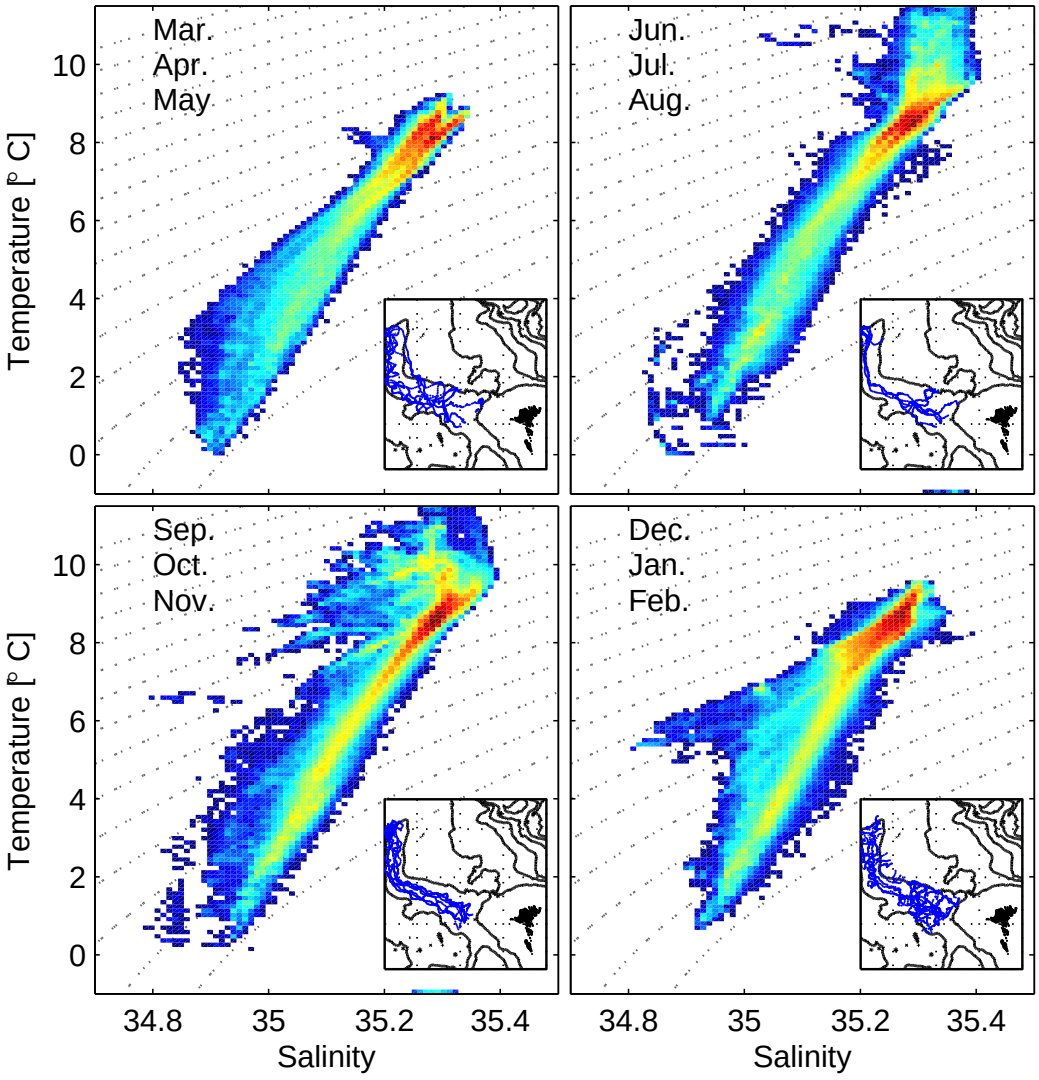

Figure 4.11: Histogram of all TS profiles from the Atlantic Flank of the IFR, excluding the FBC outflow region. Profiles are broken into three month seasons. The locations of profiles are shown as blue dots in the inset maps.

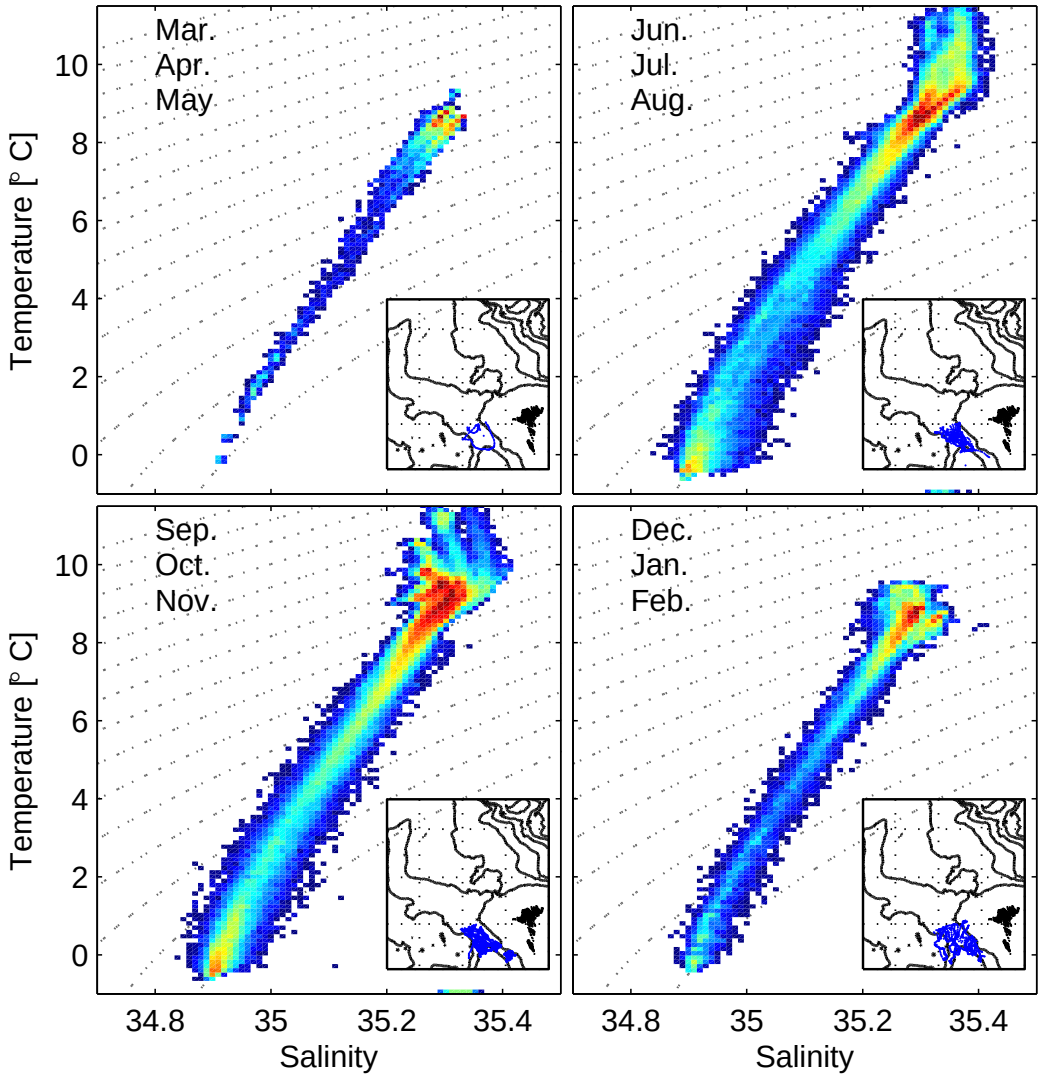

Figure 4.12: Histogram of all TS profiles from the FBC outflow region. Profiles are broken into three month seasons. The locations of profiles are shown as blue dots in the inset maps.

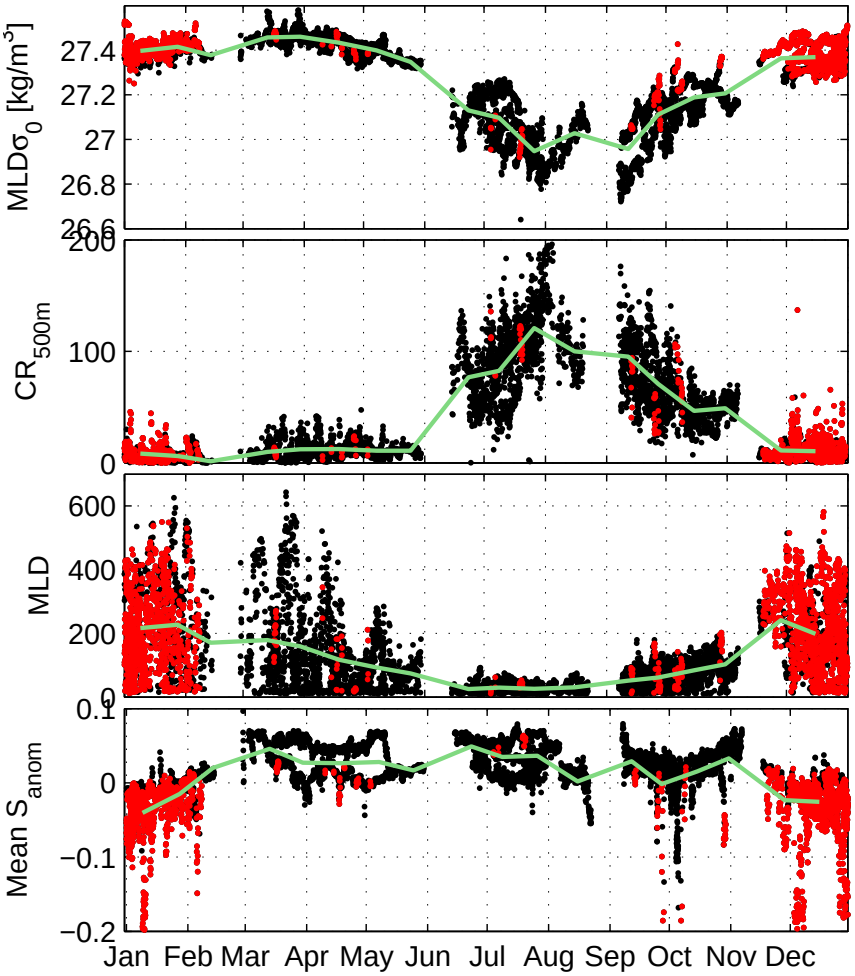

Figure 4.13: Seasonal cycle of properties on the AIFR (excluding the FBC region), from the top: mixed layer density, Convection resistance to 500 m, mixed layer depth, and mean salinity anomaly over the density range $27.4 \leq \sigma_\theta \leq 27.65$. Red dots show profiles with LSFW influence, black are intrusion free. Green curves are 20 day running means of each property.

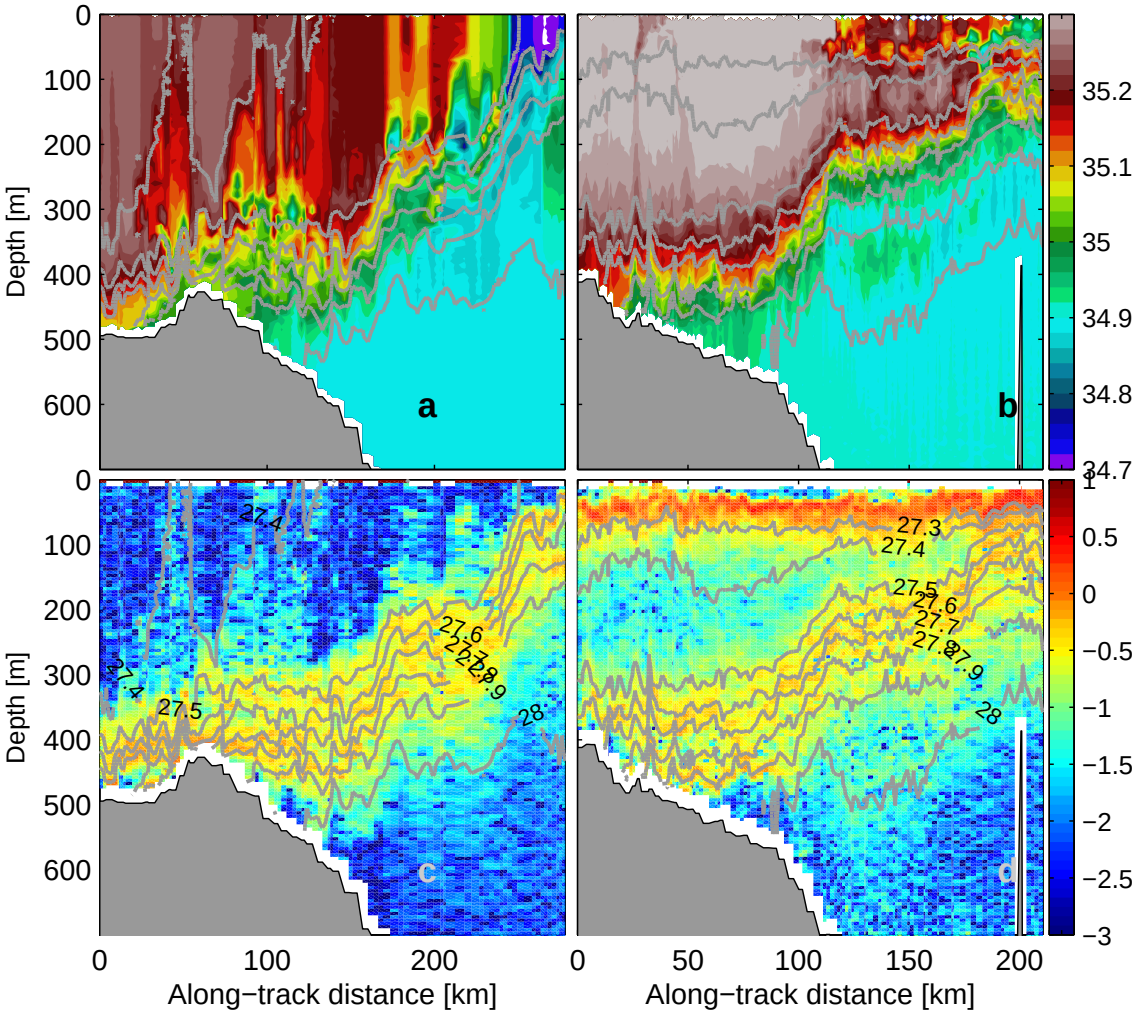

Figure 4.14: Salinity (top row) and $\log_{10}$ of planetary Potential Vorticity $[10^{-9}(\mathrm{m\,s})^{-1}]$ at the IFF in winter (left column) and summer (right column) sections.

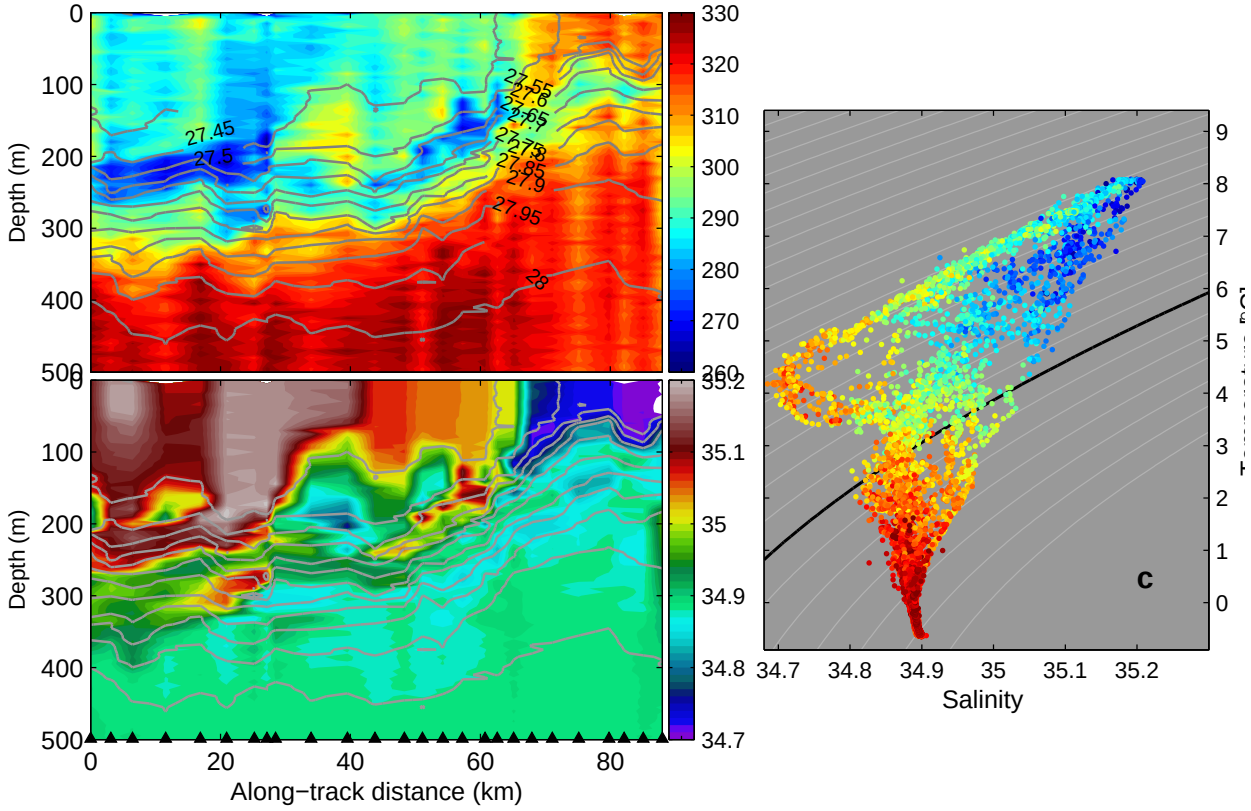

Figure 4.15: Close up of subduction of LSFW at the IFF from the last 85 km of the section in Figure 4.4. Layout and units are the same as Fig. 4.4. Upward pointing triangle indicate the location of profiles. Density is contoured in 0.05 kg m^{-3} steps. Only the upper 500 m are shown in the contour sections, whereas the TS-oxygen scatter contains the full 1000 m profile data.

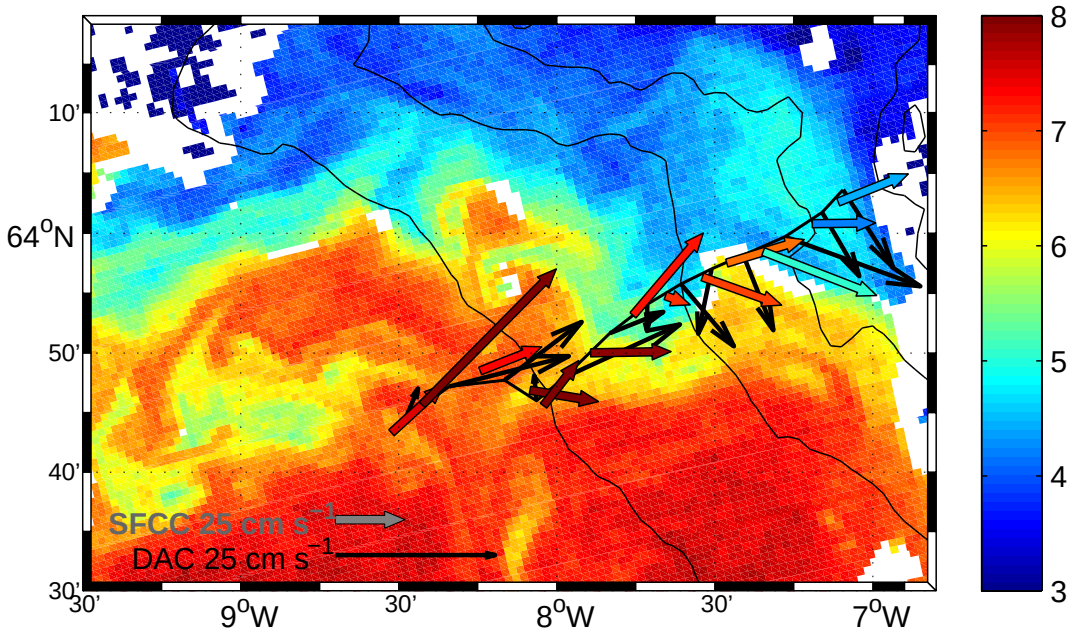

Figure 4.16: MODIS SST from 13 Dec. 2007 and the Depth-average and surface currents from the final 12 dive cycles of the glider section from Figure 4.15 (15-19 Dec. 2007). The Depth-averaged current is shown in black vectors, and the surface current is shown in vectors whose color represents the surface temperature at the location. Note the difference in scales.

Table 4.1: Regional water mass property ranges (Fogelqvist et al., 2003; Hansen and Østerhus, 2000; Read and Pollard, 1992)

Acronym	Name	Temperature range	Salinity range	Notes
NSDW	Norwegian Sea Deep Water	-1.03°C	34.91	
LSFW	Low Salinity Frontal Water	~ 4.5°C	~ 34.7	High O_2
MEIW	Modified East Icelandic Water	$1 \rightarrow 3$°C	$34.6 \rightarrow 34.9$	
NI/AI	N. Icelandic Winter/ Arctic Intermediate water	≥ 3°C	≤ 34.78	
EICW	East Icelandic Current Water	8°C	34.3	
MNAW	Modified North Atlantic Water	$7 \rightarrow 8.5$°C	$35.1 \rightarrow 35.3$	SPMW
NAW	North Atlantic Water	$9.5 \rightarrow 10.5$°C	$35.35 \rightarrow 35.45$	
IW	Iceland Basin Intermediate Water	$6 \rightarrow 8$°C	$35.1 \rightarrow 35.25$	Low O_2
ISOW	Iceland-Scotland Overflow Water	$2.7 \rightarrow 2.9$°C	34.92	

Chapter 5

CONCLUSIONS

The eastern Greenland-Scotland ridge is a unique and important region for the upper and lower branches of the Atlantic Meridional Overturning Circulation. The regional circulation is strongly controlled by topography. The warm and cold branch are in close proximity and interact with one another through microscale mixing and mesoscale dynamics. The processes above the ridge have global consequences via connections to the global Meridional Overturning Circulation.

This thesis investigates exchange and mixing processes above the ridge through an extensive field campaign with Seaglider autonomous vehicles. Over 17,000 high resolution hydrographic profiles augment the historical data. The wintertime coverage of the glider data is a particularly significant contribution.

Chapter 2 is concerned with the mean structure of the dense overflow water south of the ridge crest. Mean plume circulation is defined and estimates of the dense water transport across the Iceland-Faroe Ridge are made. Because it is relatively small, and historically poorly measured, the overflow across the IFR is often ignored in larger scale discussions of the impact of the Nordic Seas overflows. I would argue that it is a poor assumption to ignore IFR overflow. As Chapter 2 shows, the IFR dense water transport is 50% as large as that in the FBC. This is not inconsequential. Perhaps more importantly the IFR overflow is clearly more variable than the FBC or Denmark Strait overflows in its spatial extent, and probably its temporal distribution as well. This variability may have important downstream consequences which justify the inclusion of the IFR overflow with its larger counterparts the FBC and Denmark Strait. The Seaglider sections in the Western Valley of the IFR (Chapter 2) showed

that at least one IFR overflow branch, likely the largest, can be consistently spatially located. The WV branch of overflow exhibited enormous variability on short time scales, but the glider data are insufficient to resolve longer time scale variability. The WV branch of IFR overflow would be an excellent target for a longer term study, perhaps with a combinations of moorings, more capable of producing time series, and gliders providing spatial context.

Chapter 3 develops a novel method to infer dissipation of turbulent kinetic energy from Seaglider finescale vertical velocity profiles. These measurements are important because turbulent entrainment in the overflow plumes is a critical component of the evolution of the plumes and eventual production of North Atlantic Deep Water. Microstructure mixing measurements are highly specialized and difficult, making them relatively rare. By showing that in the highly turbulent regime of the FBC one could used glider finescale vertical velocity to infer dissipation, I was able to map regions of enhanced mixing to a previously unrealized degree. More recently groups have begun to equip gliders with microstructure shear and temperature probes. These developments will hopefully make the types of studies like Chapter 3 routine, augmenting the sparse record of global mixing observations. There will, however, continue to be a large number of gliders without microstructure probes and the method outlined in Chapter 3 might prove useful in other contexts. However the sine qua non of this approach is the presence of a fully developed turbulent cascade. It is likely that the Large Eddy Method would only work in highly turbulent environments, and should be validated with direct microstruture methods before it is trusted in regions outside the FBC.

Chapter 4 investigates a previously unreported seasonal flux of fresh intermediate water across the IFF and IFR. The glider data are a vast improvement over the historical data, particularly in winter, west of the Faroe Islands. The data show the nearly ubiquitous presence of fresh thermohaline intrusions which subduct from the surface waters of the IFF to the south, approximately along the 1027.55 kg m^{-3} isopycnal.

The thermohaline features appear to be related to the onset of deep winter mixing south of the front, where surface mixed layer depths reach 600 m. The mixing results in the destruction of the seasonal thermocline, a PV barrier to subduction of the surface fresh waters. Although the glider data are not sufficient to explicitly resolve the underlaying dynamics several mechanisms of frontal subduction are consistent with the observations. Back of the envelope calculations suggest that the heat and salt flux associated with the subduction of these thermohaline intrusions is comparable to the local cross frontal fluxes of eddies and of double diffusive interleaving.

BIBLIOGRAPHY

Allen, J. and D. Smeed, 1996: Potential vorticity and vertical velocity at the Iceland-Faroes Front. *Journal of Physical Oceanography*, **26**, 2611–2634.

Allen, J., D. Smeed, and A. Chadwick, 1994: Eddies and mixing at the Iceland-Faroes Front. *Deep-Sea Research*, **41**, 51–79.

Bacon, S. and P. Saunders, 2010: The Deep Western Boundary Current at Cape Farewell: Results from a moored current meter array. *Journal of Physical Oceanography*, **40**, 815–829.

Beaird, N. L., I. Fer, P. B. Rhines, and C. C. Eriksen, 2012: Dissipation of turbulent kinetic energy inferred from Seagliders: An application to the eastern Nordic Seas overflows. *Journal of Physical Oceanography*, **42**, 2268–2282.

Beaird, N. L., P. B. Rhines, and C. C. Eriksen, 2013: Overflow waters at the Iceland-Faroe Ridge observed in multiyear Seaglider surveys. *Journal of Physical Oceanography*, **43**, 2334–2351.

Boccaletti, G., R. Ferrari, and B. Fox-Kemper, 2007: Mixed layer instabilities and restratification. *Journal of Physical Oceanography*, **37**, 2228–2250.

Brambilla, E. and L. Talley, 2008: Subpolar Mode Water in the northeastern Atlantic: 1. Averaged properties and mean circulation. *Journal of Geophysical Research*, **113**, C04 025.

Bretherton, F. P., R. E. Davis, and C. B. Fandry, 1976: A technique for objective analysis and design of oceanographic experiments applied to MODE-73. *Deep-Sea Research*, **23**, 559–582.

Broecker, W., 2003: Does the trigger for abrupt climate change reside in the ocean or atmosphere? *Science*, **300**, 1519–1522.

Cenedese, C., J. A. Whitehead, T. A. Ascarelli, and M. Ohiwa, 2004: A dense current flowing down a sloping bottom in a rotating fluid. *Journal of Physical Oceanography*, **34**, 188–203.

Chafik, L., T. Rossby, and C. Schrum, subm.: On the spatial structure and temporal variability of poleward transport between Scotland and Greenland. *Journal of Geophysical Research*.

Danabasoglu, G., W. G. Large, and B. P. Briegleb, 2010: Climate impacts of parameterized Nordic Sea overflows. *Journal of Geophysical Research*, **115**, C11 005.

Darelius, E., I. Fer, and D. Quadfasel, 2011: Faroe Bank Channel Overflow: Mesoscale Variability. *Journal of Physical Oceanography*, **41**, 2137–2154.

Darelius, E., J. Ullgren, and I. Fer, 2013: Observations of barotropic oscillations and their influence on mixing in the Faroe Bank Channel Overflow region. *Journal of Physical Oceanography*, **43**, 1525–1532.

D'Asaro, E. A. and R. C. Lien, 2000a: Lagrangian measurements of waves and turbulence in stratified flows. *Journal of Physical Oceanography*, **30**, 641–655.

D'Asaro, E. A. and R. C. Lien, 2000b: The wave-turbulence transition for stratified flows. *Journal of Physical Oceanography*, **30**, 1669–1678.

Dewey, R., 1999: Mooring Design & Dynamics- a Matlab package for designing and analyzing oceanographic moorings. *Mar. Models*, **1**, 103–157.

Dickson, R. and J. Brown, 1994: The production of North Atlantic Deep Water: Sources, rates and pathways. *Journal of Geophysical Research*, **99 (C6)**, 12 319–12 341.

Dillon, T. M., 1982: Vertical overturns: a comparison of Thorpe and Ozmidov length scales. *Journal of Geophysical Research*, **87**, 9601–9613.

Duncan, L. M., H. L. Bryden, and S. A. Cunningham, 2003: Friction and mixing in the Faroe Bank Channel outflow. *Oceanologica Acta*, **26**, 473–486.

Enmar, L., K. Borenäs, I. Lake, and P. Lundberg, 2009: Comments on "Is the Faroe Bank Channel Overflow Hydraulically Controlled". *Journal of Physical Oceanography*, **39**, 1534–1538.

Eriksen, C. C., in prep.: Conductivity cell thermal inertia correction revisited. *JOURNAL*, **V**, pp.

Eriksen, C. C., T. J. Osse, R. D. Light, T. Wen, T. W. Lehman, P. L. Sabin, J. W. Ballard, and A. M. Chiodi, 2001: Seaglider: a long-range autonomous underwater vehicle for oceanographic research. *IEEE Journal of Oceanic Engineering*, **26**, 424–436.

Fer, I., G. Voet, K. S. Seim, B. Rudels, and K. Latarius, 2010: Intense mixing of the Faroe Bank Channel overflow. *Geophysical Research Letters*, **37**, doi:10.1029/2009GL041 924.

Fogelqvist, E., J. Blindheim, T. Tanhua, S. Østerhus, E. Buch, and F. Rey, 2003: Greenland-Scotland overflow studied by hydro-chemical multivariate analysis. *Deep-Sea Research I*, **50**, 73–102.

Frajka-Williams, E., C. Eriksen, P. Rhines, and R. Harcourt, 2011: Determining vertical water velocities from Seaglider. *Journal of Atmospheric and Oceanic Technology*, **28**, 1641–1656.

Gargett, A., 1999: Velcro measurement of turbulent kinetic energy dissipation rate ε. *Journal of Atmospheric and Oceanic Technology*, **16**, 1973–1993.

Geyer, F., S. Østerhus, B. Hansen, and D. Quadfasel, 2006: Observations of highly regular oscillations in the overflow plume downstream of the Faroe Bank Channel. *Journal of Geophysical Research*, **111 (C12020)**.

Gill, A. E., 1982: *Atmosphere-Ocean Dynamics*. Academic Press, 662 pp.

Girton, J. B., L. J. Pratt, D. A. Sutherland, and J. F. Price, 2006: Is the Faroe Bank Channel Overflow Hydraulically Controlled? *Journal of Physical Oceanography*, **36**, 2340–2349.

Girton, J. B. and T. Sanford, 2003: Descent and modification of the overflow plume in the Denmark Strait. *Journal of Physical Oceanography*, **33**, 1351–1364.

Hallock, Z., 1985: Variability of frontal structure in the southern Norwegian Sea. *Journal of Physical Oceanography*, **15**, 1245–1253.

Hansen, B. and Meincke, 1979: Eddies and meanders in the Iceland-Faroe Ridge area. *Deep-Sea Research*, **26**, 1067–1082.

Hansen, B. and S. Østerhus, 2000: North Atlantic-Nordic Seas exchanges. *Progress in Oceanography*, **45 (2)**.

Hansen, B. and S. Østerhus, 2007: Faroe Bank Channel overflow 1995-2005. *Progress in Oceanography*, **75**, 817–856.

Hansen, B., S. Østerhus, H. Hátún, R. Kristiansen, and K. Larsen, 2003: The Iceland-Faroe inflow of Atlantic water to the Nordic Seas. *Progress in Oceanography*, **59**, 443–474.

Harvey, J. G. and A. Theodorou, 1986: The circulation of Norwegian Sea overflow water in the eastern North Atlantic. *Oceanologica Acta*, **9**, 393–402.

Hermann, F., 1967: The T-S diagram analysis of the water masses over the Iceland-Faroe Ridge and in the Faroe Bank Channel (Overflow '60). *Rapports et Procès-Verbaux des Réunions du Conseil International pout l'Exploration de la Mer*, **157**, 139–149.

Hoskins, B., I. Draghici, and H. Davies, 1978: A new look at the ω-equation. *Quart. J. R. Met. Soc.*, **104**, 31–38.

Hubbard, R. M., 1980: Hydrodynamics technology for an Advanced Expendable Mobil Target (AEMT). APL-UW Tech. Report 8013, Applied Physics Laboratory, University of Washington.

Isachsen, P., C. Mauritzen, and H. Svendsen, 2005: Dense water formation in the Nordic Seas diagnosed from sea surface buoyancy fluxes. *Deep-Sea Research I*, **54**, 22–41.

Johnson, G. C., 2008: Quantifying Antarctic Bottom Water and North Atlantic Deep Water volumes. *Journal of Geophysical Research*, **113**, C05 027.

Johnson, G. C. and T. B. Sanford, 1992: Secondary circulation in the Faroe Bank Channel outflow. *Journal of Physical Oceanography*, **22**, 927–933.

Jónsson, S., 2007: Volume flux and fresh water transport associated with the East Icelandic Current. *Progress in Oceanography*, **73**, 231–241.

Joyce, T., 1977: On the lateral mixing of water masses. *Journal of Physical Oceanography*, **7**, 626–629.

Käse, R. H., G. Voet, C. B. Rodehacke, D. Quadfasel, and N. Serra, 2013: The overflow in the western channel of the Iceland-Faroe Ridge. *Unpublished Manuscript*.

Kida, S., J. Price, and J. Yang, 2008: The upper-oceanic response to overflows: A mechanism for the Azores Current. *Journal of Physical Oceanography*, **38**, 880–895.

Killworth, P., 2001: On the rate of descent of overflows. *Journal of Geophysical Research*, **106**, 22 267–22 275.

Kolmogoroff, A., 1941: The local structure of turbulence in incompressible viscous fluid for very large Reynolds numbers. *Dokl. Akad. Nauk SSSR*, **30**, 299–303.

Legg, S., et al., 2009: Improving oceanic overflow representation in climate models: The Gravity Current Entrainment Climate Process Team. *Bulletin of the American Meteorological Society*, **90**, 657–670.

Lueck, R. G., D. Huang, D. Newman, and J. Box, 1997: Turbulence measurement with a moored instrument. *Journal of Atmospheric and Oceanic Technology*, **14 (1)**, 143–161.

Mauritzen, C., 1996: Production of dense overflow waters feeding the North Atlantic across the Greenland-Scotland Ridge. Part 1: Evidence for a revised circulation scheme. *Deep-Sea Research*, **43**, 769–806.

Mauritzen, C., J. Price, T. Sanford, and D. Torres, 2005: Circulation and mixing in the Faroese Channels. *Deep-Sea Research*, **52**, 883–913.

McCartney, M. and L. Talley, 1982: The Subpolar Mode Water of the North Atlantic. *Journal of Physical Oceanography*, **12**, 1169–1188.

Meincke, J., 1972: The hydrographic section along the Iceland-Faroe Ridge carried out by R.V. '*Anton Dohrn*' in 1959-1971. *Berichte der Deutchen Wissenchaftlichen Kommission für Meeresforschung*, **22**, 372–384.

Meincke, J., 1978: On the distribution of low salinity intermediate waters around the Faroes. *Deutsche Hydrographische Zeitschrift*, **31**, 50–64.

Merckelbach, L., D. Smeed, and G. Griffiths, 2010: Vertical water velocities from underwater gliders. *Journal of Atmospheric and Oceanic Technology*, **27**, 547–563.

Moum, J. N., 1996: Energy-containing scales of turbulence in the ocean thermocline. *Journal of Geophysical Research*, **101 (C6)**.

Niiler, P., 1992: Sea surface temperature variability of the Iceland-Faeroe Front. *Journal of Geophysical Research*, **97 (C11)**, 17 777–17 785.

Nof, D., N. Paldor, and S. V. Gorder, 2002: The Reddy maker. *Deep-Sea Res.*, **49**, 1531–1549.

Orvik, K. and P. Niiler, 2002: Major pathways of the Atlantic water in the northern North Atlantic and Nordic Seas toward Arctic. *Geophysical Research Letters*, **29 (19)**, doi:10.1029/2002GL015002.

Østerhus, S., W. Turrell, S. Jónsson, and B. Hansen, 2005: Measured volume, heat, and salt fluxes from the Atlantic to the Arctic Mediterranean. *Geophysical Research Letters*, **32 (L07603)**.

Perkins, H., T. S. Hopkins, S. A. Malmberg, P. M. Poulain, and A. Warn-Varnas, 1998: Oceanographic conditions east of Iceland. *Journal of Geophysical Research*, **103**, 21 531–21 542.

Perkins, H., T. J. Sherwin, and T. Hopkins, 1994: Amplification of tidal currents by overflow on the Iceland-Faroe ridge. *Journal of Physical Oceanography*, **24**, 721–735.

Peters, H., M. C. Gregg, and T. B. Sanford, 1995: Detail and scaling of turbulent overturns in the Pacific Equatorial Undercurrent. *Journal of Geophysical Research*, **100 (C9)**.

Pistek, P. and D. Johnson, 1992: A study of the Iceland-Faeroe Front using GEOSAT altimetry and current-following drifters. *Deep-Sea Research*, **39**, 2029–20511 549.

Pollard, R. and L. Regier, 1992: Vorticity and vertical circulation at an ocean front. *Journal of Physical Oceanography*, **22**, 609–625.

Prater, M. D. and T. Rossby, 2005: Observations of the Faroe Bank Channel outflow using bottom-following RAFOS floats. *Deep-Sea Research*, **52**, 481–494.

Pratt, L. J. and P. Lundberg, 1991: Hydraulics of rotating strait and sill flow. *Annual Review of Fluid Mechanics*, **23**, 81–106.

Pratt, L. J., U. Riemenschneider, and K. R. Helfrich, 2007: A transverse hydraulic jump in a model of the Faroe Bank Channel outflow. *Ocean Modelling*, **19**, 1–9.

Price, J. F. and M. O. Baringer, 1994: Overflows and deep water production by marginal seas. *Progress in Oceanography*, **33**, 161–200.

Read, J. and R. Pollard, 1992: Water Masses in the Region of the Iceland-Faeroes Front. *Journal of Physical Oceanography*, **22**, 1365–1378.

Riemenschneider, U. and S. Legg, 2007: Regional simulations of the Faroe Bank Channel overflow in a level model. *Ocean Modelling*, **17**, 93–122.

Rossby, T. and C. Flagg, 2012: Direct measurement of the volume flux in the Faroe-Shetland Channel and over the Iceland-Faroe Ridge. *Geophysical Research Letters*, **39 (L07602)**.

Rossby, T., M. Prater, and H. Søiland, 2009: Pathways of inflow and dispersion of warm waters in the Nordic seas. *Journal of Geophysical Research*, **114 (C04011)**.

Sarafanov, A., A. Falina, H. Mercier, A. Sokov, and A. Demidov, 2008: Intense warming and salinification of the intermediate waters of southern origin in the eastern subpolar North Atlantic in the 1990s to mid-2000s. *Journal of Geophysical Research*, **113**, C12 022.

Sarafanov, A., et al., 2012: Mean full-depth summer circulation and transports at the northern periphery of the Atlantic Ocean in the 2000s. *Journal of Geophysical Research*, **117**, C01 014.

Saunders, P. M., 1990: Cold outflow from the Faroe Bank Channel. *Journal of Physical Oceanography*, **20**, 29–43.

Saunders, P. M., 1994: The flux of overflow water through the Charlie-Gibbs fracture zone. *Journal of Geophysical Research*, **99 (C6)**, 12 343–12 355.

Saunders, P. M., 1996: The flux of dense cold overflow water southeast of Iceland. *Journal of Physical Oceanography*, **26**, 85–95.

Scott, J. and A. McDowall, 1990: Cross-frontal cold jets near Iceland: In-water, satellite infrared, and Geosat altimeter data. *Journal of Geophysical Research*, **95 (C10)**, 18 005–18 014.

Seim, K. S. and I. Fer, 2011: Mixing in the stratified interface of the Faroe Bank Channel overflow: the role of transverse circulation and internal waves. *Journal of Geophysical Research*, **116**, C07 022.

Seim, K. S., I. Fer, and J. Berntsen, 2010: Regional simulations of the Faroe Bank Channel overflow using a σ-coordinate ocean model. *Ocean Modelling*, **35**, 31–44.

Skagseth, Ø., T. Furevik, R. Ingvaldsen, H. Loeng, K. Mork, K. Orvik, and V. Ozhigin, 2008: Volume and heat transports to the Arctic Ocean vie the Norwegian and Barents Seas. *Arctic-Subarctic Ocean Fluxes*, R. Dickson, J. Meincke, and P. Rhines, Eds., Springer, Dordrecht, The Netherlands.

Smart, J., 1984: Spatial variability of major frontal systems in the North Atlantic-Norwegian Sea area: 1980-1981. *Journal of Physical Oceanography*, **14**, 185–192.

Smyth, W. and S. A. Thorpe, 2012: Glider measurements of overturning in a Kelvin-Helmholtz billow train. *Journal of Marine Research*, **70**, 119–140.

Spall, M., 1995: Frontogenesis, subduction, and cross-front exchange at upper ocean fronts. *Journal of Geophysical Research*, **100 (C2)**, 2543–2557.

Spall, M., 2010: Dynamics of downwelling in an eddy resolving convective basin. *Journal of Physical Oceanography*, **40**, 2341–2347.

Steele, J. H., 1959: Observations of deep water overflow across the Iceland-Faroe Ridge. *Deep-Sea Research*, **6**, 70–72.

Swift, J., 1984: The circulation of the Denmark Strait and Iceland-Scotland overflow waters in the North Atlantic. *Deep-Sea Research*, **31 (11)**, 1339–1355.

Talley, L., 2003: Shallow, intermediate, and deep overturning components of the global heat budget. *Journal of Physical Oceanography*, **33**, 530–560.

Taylor, G. I., 1935: Statistical theory of turbulence. *Proc. R. Soc. London A*, **151**, 421–454.

Tennekes, H. and J. L. Lumley, 1972: *A First Course in Turbulence*. The MIT Press, 300 pp.

Thomas, L. and T. Joyce, 2010: Subduction on the northern and southern flanks of the Gulf Stream. *Journal of Physical Oceanography*, **40**, 429–438.

Thomas, L. and C. Lee, 2005: Intensification of ocean fronts by down-front winds. *Journal of Physical Oceanography*, **35**, 1086–1102.

Thorpe, S. A., 2005: *The Turbulent Ocean*. Cambridge University Press, 439 pp.

Ullgren, J., I. Fer, E. Darelius, and N. Beaird, in press: Interaction of the Faroe Bank Channel overflow with Iceland Basin intermediate waters. *Journal of Geophysical Research*.

Umlauf, L., L. Arneborg, H. Burchard, V. Fiekas, H. Lass, and V. Mohrholz, 2007: Transverse structure of turbulence in a rotating gravity current. *Geophysical Research Letters*, **34 (L08601)**.

van Aken, H. and G. Becker, 1996: Hydrography and through-flow in the north-eastern North Atlantic Ocean: the NANSEN project. *Progress in Oceanography*, **38**, 297–346.

van Aken, H. and C. de Boer, 1995: On the synoptic hydrography of intermediate and deep water masses in the Iceland Basin. *Deep Sea Research*, **42**, 165–189.

Wilkenskjeld, S. and D. Quadfasel, 2005: Response of the Greenland-Scotland overflow to changing deep water supply from the Arctic Mediterranean. *Geophysical Research Letters*, **32 (L21607)**.

Willebrand, J. and J. Meincke, 1980: Statistical analysis of fluctuations in the Iceland-Scotland frontal zone. *Deep Sea Research*, **27A**, 1047–1066.

Wåhlin, A. K. and G. Walin, 2001: Downward migration of dense bottom currents. *Environmental Fluid Mechanics*, **1**, 257–279.

Xu, X., W. Schmitz, H. Hurlburt, P. Hogan, and E. Chassignet, 2010: Transport of Nordic Seas overflow water into and within the Irminger Sea: An eddy-resolving simulation and observations. *Geophysical Research Letters*, **115 (C12048)**.

VITA

Nicholas Beaird was born in Hanover New Hampshire in 1983. He earned a bachelor's degree in Physics and Mathematical Sciences at Colby College in Waterville Maine in 2006. At the University of Washington he earned a Masters of Science in Oceanography in 2010 and a Doctor of Philosophy in 2013.